UNLV Theses, Dissertations, Professional Papers, and Capstones

5-2008

Imaging the southern trace of the Black Hills fault, Clark County, Nevada

Shelley A. Zaragoza
University of Nevada, Las Vegas

Follow this and additional works at: https://digitalscholarship.unlv.edu/thesesdissertations

Part of the Geology Commons, Geophysics and Seismology Commons, and the Tectonics and Structure Commons

IMAGING THE SOUTHERN TRACE OF THE BLACK HILLS FAULT,

CLARK COUNTY, NEVADA

By

Shelley A. Zaragoza

Bachelor of Science
University of Nevada, Las Vegas
2004

A thesis submitted in partial fulfillment
Of the requirements for the

Master of Science Degree in Geoscience
Department of Geoscience
College of Sciences

Graduate College
University of Nevada, Las Vegas
May 2008

UNLV
UNIVERSITY OF NEVADA LAS VEGAS

Thesis Approval

The Graduate College
University of Nevada, Las Vegas

November 30, 20 07

The Thesis prepared by

Shelley A. Zaragoza

Entitled

Imaging the Southern Trace of the Black Hills Fault, Clark County, Nevada

is approved in partial fulfillment of the requirements for the degree of

Master of Science Degree in Geoscience

Examination Committee Chair

Dean of the Graduate College

Examination Committee Member

Examination Committee Member

Graduate College Faculty Representative

1017-83

ii

ABSTRACT

Imaging the Southern Trace of the Black Hills Fault, Clark County, Nevada

by

Shelley A. Zaragoza

Dr. Catherine M. Snelson, Examination Committee Chair
Assistant Professor of Geophysics
University of Nevada, Las Vegas

The Black Hills fault (BHF) is a SE-dipping normal fault forming the northwestern structural boundary of the Eldorado basin, ~20 km southeast of Las Vegas, Nevada (Langenheim and Schmidt, 1996). The fault offsets Holocene strata and is thus considered to be active (Fossett, 2005). Therefore, the BHF poses a significant seismic hazard to the greater Las Vegas area.

Fossett (2005) estimated that the BHF is capable of producing a M_w 6.4 to 6.8 earthquake. However, this suggests a subsurface rupture length greater than the scarp length (Fossett, 2005). To test this hypothesis, remote sensing, geologic mapping, and high-resolution seismic reflection survey were utilized. The result is an interpretive geologic cross-section showing several SE-dipping normal faults on strike with the BHF. This implies that the BHF may be >6 km in length. In addition, several models are proposed to explain the anomalous orientation of the BHF relative to other normal faults in the area.

TABLE OF CONTENTS

LIST OF FIGURES

ACKNOWLEDGEMENTS

provided the opportunity for me to gain some field experience in high-resolution seismic reflection acquisition, and made this a whole lot of fun. Moreover, I would like to thank Sandra Saldaña for technical support (hardware and software), many venting opportunities, Lifehouse, an abundance of chocolate, and much, much more.

Last, but not least, I would like to thank my friends and family. Mom, your cards and letters, your enthusiasm for my research, and your patient understanding mean much more than can be expressed in words. Al, thank you for not letting me give up, and for burning the midnight oil with me. I have learned so much from you. Lala, I am truly moved by your exceptional courage and tenacity. You will always be my best friend. Diana and Lynette, my dear sisters, you are both excellent cheerleaders. Thank you Chris and Alice for the

spiritual insight, and because your home is always open to me. Margaret, I cannot thank you enough for the many life-lessons. Without you, I would not be the person I am today. Thank you, Kirk and Judy, for treating me like family. I always feel at home when I am with you. Thank you, Moosechippers, for your indefinitely lasting friendship and many, many laughs. Thank you, J.P., Toni, and the Flints for helping me to see the future and focus on it. Thank you, Bob and Helen Shook; you have had many daughters besides your own. I consider it an honor to be one of them. Thank you all for your confidence that I could find power beyond what is normal.

CHAPTER ONE

INTRODUCTION

The Black Hills fault (BHF) (Figure 1), Clark County, Nevada is located within

the central Basin and Range Province (e.g., Burchfiel et al., 1992; Wernicke,

1992), ~20 km SE of Las Vegas (Langenheim and Schmidt, 1996). Extensional

tectonic processes have shaped the region, particularly during the Cenozoic,

giving southern Nevada its characteristic normal and strike-slip faults (e.g.,

Burchfiel et al., 1992; Wernicke, 1992; Faulds et al., 2001). Recent paleoseismic

studies have documented Quaternary activity on several southern Nevada faults

(Slemmons et al., 2001; dePolo et al., 2006).

Previously, faulting in the Las Vegas Valley was thought to be primarily due to

compaction as the result of groundwater withdrawal from local wells (e.g.,

Slemmons et al., 2001). More recent studies have concluded that these faults

are tectonic in origin, and many of these faults could produce earthquakes in the

M_w5.0 to 7.0 range (Figure 1) (e.g., Slemmons et al., 2001; Taylor et al., 2003;

dePolo et al., 2006). However, the location, geometries, and seismic potential of

faults in the greater Las Vegas area are poorly constrained. Several factors

contribute to the difficulties in analyzing these faults. Many faults have not been

adequately mapped or are obscured by urban cover, producing a database that

is insufficient for determining slip rate and recurrence intervals (e.g., Slemmons et al., 2001).

Historically, much of the instrumentation used to record local earthquakes has been deployed only temporarily (e.g., Smith et al., 2001). Instrumentation may record only large events, whereas microseisms may occur with greater frequency and therefore be valuable in locating active faults (USGS, 2007). In addition, instrumentation is sparse and tends to cluster in the Las Vegas area, which biases locations of earthquakes outside Las Vegas, such as those occurring in the Eldorado Valley (Figure 1) (e.g., Smith et al., 2001). As a result, the seismic hazard from area faults is insufficiently defined.

Seismic hazard characterization of the BHF is an important step in defining the poorly constrained faults of southern Nevada (e.g., Slemmons et al., 2001). The BHF is one of several active tectonic faults in the vicinity of Las Vegas with a potential of generating M_w >5.0 earthquakes (Figure 1) (e.g., Slemmons et al., 2001). The BHF may have been the source of two earthquakes felt by area residents in 1988, although the location of these events is uncertain, due to insufficient instrumentation (Smith et al., 2001).

The BHF forms the northwestern structural boundary of the Eldorado Valley, and is located between the growing communities of Henderson and Boulder City (Figure 1) (Langenheim and Schmidt, 1996). Therefore, the BHF may specifically pose a hazard to Boulder City, Henderson, and the Las Vegas metropolitan area, as well as nearby pipelines, power lines, power stations, and industrial complexes (Fossett, 2005).

2

Previous workers have concluded that the BHF does pose a significant seismic hazard to southern Nevada (e.g., Smith et al., 2001; Fossett, 2005), but specific hazard estimates based on various criteria have produced significantly different results. For example, earthquake magnitude estimates based on surface rupture length (SRL) versus displacement values differ significantly for the BHF. Estimates based on the 4.5 km scarp indicate an earthquake potential of M_w 5.7 (Fossett, 2005). However, estimates based on displacement values documented in a paleoseismic trench indicate a higher value of M_w 6.4 to 6.8 (Fossett, 2005). This may imply that the subsurface rupture length is significantly greater than the length of the scarp (Fossett, 2005). This conclusion would agree with Anderson (1977), who mapped the trace of the BHF along the entire mountain front south of the scarp, for a total length of 9.5 km.

To test the hypothesis that the BHF trace continues southward, this study utilized a three-component approach. Remote sensing was used as a reconnaissance tool to determine the ideal study location. Geologic mapping of the area south of the BHF scarp was performed to document surface geology, including structures and geomorphology that may be related to the BHF. In addition, a high-resolution seismic reflection survey was conducted to examine the proposed southern trace of the BHF (Anderson, 1977; Fossett, 2005) to determine whether the fault ends abruptly at the southern tip of the fault scarp, or whether the fault is buried underneath basin sediments to the south. This should be particularly valuable in explaining the discrepancy between seismic hazard

3

estimates based on SRL and those based on displacement values (Fossett, 2005).
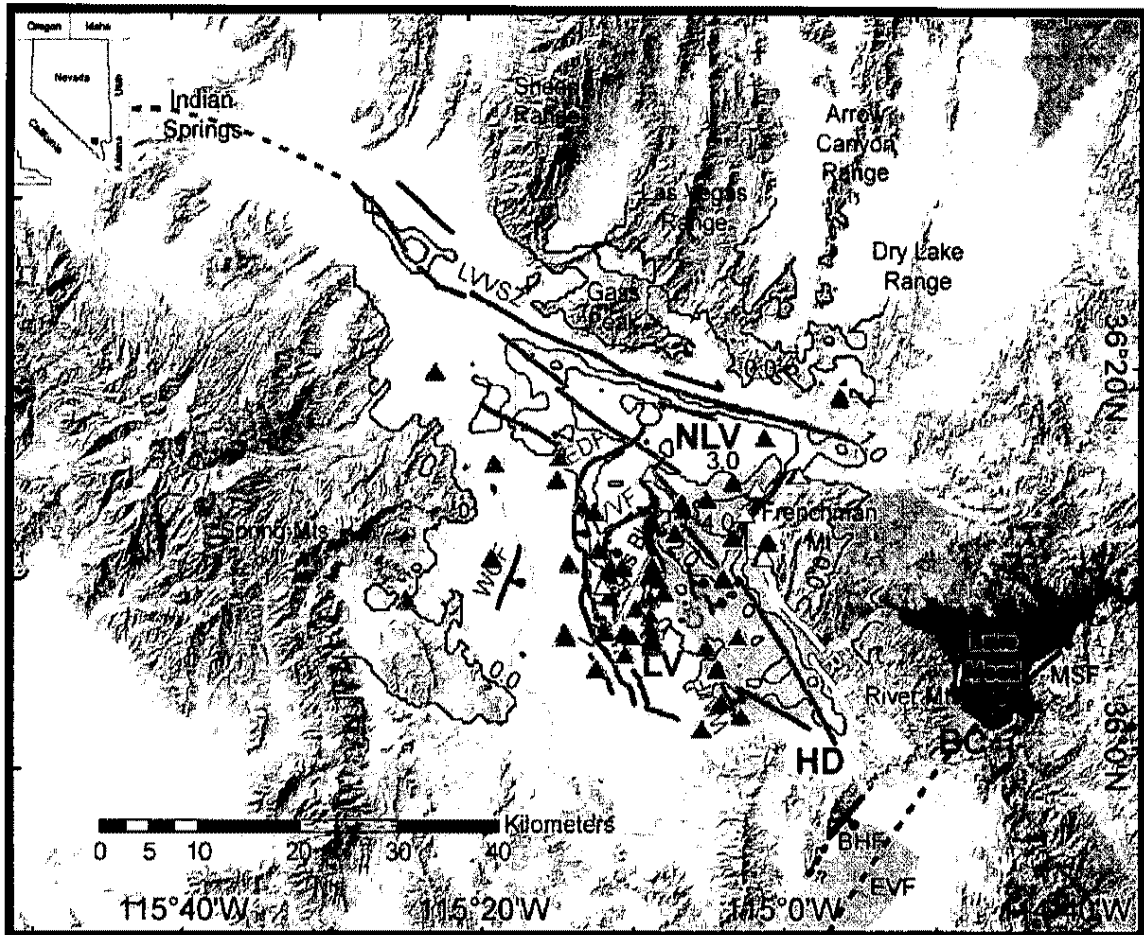
Figure 1. Simplified colored relief map of the Las Vegas area showing Quaternary age faults (adapted from Bell, 1981; Langenheim and Schmidt, 1996; Langenheim et al., 2001; Slemmons et al., 2001; Fossett, 2005). The Black Hills fault (BHF) is shown in red. Nearby communities include BC-Boulder City, HD-Henderson, LV-Las Vegas, and NLV-North Las Vegas. The Eldorado Valley (EVF) and Mead Slope (MSF) faults are shown in purple. The Miocene Las Vegas Valley Shear Zone (LVVSZ) is shown in green. The west-dipping Frenchman Mountain (FF) and River Mountains (RMF) faults are shown in yellow. East-dipping faults of the Las Vegas Valley fault system are shown in brown: CF-Cashman fault, EDF-Eglington Decatur fault, VVF-Valley View Fault, WCF-West Charleston fault, and WMF-Whitney Mesa fault. The Las Vegas Strip is shown in orange for reference. Black contours show Las Vegas basin depth in meters (Langenheim et al., 2001). Triangles show earthquake recording stations: Orange-Blume & Associates array, Red-ANSS stations, Blue-LLNL broadband stations deployed Sept 2002-Jan 2003, Yellow- LLNL broadband stations deployed Nov 2002-Jan 2003. Regional inset map shows the state of Nevada with the Las Vegas area marked as a black square.

5

CHAPTER TWO

GEOLOGIC BACKGROUND

The highly extended Basin and Range Province (Figure 2) underwent

episodic tectonism throughout its geologic history (e.g., Burchfiel et al., 1992).

The basement complex in this region consists of Proterozoic crystalline rocks of

the North American craton (e.g., Burchfiel et al., 1992). During the late Middle

Proterozoic, a series of three episodes of extension and deposition occurred from

1500 to 800 Ma (e.g., Burchfiel et al., 1992). A fourth extensional event in the

latest Proterozoic was followed by the inception of the Cordilleran passive margin

(e.g., Burchfiel et al., 1992). A westward-thickening wedge of sedimentary rocks

was then deposited during latest Proterozoic and Paleozoic times (e.g., Burchfiel

et al., 1992).

The passive margin ended in the latest Devonian with the onset of a series of

orogenic episodes, separated by periods of sedimentary deposition (e.g.,

Burchfiel et al., 1992). The first of these orogenies occurred in the latest

Devonian-Early Mississippian, thrusting the Antler allochthon ~200 km eastward

over the continental shelf along the Roberts Mountains thrust (e.g., Burchfiel et

al., 1992). During the Late Paleozoic-Early Mesozoic, the Sonoma orogeny

thrust the Golconda allochthon eastward onto the western continental margin

(e.g., Burchfiel et al., 1992). The Late Jurassic Nevadan orogeny resulted from

the collision of an island arc with the continental margin (e.g., Burchfiel et al., 1992). Compression of the crust during the Mesozoic Sevier orogeny produced east-vergent fold and thrust belts, including faults such as the Keystone and Gass Peak thrusts (Figure 3) (e.g., Burchfiel et al., 1992; Taylor, 1998; DeCelles, 2004).

With the initiation of the San Andreas fault, a transform plate boundary formed during the Cenozoic, which contributed greatly to Cenozoic extension in the Basin and Range Province (Figure 2) (e.g., Atwater, 1970; Wernicke, 1992; Taylor, 1998). The Basin and Range Province is generally separated into northern, central, and southern regions, based on each region's extensional history and structural style (Figure 2) (e.g., Wernicke, 1992). During the Oligocene and Miocene, extension was accompanied by extensive volcanism, which swept southward through the northern Basin and Range and northward through the southern Basin and Range (Figure 4) (e.g., Wernicke, 1992; Humphreys, 1995). These sweeps of Oligocene and Miocene volcanism ceased in the central Basin and Range at about the latitude of Lake Mead at ~12 Ma (Faulds et al., 2001). Early to middle Miocene plutonic rocks with geochemically related volcanic rocks are common in the River Mountains, Eldorado Mountains, and McCullough range (e.g., Weber and Smith, 1987; Faulds et al., 2001).

This igneous activity was followed by a period of erosion and deposition (e.g., Faulds et al., 2001). Clastic units in local basin fill probably include the late Oligocene to Miocene Horse Spring Formation, the late Miocene Red Sandstone unit, and the Miocene to Pliocene Muddy Creek formation (e.g., Anderson, 1977;

7

Tabor, 1982; Bohannon, 1984). Erosion and deposition continued into the Quaternary, resulting in sedimentary units, such as fanglomerates, channel fill, and playa deposits, that are visible at the surface or are buried beneath younger fan deposits or basin fill (e.g., Anderson and O'Connell, 1993; Fossett, 2005).

Strike-slip and normal faulting are characteristic of central Basin and Range extension (e.g., Burchfiel et al., 1992; Taylor, 1998). Typical of such structures are the dextral Las Vegas Valley Shear Zone (LVVSZ) (Figure 1) and sinistral Lake Mead Fault System (LMFS), which became active during the Cenozoic (e.g., Duebendorfer and Black, 1992; Campagna and Aydin, 1994; Taylor, 1998; Slemmons et al., 2001). The LMFS includes the Mead Slope fault (MSF) (Figure 1) and the Hamblin Bay fault (HBF) (Anderson, 1973; Bohannon, 1979) and has been hypothesized to extend southward to link up with the sinistral Eldorado Valley fault (EVF) (Weber and Smith, 1987; Langenheim and Schmidt, 1996) and/or the BHF (Slemmons et al., 2001; Fossett et al., 2003a).

The study area contains lithologic units ranging from Quaternary to Proterozoic ages (Figures 5 and 6). South of Lake Mead, the McCullough Range and Eldorado Mountains consist of Miocene volcanic units, which lie atop Proterozoic metamorphic and Late Cretaceous plutonic rocks (e.g., Anderson, 1977; Faulds et al., 2001). Prior to deposition of these volcanic units, the Paleozoic and Mesozoic units in the McCullough Range were removed, causing an unconformity between the volcanic rocks and the Proterozoic basement (e.g., Anderson, 1977; Faulds et al., 2001). The Black Hills consist primarily of a Miocene quartz monzonite pluton, with 14 strands of the BHF indicated by

scarps, up to 4.5 km in length, on its southeast flank (Anderson, 1977; Fossett, 2005). Andesite and altered andesite of the McCullough Range are exposed in the southern portion of the Black Hills, and altered dacite of the River Mountains is exposed at the northern extremity of the Black Hills (Anderson, 1977; Fossett, 2005). Anderson (1977) documented local Pliocene clastic deposits as belonging to the Muddy Creek formation, although Fossett (2005) mapped these same units as Tertiary-Quaternary sedimentary rocks of an unspecified formation. This discrepancy is probably generated by the fact that the Muddy Creek formation is not well resolved. Quaternary units include fanglomerates, playa deposits, basin fill, and channel deposits, all of local derivation (Anderson, 1977; Langenheim and Schmidt, 1996; Fossett, 2005). Geologic units intersecting the seismic section include Miocene altered andesite and Quaternary fanglomerate (Figure 6).
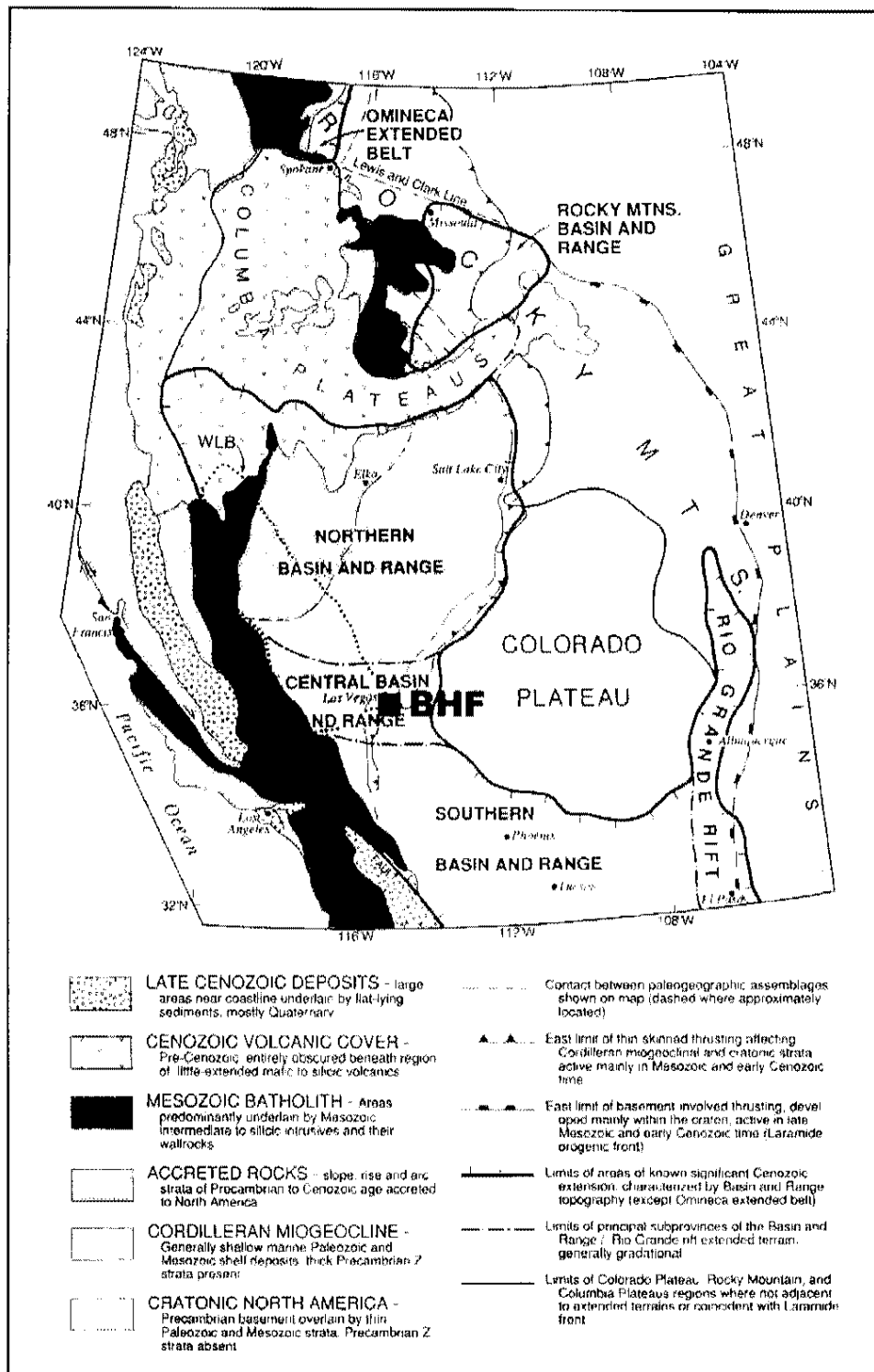
Figure 2. Map of the Basin and Range Province, with key, from Wernicke (1992). Cities are marked with a black dot. WLB indicates the Walker Lane Belt. The study area is located in the central Basin and Range and is marked by the blue box (BHF).

10
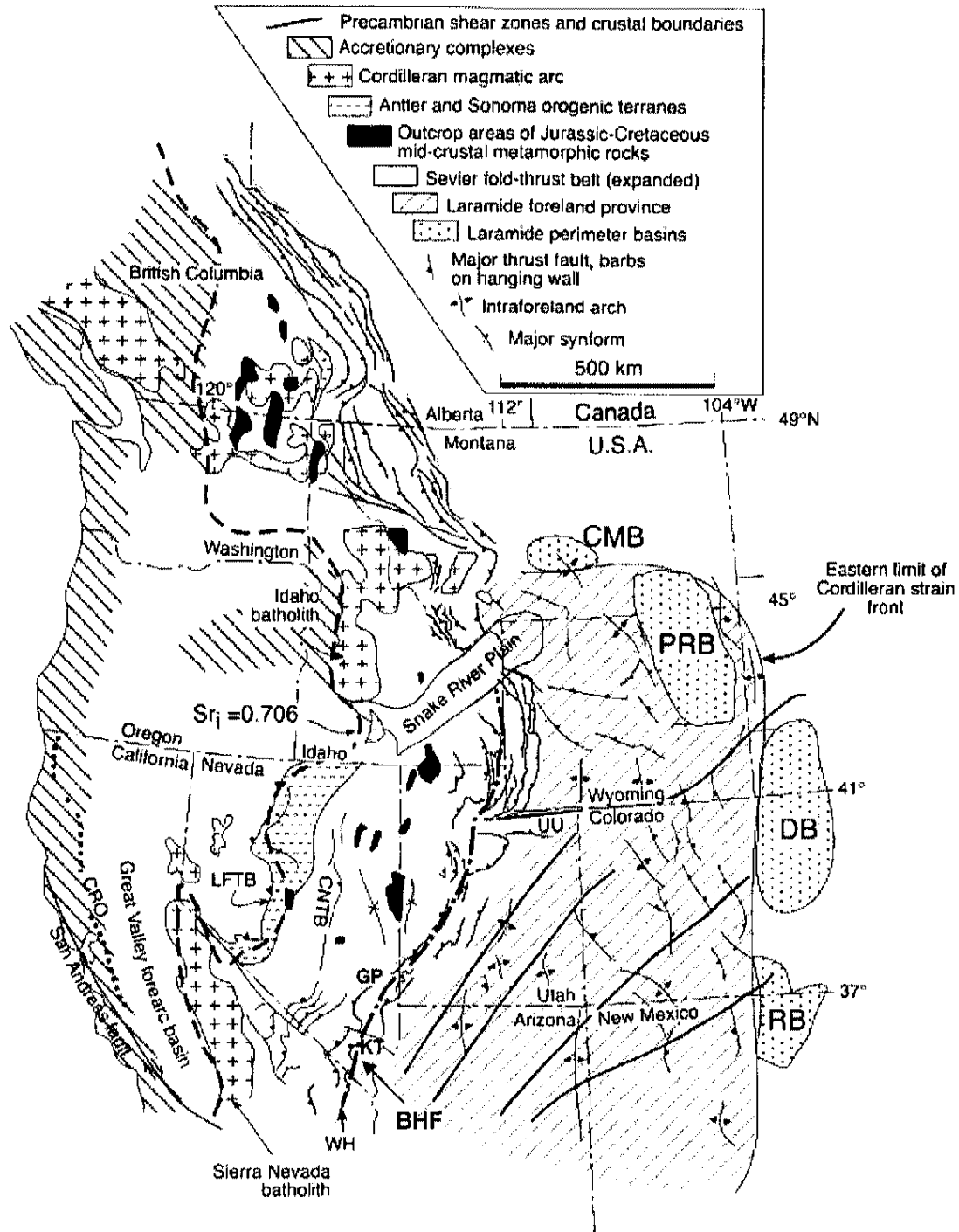
Figure 3. Map of the western United States from DeCelles (2004) showing the location of the Sevier fold and thrust belt in gray. BHF-Black Hills fault, GP-Gass Peak thrust fault, KT-Keystone thrust fault, CRO-Coast Range ophiolite, LFTB-Luning-Fencemaker thrust belt, CNTB-Central Nevada thrust belt, WH-Wasatch hinge line, UU-Uinta Mountains uplift, CMB-Crazy Mountains basin, PRB-Powder River basin, DB-Denver basin, RB-Raton basin, Sr_i=0.706 (dashed line) indicates the edge of the north American cratonic basement (e.g., DeCelles, 2004).

11
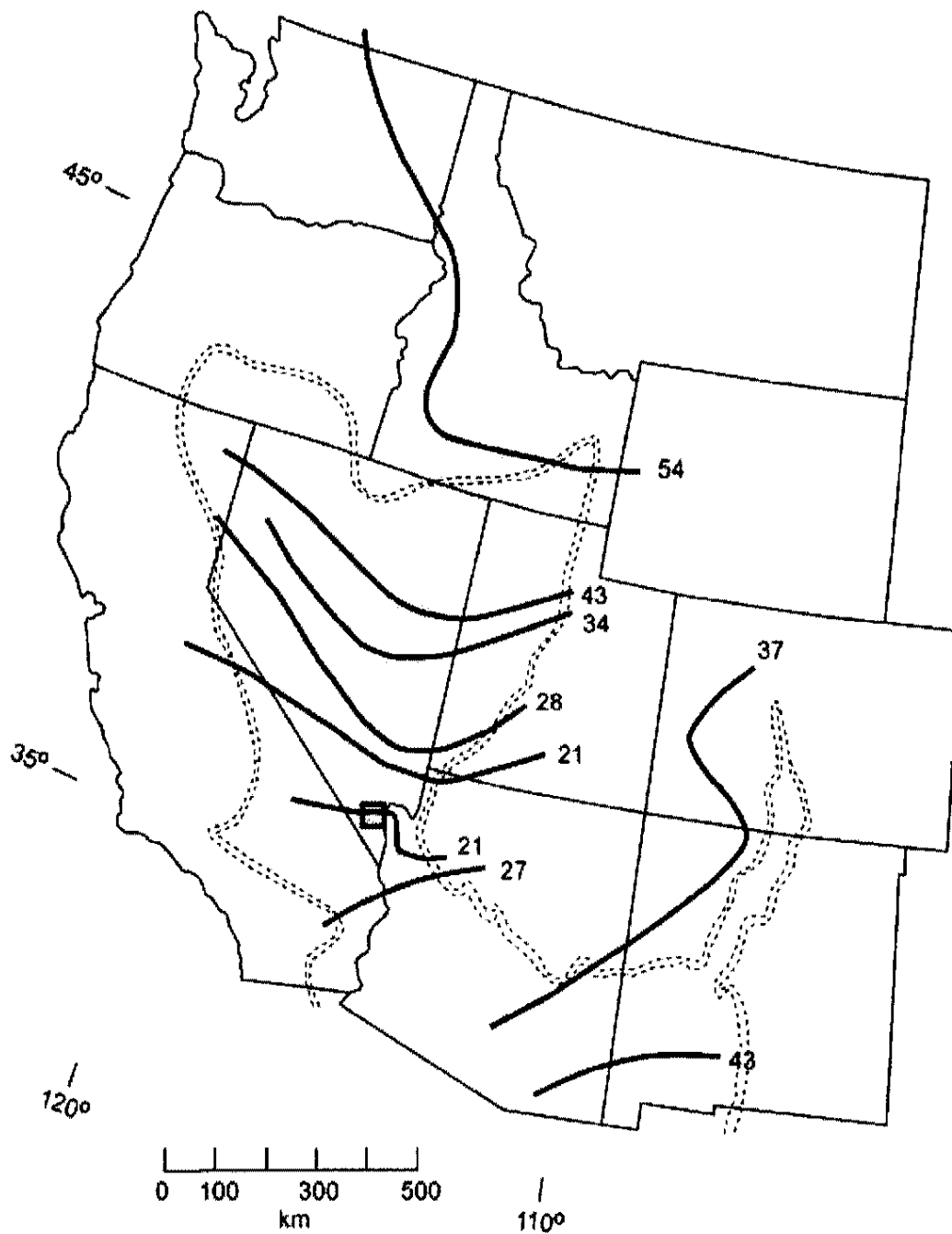
Figure 4. Directions and timing of Basin and Range magmatic propagation ~54 to 21 Ma, from Humphreys (1995). Solid black lines show boundaries of magmatic fronts at the given times (Ma), from Christiansen et al. (1992). Double dashed lines show outline of the Basin and Range province and the Rio Grande Rift. Gray arrows show the direction of propagation for each magmatic front. Study area is located in the red box.
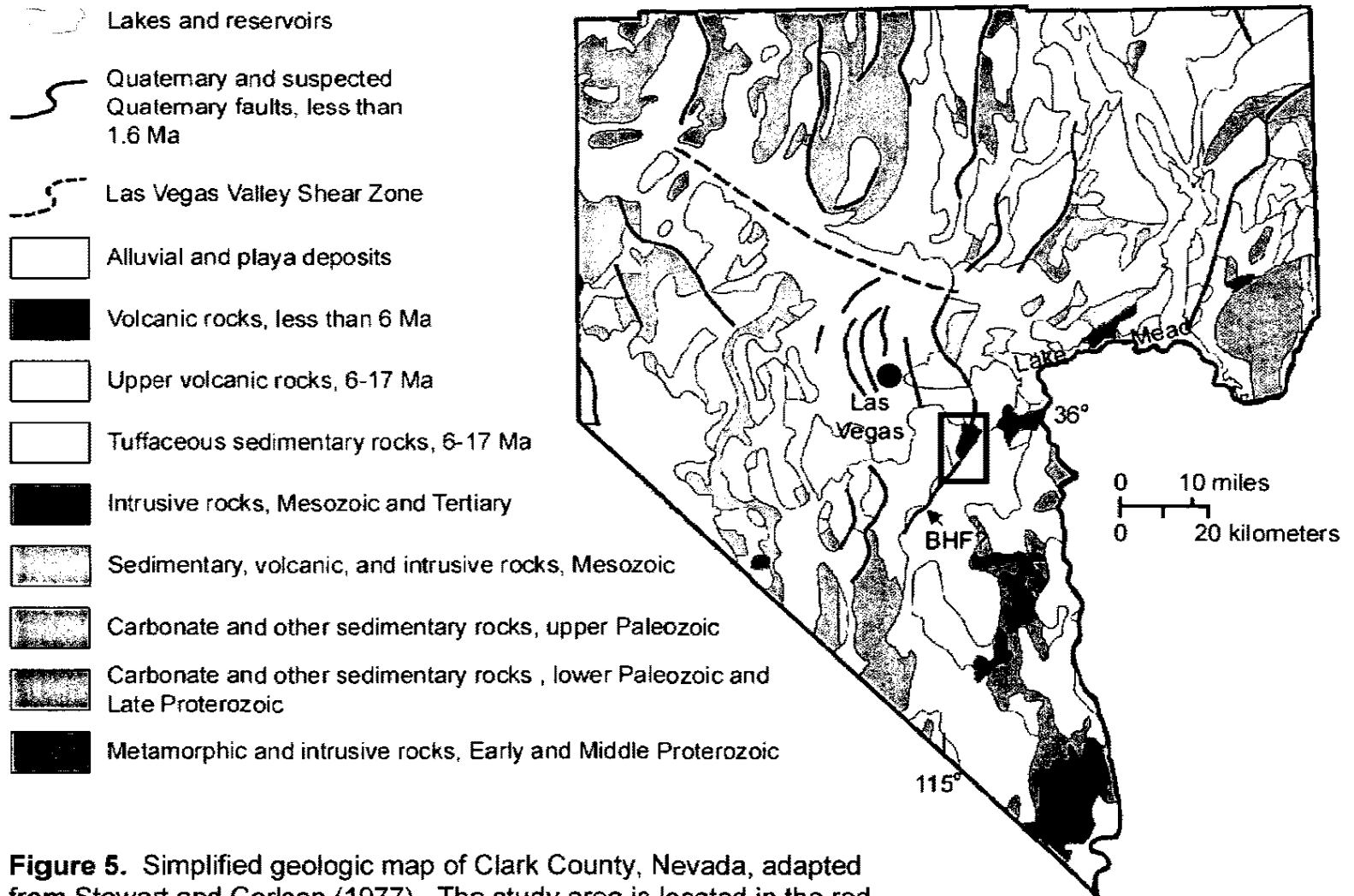
Figure 5. Simplified geologic map of Clark County, Nevada, adapted from Stewart and Carlson (1977). The study area is located in the red box. The red dot shows the location of Las Vegas. The black arrow indicates the proposed southern trace of the BHF.

13

Ma	EON	ERA	PERIOD	EPOCH	UNIT(S)
			QUATER-NARY	HOLOCENE	FANGLOMERATES
				PLEISTOCENE	
5				PLIOCENE	
					MUDDY CREEK FM?
10	CENOZOIC		NEOGENE	MIOCENE	RED SANDSTONE UNIT
					HORSE SPRING FM.
					BLACK HILLS PLUTON
15					ALTERED ANDESITES
70	MESOZOIC		CRETACEOUS	LATE	PLUTONIC ROCKS
75					
550		LATE			
800					
1050	PROTEROZOIC	MIDDLE			
1300					
1550					
1800		EARLY			METAMORPHIC BASEMENT

Unconformity
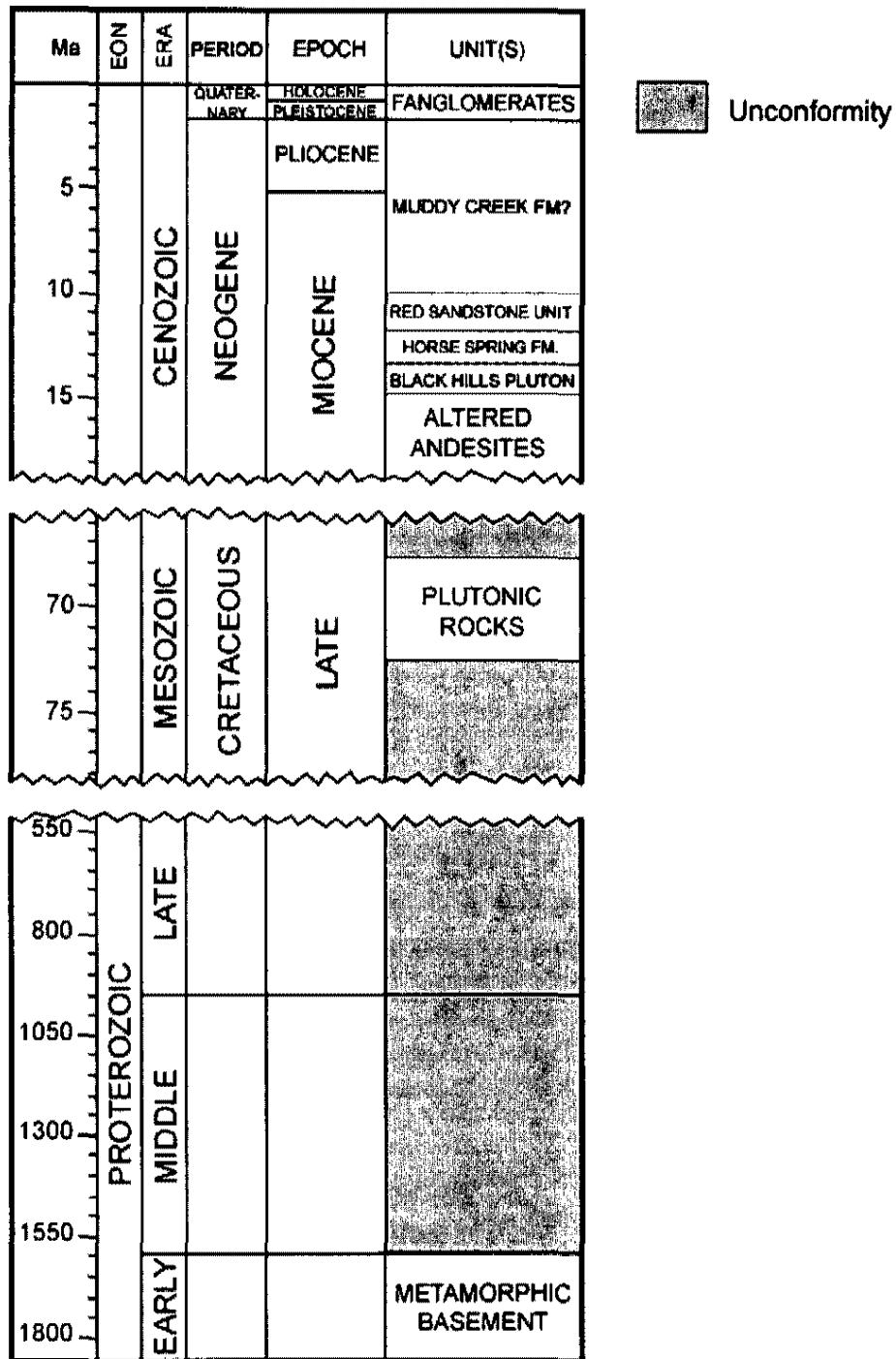
Figure 6. Stratigraphic column of the study area. Geologic units that intersect the seismic section include Quaternary fanglomerates and Miocene altered andesites. Geologic time scale nomenclature and Ma from Palmer and Geissman (1999), and approximate ages of rock units from Bohannon (1984), Faulds et al. (2001) and Fossett (2005).

CHAPTER THREE

PREVIOUS STUDIES

Geologic mapping has been one of the principle means used to document the

BHF, which in early studies was called the EVF (Werle and Knight, 1992;

Anderson and O'Connell, 1993). Anderson (1977) mapped the vicinity of the

BHF at a scale of 1:62,500 and projected the fault to continue ~5 km south of the

scarp, along the linear mountain front. Anderson and O'Connell (1993) did not

observe bevels in the scarp and concluded that the scarp was formed by a single

event. Based on the local geology, they proposed a fault length of ~29 km, with

a segment boundary at the southern edge of the Black Hills (Anderson and

O'Connell, 1993). Fossett (2005) mapped the vicinity of the scarp at a scale of

1:12,000 and documented 14 strands of the scarp, with a maximum SRL of 4.5

km. This SRL would indicate a potential of M_w 5.7 (Fossett, 2005). Fossett's

(2005) map does not show the fault extending southward beyond the visible

scarp, although he did acknowledge this as a possibility.

Geochemical studies by Weber and Smith (1987) indicated that the Boulder

City pluton (BCP) was related to the volcanic rocks in the McCullough Range and

Eldorado Mountains. As a result, they concluded that the BCP had been

displaced along the sinistral EVF between 10 and 15 Ma (Weber and Smith,

1987). Weber and Smith (1987) proposed a structural model wherein extension

15

in the McCullough Range and Eldorado Mountains occurred along W-dipping

normal faults that soled into a single detachment fault, with the EVF acting as an

accommodation zone between the two ranges.

Gravity and aeromagnetic studies by Langenheim and Schmidt (1996)

estimated the average thickness of Eldorado basin sediments to be ~300 m, with

the deepest portion of the basin (~1800 m) at the northern end of the Eldorado

Valley playa. Both models show estimated basin thickness by using the

basement gravity field in combination with densities of sediments and volcanic

rocks at varying depths (Figures 7 and 8). Wells in the Eldorado Valley do not

penetrate pre-Cenozoic units and were therefore not utilized in the Langenheim

and Schmidt models (1996). Utilizing average densities for the state of Nevada,

the preferred model shows a steep thickness gradient along the entire Black Hills

mountain front, suggesting that the BHF may extend the entire length of the

Black Hills (Figure 7). An alternative model utilizes densities based on well 78E

in the Las Vegas Valley in an effort to utilize local density values (Figure 8).

However, the geologic units in the Las Vegas Valley differ significantly from those

in the Eldorado Valley (Tabor, 1982). This alternate model shows the steep

thickness gradient in a more southerly orientation, suggesting that the BHF may

continue southward, but not along the mountain front (Figure 8) (Langenheim

and Schmidt, 1996). Langenheim and Schmidt (1996) interpreted this steep

gradient as an indicator of the EVF location, hypothesizing that the EVF was a

continuation of the sinistral Hamblin Bay fault, which is part of the LMFS.

Langenheim and Schmidt (1996) further suggested, as did Weber and Smith

16

(1987), that the EVF may act as an accommodation structure between faults in the Eldorado Mountains and those in the McCullough Range and River Mountains. This interpretation is in contrast with Slemmons et al. (2001), who hypothesized that the BHF is a continuation of the Mead Slope fault (MSF), which is also part of the LMFS.

Scarp profiling and diffusion equation modeling have been utilized to estimate surface displacement and ages of events along the scarp. Typically, the topographic profile of a scarp is measured with a Total Station, and then scarp ages are calculated using the assumption that erosion of the scarp occurs as a process of sediment diffusion (Ostenaa, 1984). Utilizing this method, Werle and Knight (1992) determined that the maximum surface displacement was ~2 to 7 m and concluded that the BHF (which they called the Eldorado Valley fault) was 5500 to 8200 ya. Fossett (2005) measured beveled scarp heights at a maximum of 3.49 m, indicating that the scarp was formed by multiple events.

Geophysical methods have been used in an effort to determine possible locations of the BHF and EVF in the subsurface. Werle and Knight (1992) acquired gravity and seismic refraction data ~5 km SSW of the scarp, but the results of that study in terms of locating the fault trace were inconclusive. Fossett et al. (2003b) performed Spectral Analysis of Surface Waves (SASW), Multi-channel Analysis of Surface Waves (MASW) and collected seismic refraction data, which suggested that offset on the BHF was as much as 1.2 m greater than offset indicated by the scarp. Fossett et al. (2003b) also collected magnetic data

17

orthogonal to the scarp. These data were used as a basis for determining the location of the paleoseismic trench for Fossett's (2005) study.

Measurements acquired by Fossett (2005) in an excavated paleoseismic trench provided magnitude estimates for events on the BHF. Fossett (2005) documented 38 fault strands, with strikes of N02E to N35E and dips of 50° to 86°. Vertical displacement on these strands was from 5.1 cm to 1.98 m, which would imply that the BHF is capable of producing up to a M_w 6.8 earthquake (Fossett, 2005). These estimates disagree with those based on SRL, which would indicate a potential of M_w 5.7 (Fossett, 2005). Fossett (2005) concluded, based on geomorphic indicators, that a much greater subsurface rupture length, ~15 to 30 km, was likely.
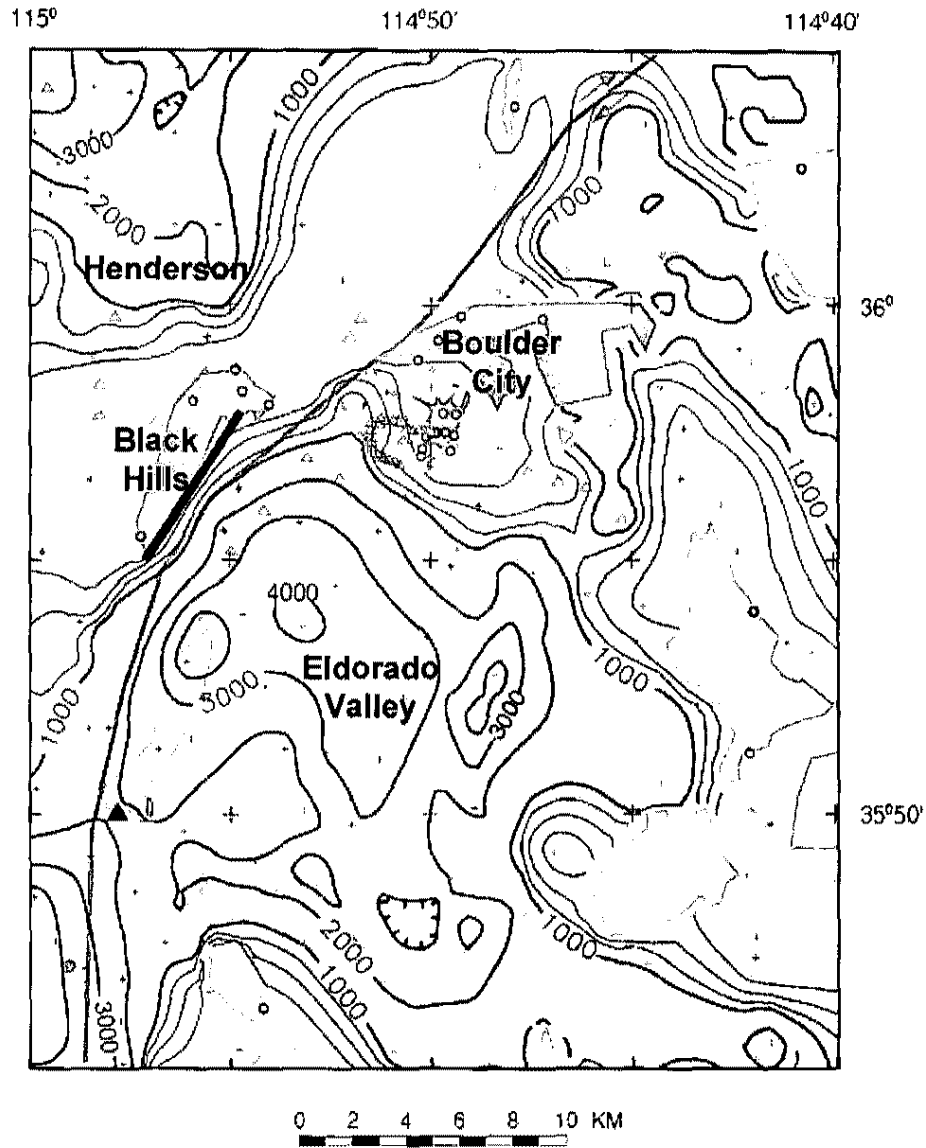
Figure 7. Langenheim and Schmidt (1996) model for basin thickness in the Eldorado Valley. This model calculates basin thickness by using the basement gravity field in combination with densities of sediments and volcanic rocks at varying depths, using average density values for the entire state of Nevada. The red line marks the approximate location of the BHF scarp. The gray line is the inferred location of the EVF. Contour lines show thickness of basin sediments in feet. Colors indicate rock types: dark pink-Miocene plutonic rocks, light pink-Miocene volcanic rocks, light yellow-Quaternary alluvium and basin fill, dark yellow-playa deposits, purple-Precambrian basement rocks. Circles indicate basement gravity stations, plus signs are previously collected gravity stations, and triangles are new gravity stations. The model shows a steep thickness gradient along the entire Black Hills mountain front, suggesting that the BHF may extend the entire length of the Black Hills.

19
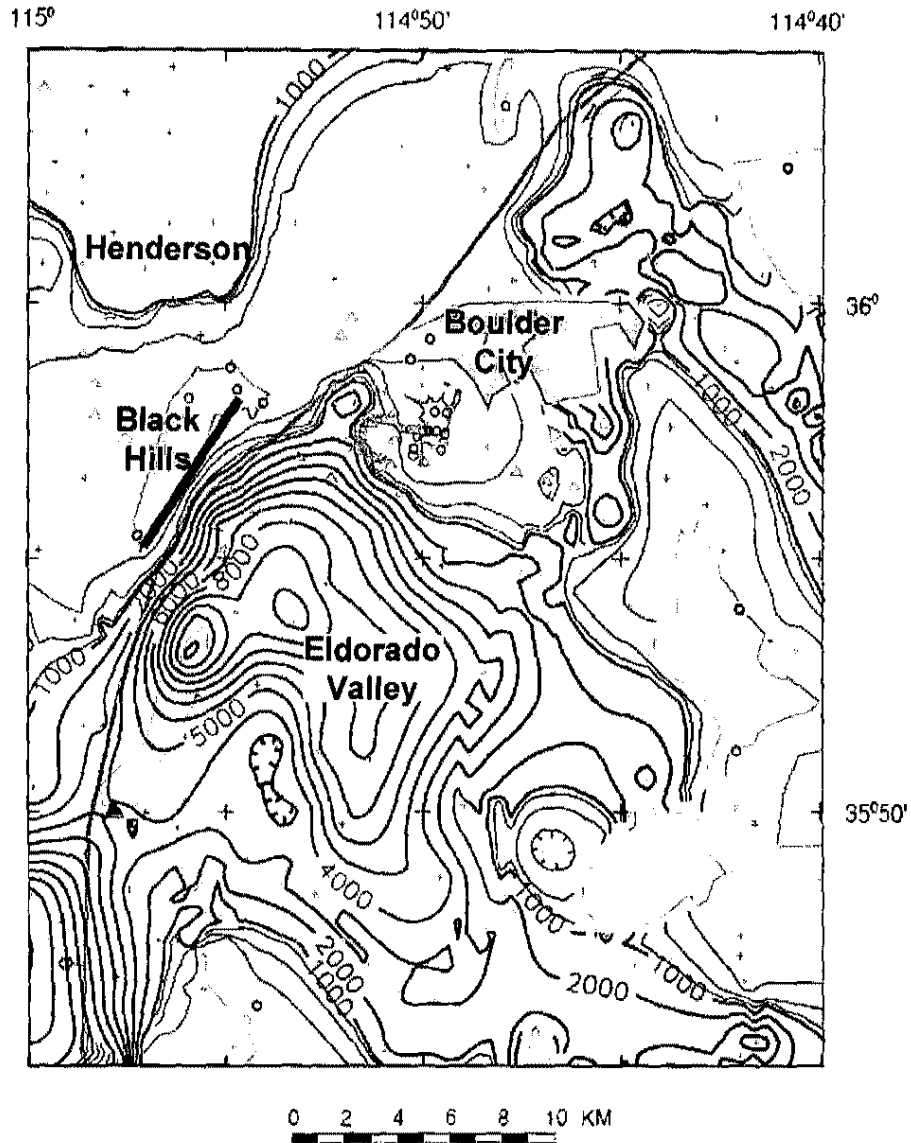
Figure 8. Langenheim and Schmidt (1996) alternate model for basin thickness in the Eldorado Valley. This model calculates basin thickness by using the basement gravity field in combination with density values based on well 78E in the Las Vegas Valley (not shown in the image) and therefore does not represent actual density values. The red line marks the approximate location of the BHF scarp. The gray line is the inferred location of the EVF. Contour lines show thickness of basin sediments in feet. Colors indicate rock types: dark pink-Miocene plutonic rocks, light pink-Miocene volcanic rocks, light yellow-Quaternary alluvium and basin fill, dark yellow-playa deposits, purple-Precambrian basement rocks. Circles indicate basement gravity stations, plus signs are previously collected gravity stations, and triangles are new gravity stations. This model shows a steep thickness gradient that bends in a southerly direction south of the BHF scarp.

20

CHAPTER FOUR

REMOTE SENSING

One method of identifying the subsurface location of a fault involves acquiring

seismic data orthogonal to the fault trace. These data are then tied to the

geology observed at the surface to produce an interpretive cross-section.

Although acquiring multiple seismic lines would be ideal, this can also be cost-

prohibitive. Therefore, the first step in this study was to choose the optimal

location to perform geologic mapping and to acquire seismic data along at least

one profile. To minimize costs and increase time efficiency, remote sensing data

were used as a reconnaissance tool. The objective was to detect linear

structures not identified by aerial photography or conventional topographical

mapping that could be related to the BHF.

Both Shuttle Radar Topography Mission (SRTM) data and spectral

reflectance data from Landsat 7 Enhanced Thematic Mapper Plus (ETM+)

imagery, downloaded from the Global Land Cover Facility (GLCF, 2005), were

utilized. Bounding coordinates were chosen to include the area mapped by

Langenheim and Schmidt (1996) to see whether linear structures could be

observed in areas with high basin thickness gradients (Appendices A and B;

Figures 7 and 8).

SRTM Data and Analyses

Raw Shuttle Radar Topography Mission (SRTM) data of 30 m resolution were

downloaded from the USGS (2002) and processed to emphasize NE-SW and N-

S linear features (Langenheim and Schmidt, 1996; Faulds et al., 2001) that may

indicate locations of the BHF trace or of fault traces that may be related to the

BHF. Raw SRTM data files typically have occasional no-data or bad data values

(Figure 9). Therefore, a topographical correction was applied to correct data

values <0 (Figure 10).

Hillshading was performed to simulate an afternoon sun angle in the SRTM

image (Figure 11). This emphasized the NE-SW linear mountain front along the

Black Hills that extends along the scarp and SW of the scarp. In addition, a N-S

linear feature is evident along most of the western edge of the image (Figure 11).

A NE-SW linear feature is also seen in the center of the Eldorado Valley (Figure

11), which is interpreted as power lines.

Further processing of the SRTM image was performed to examine potential

linear geologic features. First, a 5 x 5 pixel (each pixel is 30 m^2) edge filter was

utilized to accentuate N-S lineations (Figure 12), and an additional 5 x 5 pixel

edge filter was utilized to accentuate NE-SW lineations (Figure 13). Next,

density slicing emphasized radar differences by assigning a range of colors to

the radar values (Figure 14). Finally, a classification process was used to assign

colors to areas of the image that display similar characteristics. For this purpose,

an unsupervised K-means classification was utilized. This involved using a

simple computer-generated algorithm to cluster the pixel values into $k = 5$

aggregates (MacQueen, 1967; RSI, 2005). The computer then arbitrarily

assigned red, light blue, dark blue, yellow, and green colors to these aggregates

(RSI, 2005). This resulted in a false color image that emphasized NE-SW

lineations along the Black Hills mountain front (Figure 15). An additional N-S

linear trend can also be noted along much of the western edge of the image

(Figure 15). These lineations may indicate the presence of faults or other linear

geologic features.

Landsat 7 ETM+ Data and Analyses

Raw Landsat 7 ETM+ data were also downloaded and processed to examine

linear features that may represent the BHF or related structures. Bands 1 to 5,

and 7, which correspond to wavelengths of the visible or near infrared (NIR)

portion of the electromagnetic spectrum, were downloaded from GLCF (2005).

Band 6 consisted of thermal reflectance data, and was therefore not utilized

(Jensen, 2000). The downloaded bands consisted of raw data with separate files

for each spectral band (Figures 16 to 21). Atmospheric corrections were applied

to all bands. The bands were then merged (Figure 22), and median wavelengths

(μm) were applied to each band (Jensen, 2000). This provided a single data file

containing all bands that could be used as a starting point for further processing,

such as applying red, green, and blue (RGB) colors to selected bands to produce

a false color image (Figure 23).

In the first analysis, bands 2, 7, and 5 were assigned to RGB colors

respectively. This produced a false color image that appeared to differentiate

between lithologies and provenance (Figure 24). However, many of the igneous units had a similar greenish tint, making it difficult to distinguish between the quartz monzonite pluton of the Black Hills (adjacent to the scarp) and the Miocene volcanics directly SW of the pluton.

Next, band ratios were calculated to emphasize differences in mineralogy. To make a certain material appear outstandingly bright, the following formula was utilized:

$$R = B/A,$$

where R represents the band ratio, B represents the band that returned the highest degree of reflectance for the specified material, and A represents the band that experienced the highest degree of absorption for the specified material (Sabins, 1997). In this case, the band ratio 1/7 was utilized to emphasize the reflectance values of andesitic volcanic rocks, 3/1 to emphasize iron-rich rocks, and 7/5 to emphasize clay alteration (e.g., Short, 1984; Sabins, 1997). Assigning 1/7, 3/1, and 7/5 to RGB, respectively, resulted in a false color ratio image (Figure 25) with a narrow range of pixel values (~10 to 30 out of 255). An equalization stretch, similar to a uniform distribution stretch (Sabins, 1997), distributed these data at regular intervals across the available pixel range of 0 to 255. The result was a false color ratio image (Figure 26) that displayed a clearer differentiation between lithologies. In particular, the andesites (Figure 26) mapped by Anderson (1977) are contrasted from the altered andesites (Figure 26). In addition, the large alluvial fan south of the Black Hills pluton appears to have provenance west of the Black Hills, whereas other fans adjacent to the

Black Hills appear to have the Black Hills pluton or local volcanic rocks as their provenance (Figure 26).

A Laplacian filter was next applied to accentuate lineations in the Landsat data without respect to lithology (Figure 27). In particular, two edges of interest were found. A continuous NE-SW trending lineation is noted along the Black Hills mountain front, extending the full length of the BHF scarp and continuing without interruption along the base of the volcanic rocks to the south (Figure 27). An additional lineation at a high angle to the BHF scarp is also noted, which may indicate the presence of a fault that intersects the BHF at a high angle (Figure 27). If motion has occurred on this potential fault, this may have offset the BHF in the subsurface south of the BHF scarp.

Remote Sensing Results

Linear features noted in processed SRTM and Landsat 7 ETM+ imagery may indicate the presence of faults. As expected from aerial photographs and topographical maps, a NE-SW lineation appears in both SRTM and Landsat data along the entire Black Hills mountain front. SRTM and Landsat 7 ETM+ data did not detect additional NE-SW oriented linear geologic features in the study area. Therefore, the seismic survey was conducted orthogonal to this lineation (Figure 28).

Because a significant N-S lineation was noted in SRTM data, an additional line of interested was considered (Figure 28). This corresponded to the inferred

location of the EVF in Langenheim and Schmidt's (1996) basin thickness models, but no seismic data were acquired in this location due to time constraints. Although Anderson and O'Connell (1993) and Fossett (2005) hypothesized that the BHF may continue along the McCullough Range SW of the Black Hills, no distinct NE-SW lineation was noted at that location.

Surface geology in the area of the proposed seismic line was documented via geologic mapping (Figure 28). The map area was chosen based on the Landsat ratio imagery (Figure 26) as well as Landsat imagery with the Laplacian filter applied (Figure 27). The map area extends from the southern edge of the BHF scarp southward to ~2 km south of the proposed seismic line (Figure 28). The map area includes the secondary lineation seen in the Landsat Laplacian-filtered image (Figure 27), to examine the question of whether this lineation represents an additional fault that may offset the BHF in the subsurface.
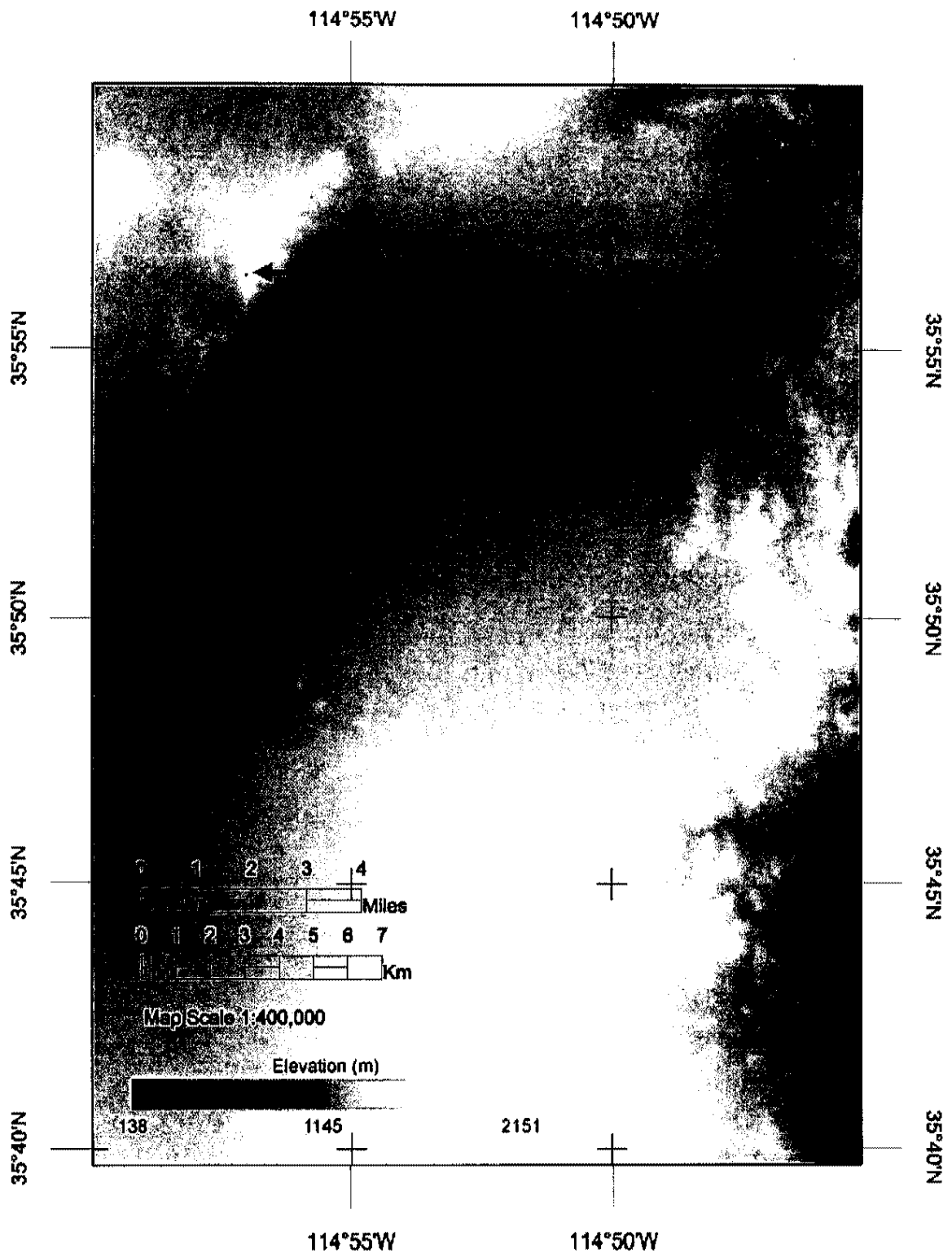
Figure 9. Raw SRTM data of the field area, downloaded from USGS (2002). Raw SRTM may contain data values <0, such as the dark spot marked by the red arrow, and must be corrected.
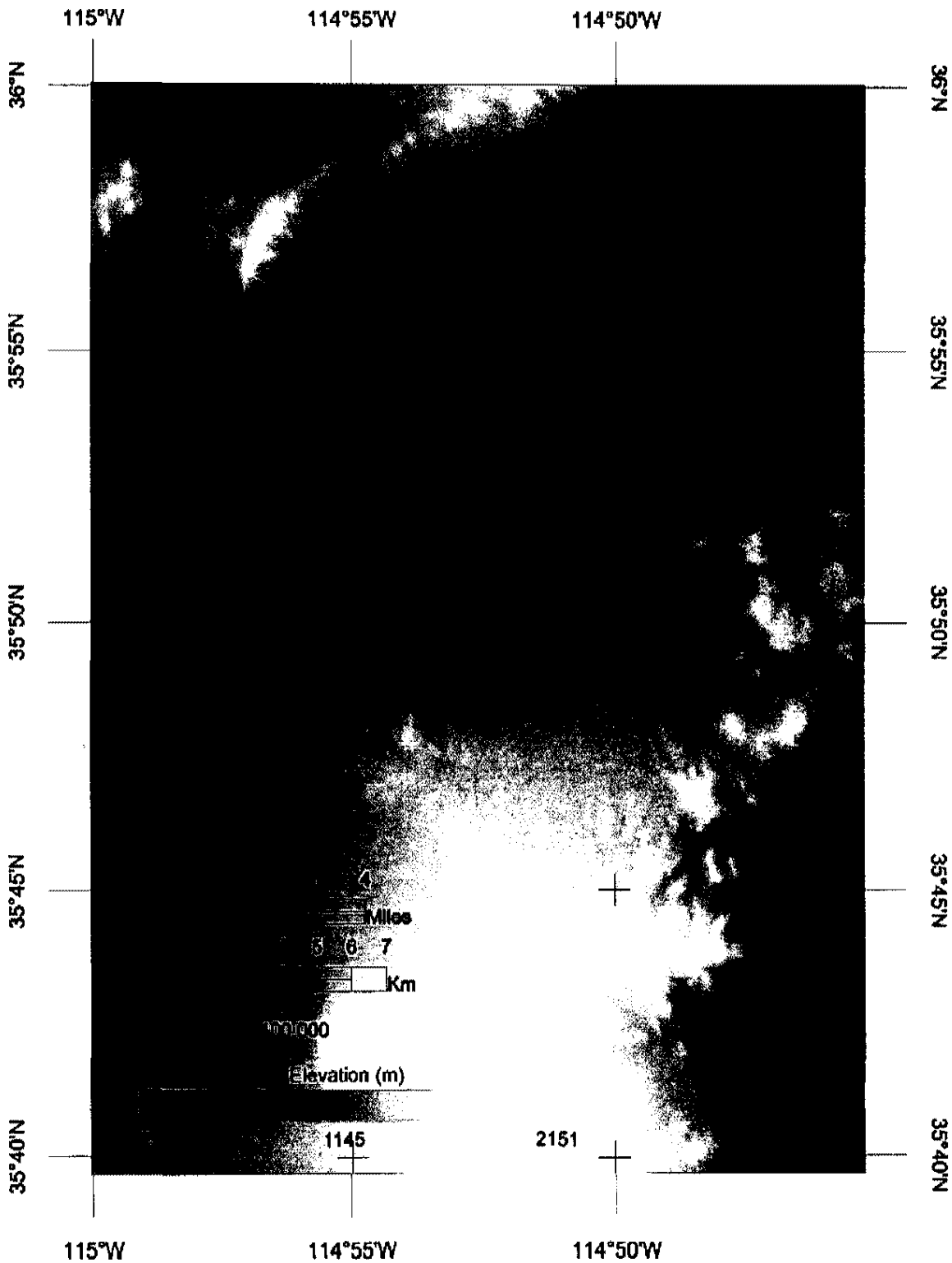
Figure 10. Corrected SRTM data of the field area (USGS, 2002). A topographical correction was applied to correct bad data values (dark spot marked by red arrow is eliminated).

28
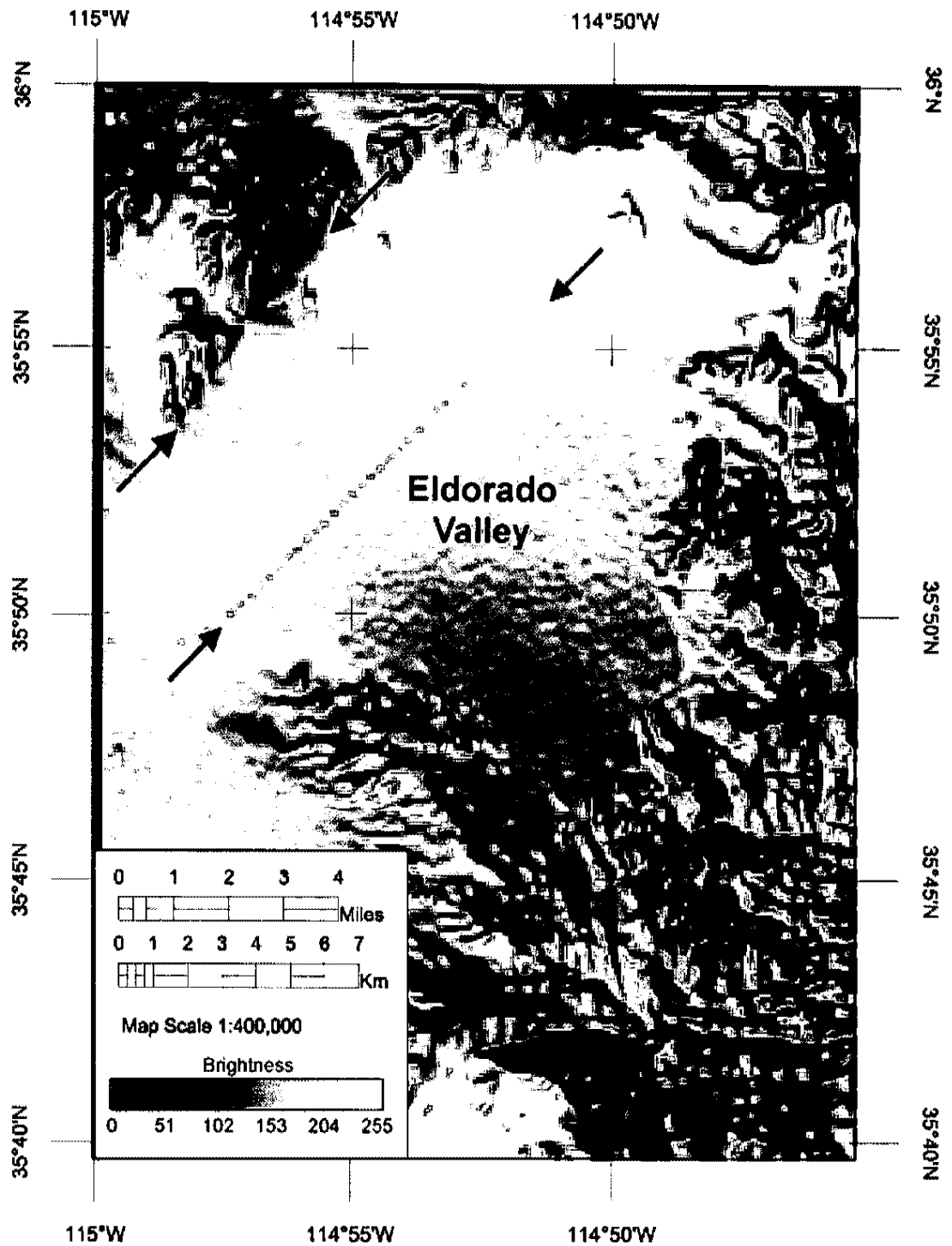
Figure 11. Shaded relief SRTM image (USGS, 2002), produced by applying a hillshade. Red arrows indicate the linear mountain front along the SE edge of the Black Hills. Blue arrows indicate the location of power lines. Pixel values display brightness of spectral reflectance, with 0 representing the darkest values, and 255 representing the brightest values.

N-S Edge Enhancement Filter

0	0	0	0	0
0	0	0	0	0
-1	-2	16	-2	-1
0	0	0	0	0
0	0	0	0	0

$30m^2$ Pixel (left label)

$30m^2$ Pixel (bottom label)

Figure 12. Edge enhancement filter kernel applied to the SRTM image to emphasize N-S lineations.

NE-SW Edge Enhancement Filter

-1	0	0	0	0
0	-2	0	0	0
0	0	16	0	0
0	0	0	-2	0
0	0	0	0	-1

$30m^2$ Pixel (left label)

$30m^2$ Pixel (bottom label)

Figure 13. Edge enhancement filter kernel applied to the SRTM image to emphasize NE-SW lineations.
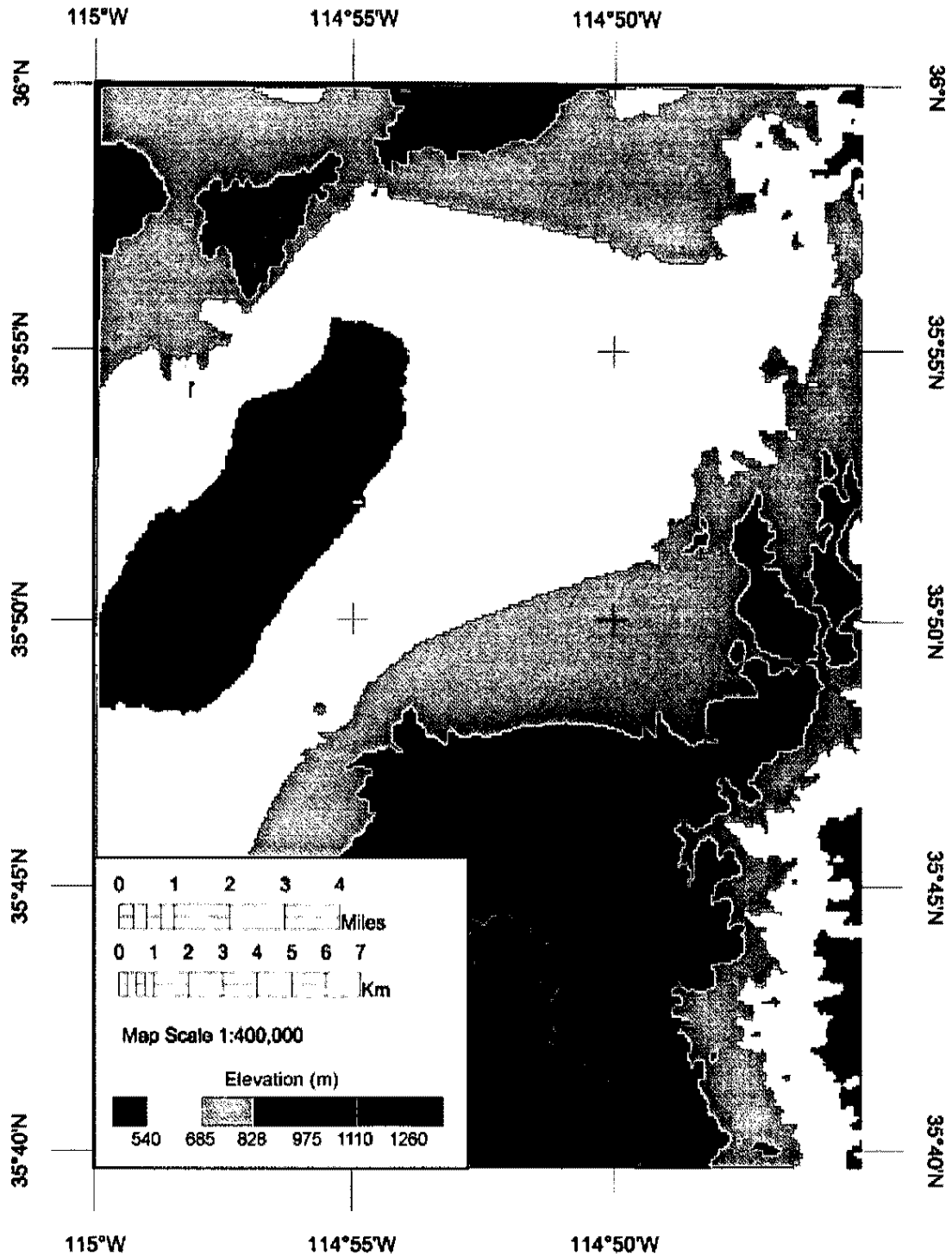
Figure 14. SRTM image (USGS, 2002) after applying edge enhancement filters (Figures 9 and 10) and density slicing. The image shows elevation differences with a NE-SW linear trend.
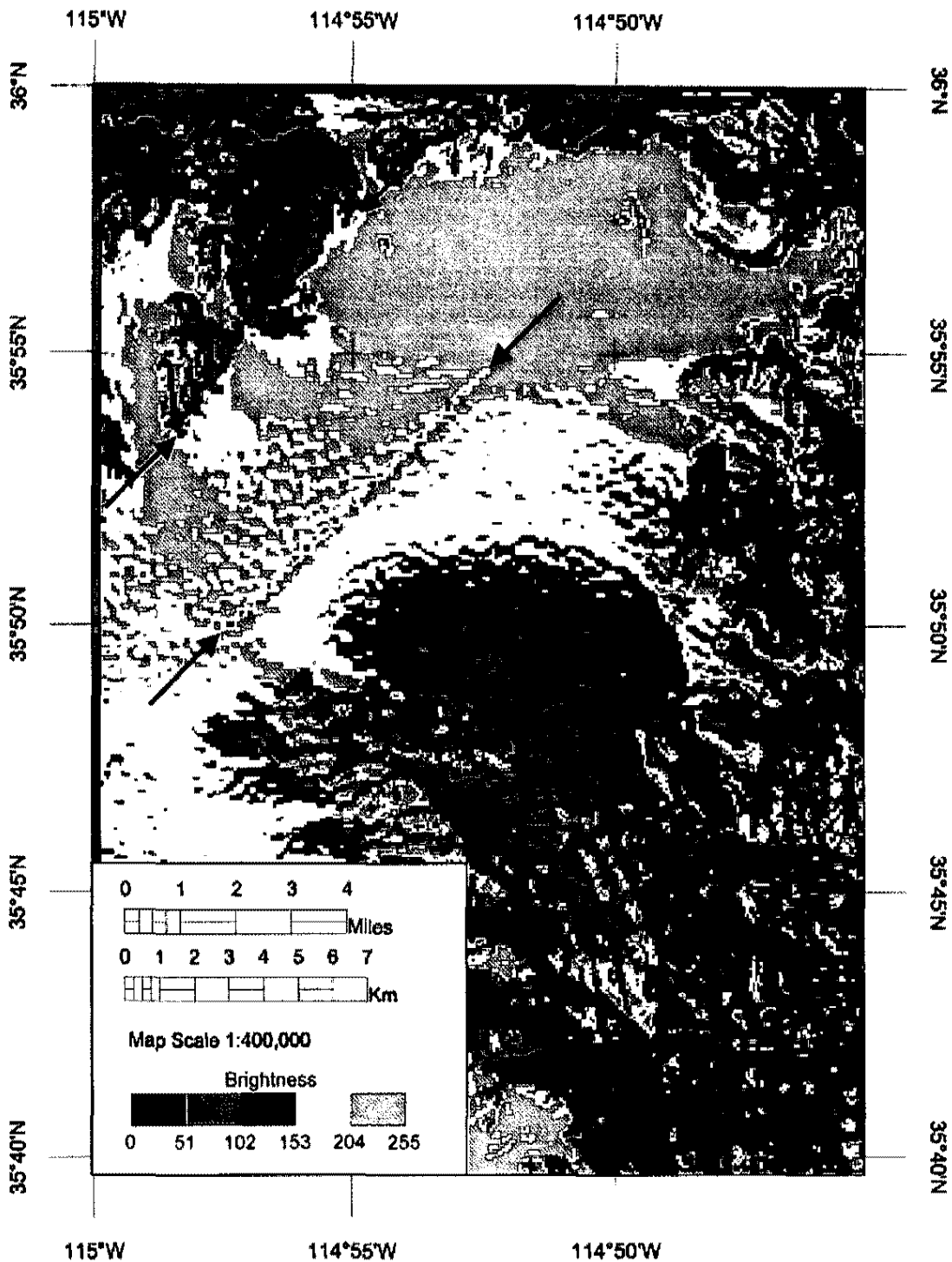
Figure 15. SRTM image (USGS, 2002) following unsupervised K-means classification based on the brightness of spectral reflectance displayed in the hillshaded SRTM (Figure 11). The image emphasizes NE-SW lineations. Black arrows indicate the linear mountain front along the SE edge of the Black Hills. Blue arrows indicate an artifact in the data, probably representing power lines.

Figure 16. Image showing raw Landsat 7 ETM+ data from band 1 (GLCF, 2005), which has a median wavelength of ~0.485 μm (Jensen, 2000). This roughly corresponds to blue light in the visible spectrum.
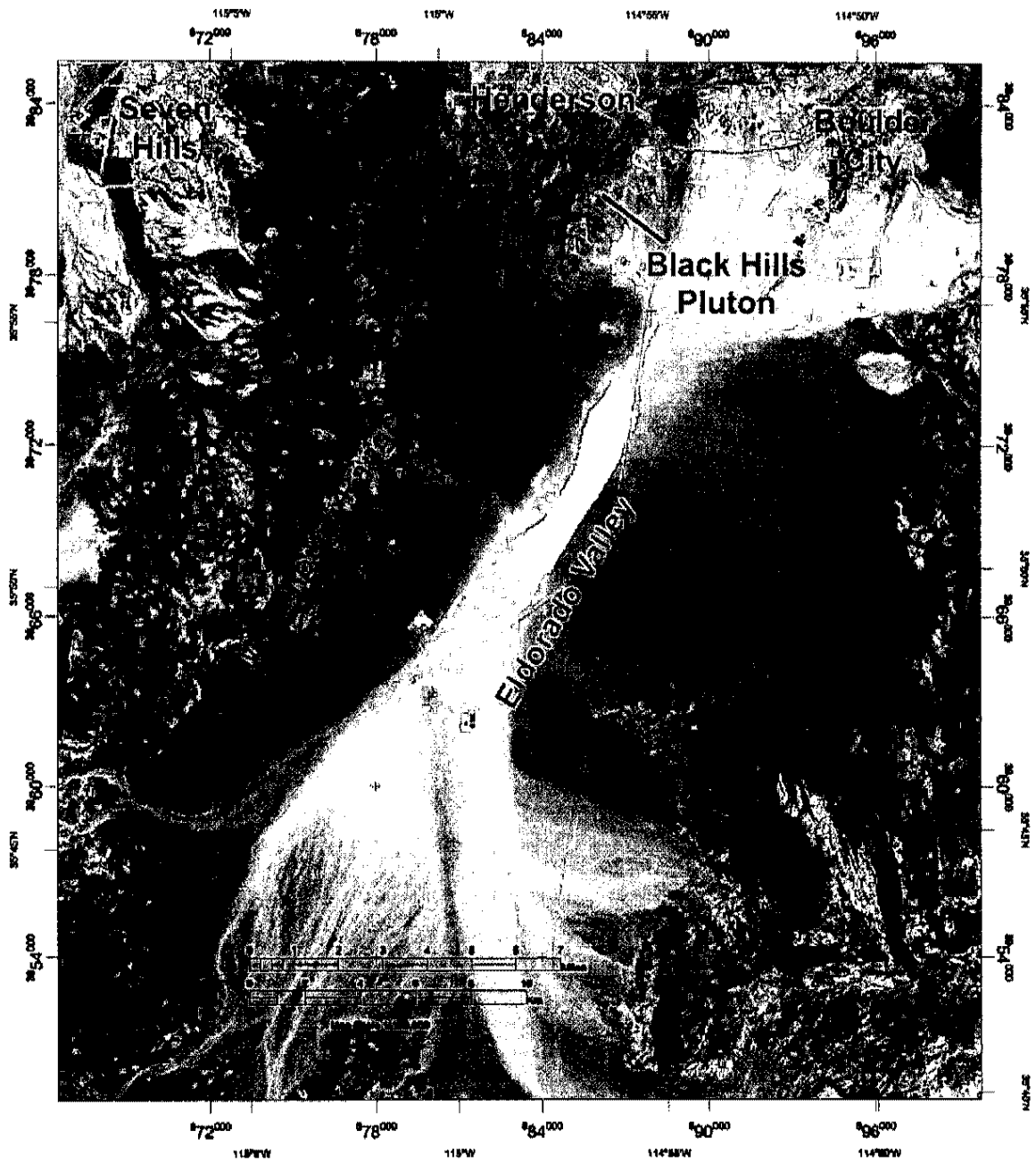
Figure 17. Image showing raw Landsat 7 ETM+ data from band 2 (GLCF, 2005), which has a median wavelength of ~0.560 μm (Jensen, 2000). This roughly corresponds to green light in the visible spectrum.
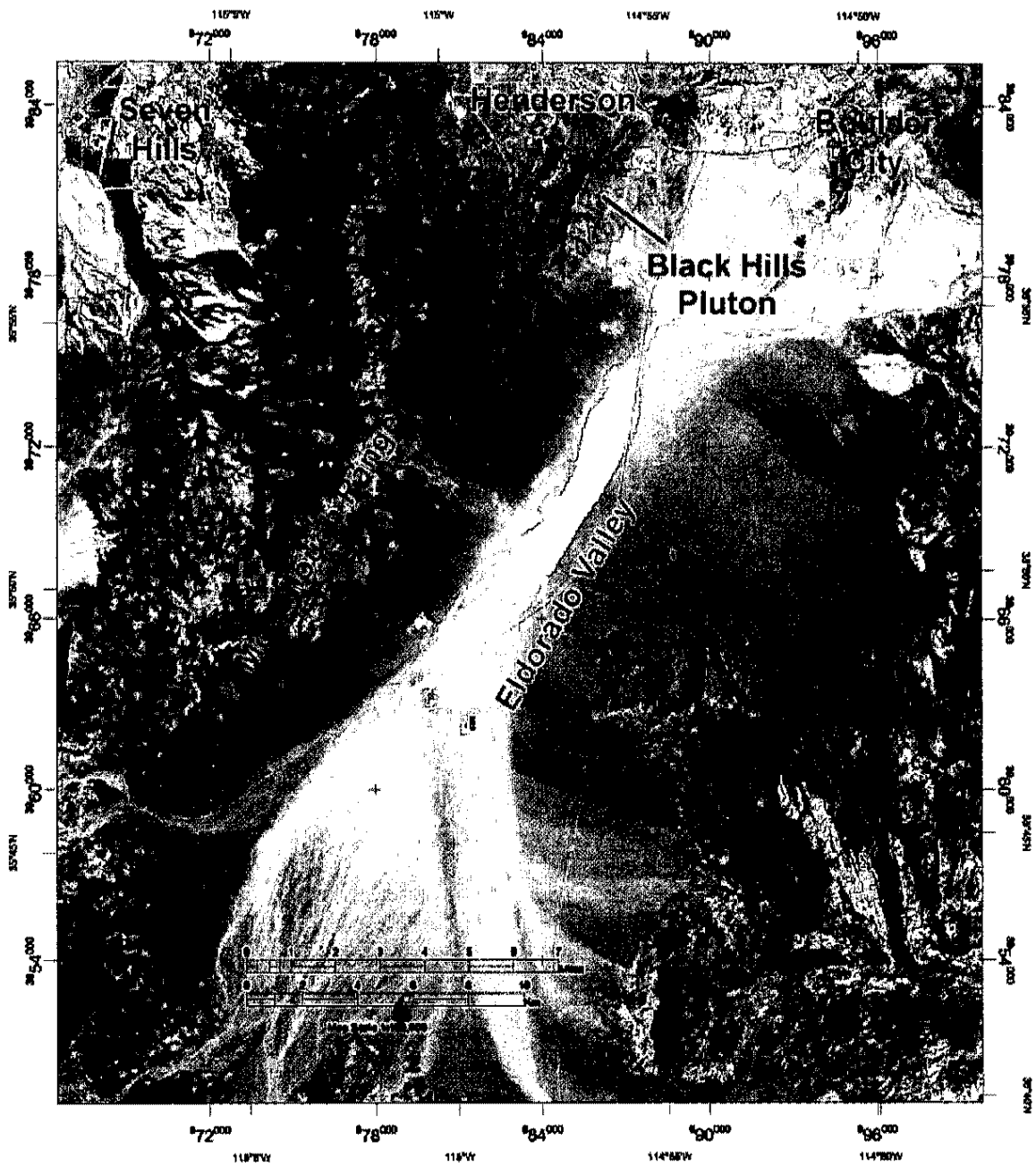
Figure 18. Image showing raw Landsat 7 ETM+ data from band 3 (GLCF, 2005), which has a median wavelength of ~0.660 μm (Jensen, 2000). This roughly corresponds to red light in the visible spectrum.

Figure 19. Image showing raw Landsat 7 ETM+ data from band 4 (GLCF, 2005), which has a median wavelength of ~0.830 µm (Jensen, 2000). This corresponds to a portion of the NIR spectrum.

Figure 20. Image showing raw Landsat 7 ETM+ data from band 5 (GLCF, 2005), which has a median wavelength of ~1.650 µm (Jensen, 2000). This corresponds to a portion of the NIR spectrum.

Figure 21. Image showing raw Landsat 7 ETM+ data from band 7 (GLCF, 2005), which has a median wavelength of ~2.215 μm (Jensen, 2000). This corresponds to a portion of the NIR spectrum.
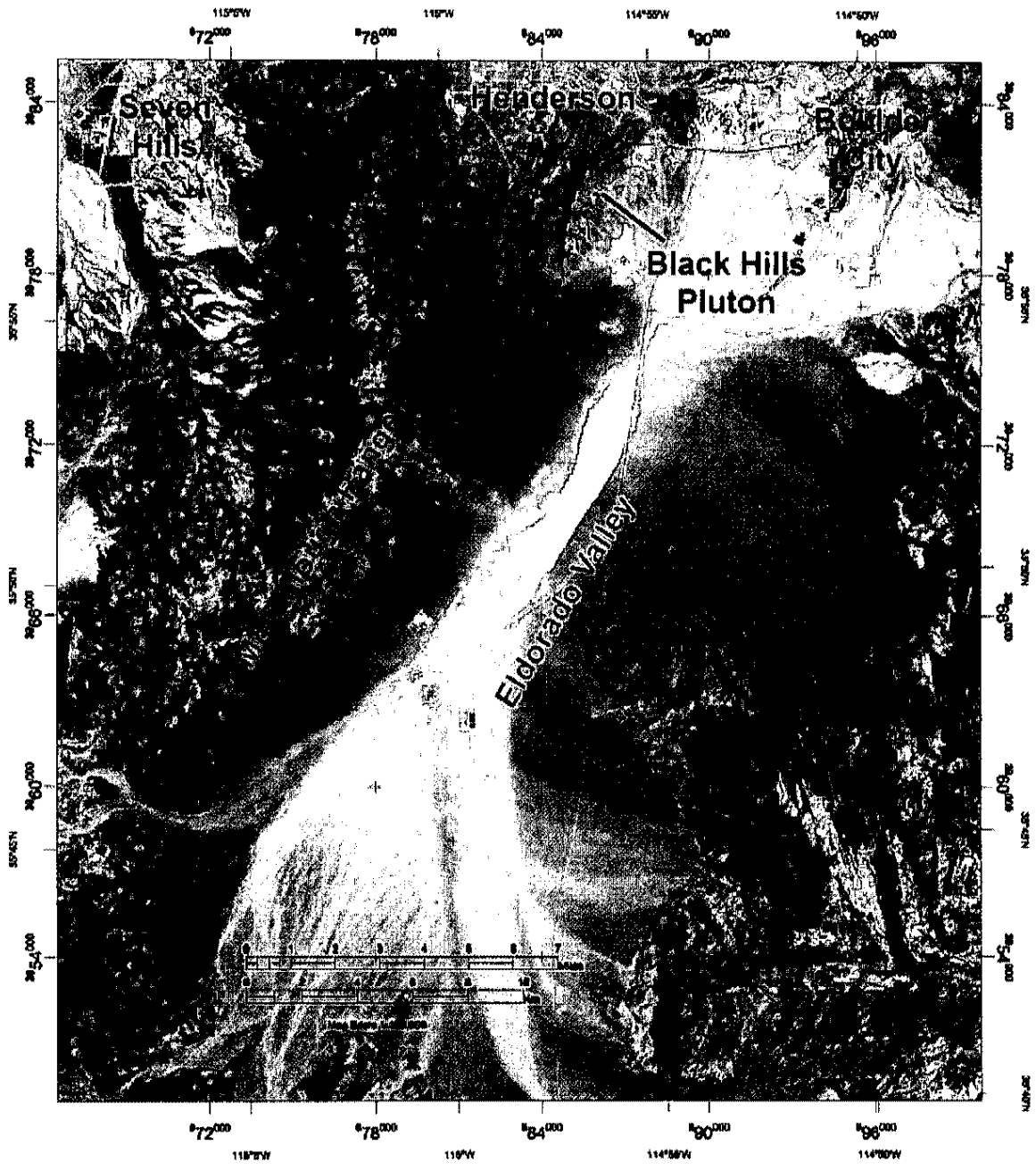
Figure 22. Landsat 7 ETM+ image (GLCF, 2005) with bands 1 to 5, 7 merged into a single data file in preparation for further processing.

Figure 23. Selected bands of a Landsat image can be assigned RGB colors to produce a false color image (GLCF, 2005). In this case, RGB are applied to bands 3, 2, and 1 respectively to produce an image that approximates true color (Landsat 321 image).

Figure 24. Landsat 7 ETM+ 275 false color image (GLCF, 2005). Differences in spectral reflectance may indicate changes in lithology as well as provenance. Abrupt, linear changes in lithology may indicate the presence of a fault or other linear geologic structure.

Figure 25. Landsat 7 ETM+ false color image with band ratios 1/7, 3/1, and 7/5 applied to RGB respectively (GLCF, 2005). Values in the image occupy a very narrow pixel range, so that only yellow and pink colors are displayed and differences in lithology are difficult to determine.

Figure 26. Landsat 7 ETM+ image with band ratios 1/7, 3/1, and 7/5 applied to RGB respectively, followed by a uniform distribution stretch to distribute values across all available pixel values (GLCF, 2005). Based on Anderson (1977) and Fossett (2005), colors in the image suggest probable differences in lithology and provenance: Reds appear to emphasize Si-altered andesites or roads and buildings; light blues reflect playa deposits and anthropomorphically disturbed surfaces; darker blues emphasize Fe-altered andesites or dacites; greens appear to reflect intermediate to mafic volcanic rocks. The Black Hills pluton is medium blue suggesting that this color may represent Miocene instrusive bodies. Sediments retain the same spectral reflectance attributes as the lithologies from which they are derived. Linear discontinuities in lithology may indicate the presence of a fault.

Figure 27. Landsat 7 ETM+ (GLCF, 2005) image with Laplacian filter applied. The dashed red line marks a linear feature that represents the potential BHF location. The dashed dark blue line marks a linear feature that may represent a fault adjacent to the BHF. Kinematic indicators on the adjacent fault may affect interpretation of the seismic data.
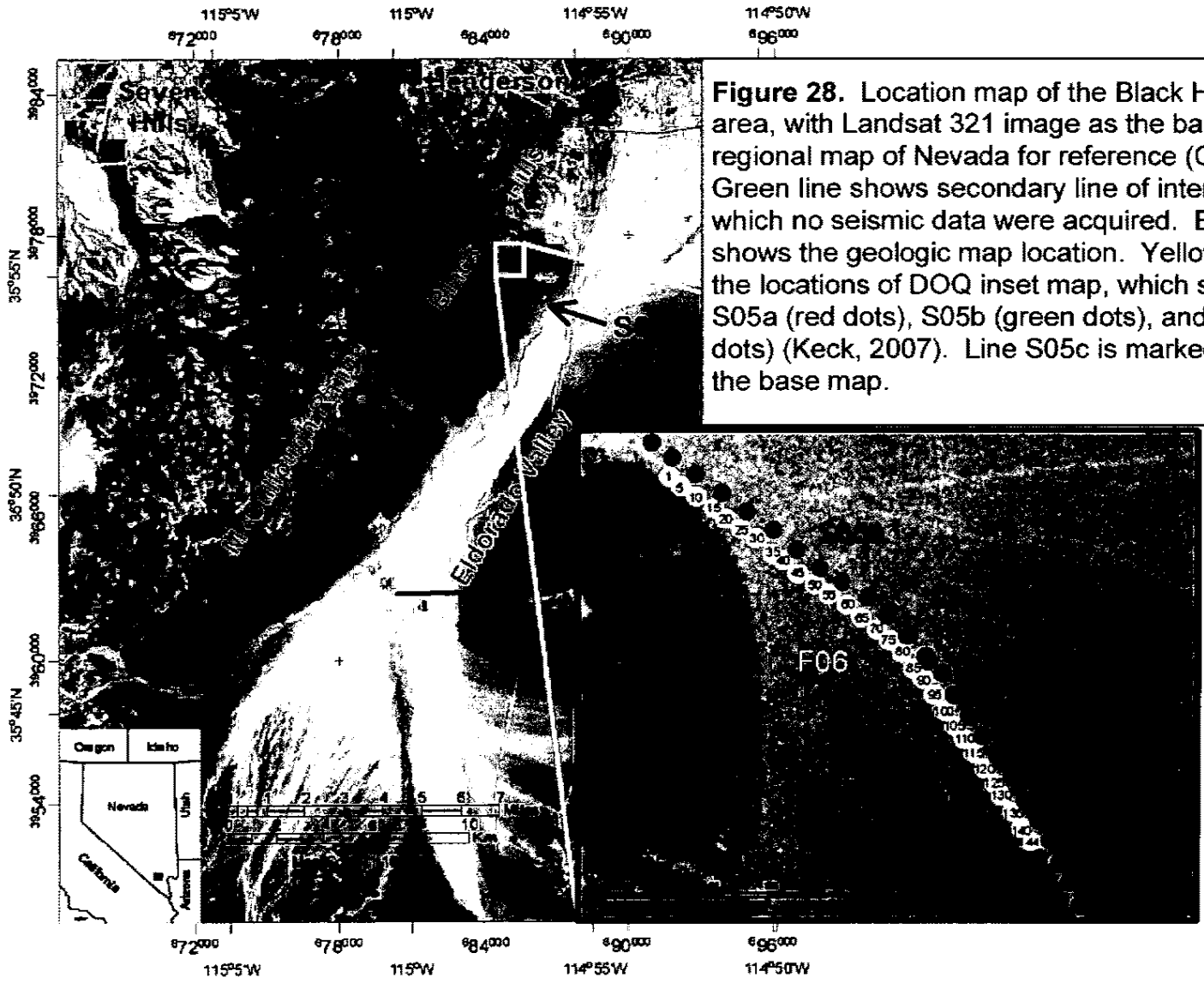
Figure 28. Location map of the Black Hills study area, with Landsat 321 image as the base map and regional map of Nevada for reference (GLCF, 2005). Green line shows secondary line of interest, along which no seismic data were acquired. Blue box shows the geologic map location. Yellow box shows the locations of DOQ inset map, which shows Lines S05a (red dots), S05b (green dots), and F06 (yellow dots) (Keck, 2007). Line S05c is marked in pink on the base map.

CHAPTER FIVE

GEOLOGIC MAPPING

Detailed mapping at the 1:12,000 scale was performed to document surface geology (Figure 29; Plate 1). Map contacts were determined based on analyses of the remote sensing data (Figure 28). The purpose was to document surface units along the suspected BHF trace as well as examine potentially related structures to the west that may have offset the BHF in the subsurface.

Data and Analyses

Geologic units in the study area range from Quaternary to Miocene in age. The youngest Quaternary unit (Qa) consists of deposits in active drainages, with clast sizes ranging from very fine sand boulder size. Qa typically occurs in the topographic low between the Black Hills pluton and the volcanic rocks to the SW, or in the topographic low along the road on which the seismic profile was located (Figure 29; Plate 1). These relatively low topographic locations form a geomorphic "gap" through which source rocks appear to have been transported to form the large fan (Qf2) that occupies the eastern portion of the map area. Qf2 contains gravel to cobble-sized subangular to subrounded volcanic clasts of red, gray or brown color, supported in a very fine sandy matrix with poorly developed desert pavement and no apparent vesicular A (AV) soil horizon.

46

Other Quaternary fanglomerate units typically consist of subangular gravel to cobble-sized clasts derived from local volcanic units, with a very fine sandy matrix. Younger fans exhibit poorly to moderately developed desert pavement with no apparent AV horizon.

Older fans exhibit well-developed desert pavement and may have a ~2 to 3 mm thick AV horizon. The fanglomerate in the extreme northern portion of the map area (Qfo1) consists of gravel to cobble-sized clasts derived from local volcanic rocks and from the Black Hills pluton. This unit is deeply dissected and is topographically higher than adjacent Quaternary units (Figure 30). Drainages exhibit a sinistral-type offset, which appears to follow fracture orientation. Older fans south of the seismic profile (Figure 29; Plate 1) are also deeply dissected and topographically higher than adjacent Quaternary units (Figure 31). A possible surface rupture is noted in the fanglomerate directly south of the NW end of the seismic profile (Qfo2), as indicated by an abrupt change in slope of the fan surface, with no change in appearance of the fan surface (i.e., desert pavement, clast type, etc.).

Miocene map units include both intrusive and extrusive igneous rocks derived from the same volcanic center (Weber and Smith, 1987). The Black Hills pluton (Ti) occupies the northeastern portion of the map area and is composed of quartz monzonite, dated by P. Gans at 14.99 ± 0.08 Ma, according to Faulds et al. (2001). The fresh surface is a light pinkish gray, and the weathered surface is a medium pinkish brown. The unit contains ~20% quartz, ~35% potassium feldspar, ~25% plagioclase, and ~20% biotite. The unit is highly fractured, with

47

fluid alteration along some fractures. The unit is cut by several mafic dikes, which tend to exhibit the same orientation as the fractures.

Miocene andesite and altered andesite (Taa) of the McCullough Range lie stratigraphically above the quartz monzonite pluton (Ti) along a sharp, intricate contact, where Ti intruded the Taa (Figure 32). Taa varies in appearance throughout the map area. In the northwestern map area, the unit forms highly fractured conical hills, is finely crystalline, and ranges from light gray to green, with a weathered surface that is tan to reddish brown. Just south of the pluton, the unit forms cliffs with columnar joints and has a weathered surface that is brown to black. Calcite and quartz crystals occur in some fractures in this area. South of the seismic profiles, chaotic flow patterns and numerous dikes are noted. Despite these differences in appearance, the unit exhibits silica alteration in these areas, in contrast with Taa at the extreme western edge of the map area, which exhibits ferric alteration. Several faults cut the Miocene units, typically striking NE-SW or NW-SE. Fluid alteration is noted in the NE-SW striking Miocene faults in the Taa SW of the pluton.

Geologic Mapping Results and Interpretations

Several features in the map area indicate that a rapid drop in base level has occurred. The toes of older fans, notably Qfo1 (Figure 30) and Qfo2 (Figure 31), have abrupt, linear edges that are topographically 2 to 3 m higher than the adjacent Quaternary units. These fans are also deeply dissected. This implies that rapid erosion occurred on these fans due to base level drop. In addition, the

48

large fan Qf2 (Figure 29) contains clasts with ferric alteration, indicating

provenance from the western map area through the topographic gap between Ti

and Taa. No fault was noted to lie along the length of this gap that could explain

the cause of a topographical low in this location, but such a gap could be the

result of erosion due to a rapid drop in base level. One potential cause of base

level drop could be rupture along the BHF.

The possible surface rupture noted in Qfo2 is located on strike with strands of

the BHF scarp as mapped by Fossett (2005). The feature in Qfo2 also lies ~100

m east of a Miocene fault striking N24W, dipping 82°W, previously mapped by

Anderson (1977). A conjugate fault strikes N12W, dipping 84°E. Whether there

is a relationship between the potential Quaternary structure and these Miocene

faults is unclear. Faults in Taa are assumed to be Miocene in age, since

Quaternary slip on these faults cannot be verified. Such preexisting structures

may provide planes of weakness along which slip can initiate, causing

reactivation of older faults. Thus, Quaternary motion may have occurred on

Miocene faults. However, because this Miocene fault is west dipping, it is

assumed to be unrelated to the BHF. Therefore, if the feature in Qfo2 is a

surface rupture but is related to the Miocene fault, then this feature would not

likely be indicative of motion on the BHF. To examine this possibility, dip

orientation of offset reflectors in the seismic section will be extremely significant.

Drainages in the northern map area appeared to exhibit some sinistral offset

(Figure 29). This offset appeared to be located on strike with a fault in Taa.

However, on further examination, these drainages follow local fracture

49

orientations, which strike N65W and N48W. Moreover, there is no evidence that suggests that the fault in Taa extends into the Qfo1. Alteration is noted along the Taa-Ti contact in this area, indicating that Ti intruded directly into the Taa unit (Figure 32). The fault in Taa near this location may therefore have occurred during emplacement of Ti and would likely be relatively short in rupture length (Boland, 1996). Therefore, the existence of a sinistral fault in this location that would affect the subsurface location of the BHF is ruled out. This would imply that the location of the BHF in the subsurface would be on strike with the previously mapped scarp (Fossett, 2005).

The overall pattern in the Miocene igneous units is consistent with the existence of a relict stratovolcano (Boland, 1996). The quartz monzonite pluton (Ti) lies adjacent to Taa that exhibits silicic alteration. The zone of silicic alteration, in turn, lies adjacent to a large zone of Taa with ferric alteration. Ti and Taa are cut by numerous dikes, which are more concentrated in the Ti and silicic-altered Taa. The dikes were not extensively mapped as part of this study. However, detailed mapping of dikes may provide an indication of the local stress field at the time that they were emplaced.
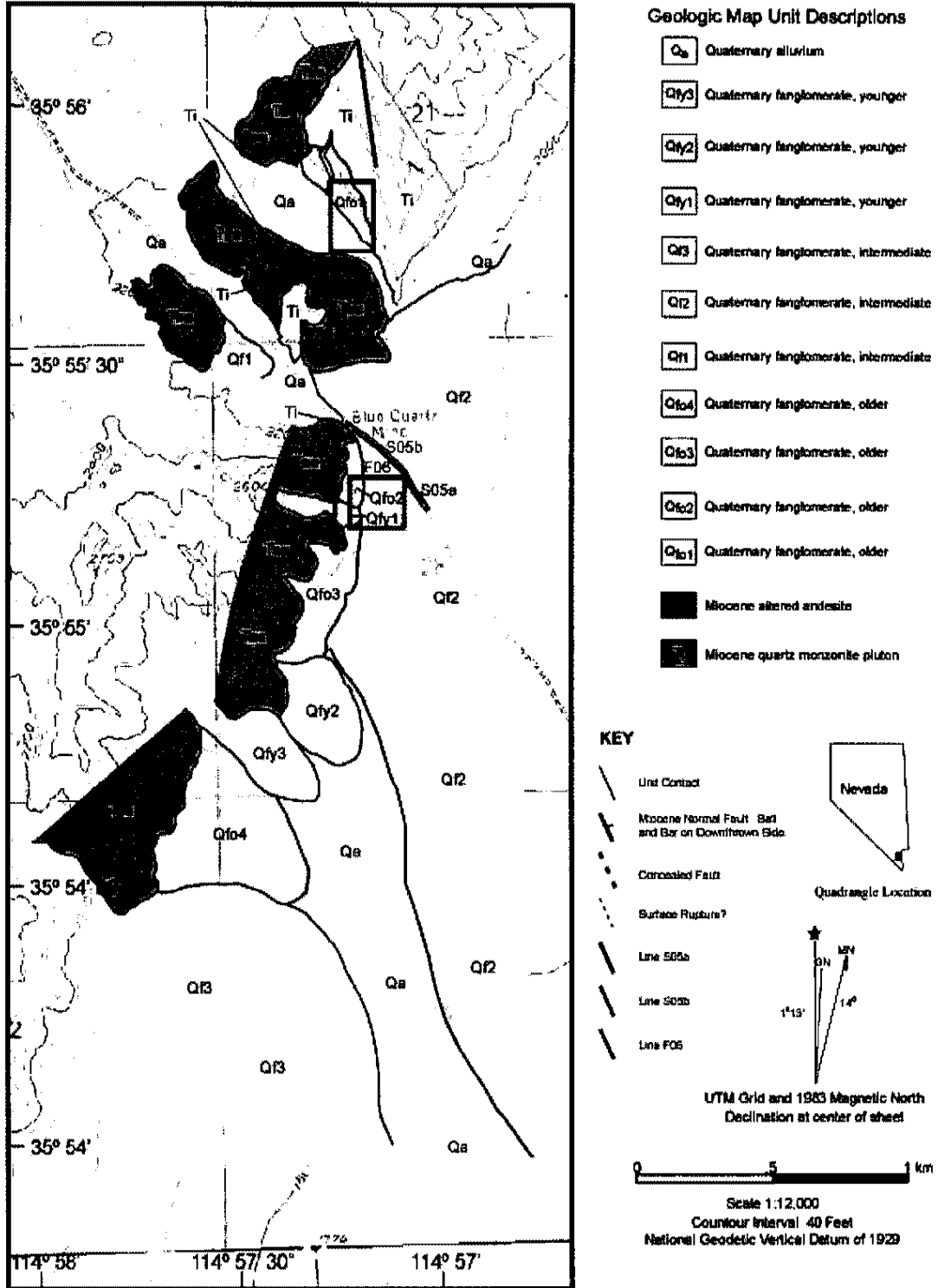
Figure 29. Geologic map of the BHF study area. See Plate 1 for complete unit descriptions. The red box shows the location of Figure 30. The blue box shows the location of Figure 31. The red star shows the location of Figure 32.

Figure 30. Photo looking E, taken in the northern geologic map area (Figure 29), with power lines for scale. The foreground shows Qa and Qfo1 (left). The main Black Hills pluton (Ti) is in the left background. Taa appears in the background on the right. The surface of Qfo1 is topographically higher than the Qa.

Figure 31. Photo looking NW, taken south of the seismic profiles (Figure 29), with vehicle for scale. Qfo2 appears in the left foreground, and Qf2 in the right foreground, with vehicle parked on the road for scale. The background shows Taa (left and center) and Ti (right). The surface of Qfo2 is topographically higher than Qf2.

Figure 32. Photo of the Ti/Taa contact found N of Qfo1, with mechanical pencil for scale. Note the grainy appearance of the Ti in contrast with the smoother surface of the Taa. The contact is sharp and nonlinear. In some locations, alteration is noted along the contact.

CHAPTER SIX

SEISMIC REFLECTION

Seismic reflection and refraction data record the travel time of an input wave between the source and the receivers (Figure 33) (e.g., Mussett and Khan, 2000). Reflection and refraction data were acquired simultaneously. However, only reflection data were processed as a part of this project. These data were analyzed to look for offset reflectors that may indicate the location of the BHF in the subsurface.

Reflection Data

The optimal location for the seismic profile was determined from the remote sensing data (Figure 28). Using a differential global positioning system (GPS), the main seismic profile was surveyed orthogonal to the suspected fault trace along the road indicated in Figure 28. An additional line of interest was surveyed along Eldorado Valley Road, ~15 km south of the scarp, but seismic data were not acquired along this profile (Figure 28). This secondary profile is located orthogonal to the projected EVF location shown in Langenheim and Schmidt's (1996) models (Figures 7 and 8).

Line S05 was acquired in three stages: S05a, S05b and S05c (Figure 28). Only S05a data were processed as part of this project (Figure 28; Appendices D

to F). Line S05b was designed to overlap S05a, but only 11 shot points were acquired on this line (Figure 28; Appendices D to F). Line S05c was designed to examine the hypothesis that the trace of the EVF may be located in the subsurface west of the playa (Figure 28). Only 29 shot points were acquired on Line S05c (Appendices D to F).

Seismic reflection data for Line S05 were acquired in SEG2 format at 5 m station spacing utilizing a vibroseis source. Source and receiver stations were co-located. Data acquisition parameters are summarized in Table 1. A 60 Hz notch filter was utilized to filter out noise from local power lines. Equipment failure limited data acquisition, and only one complete 60-channel spread (Line S05a) was acquired, with a few additional shots NW and SE of the 60-channel spread (Lines S05b and S05c) (Figure 28).

The signal recorded at each geophone included both the vibroseis sweep signal and the response of the subsurface through which the sweep signal traveled (e.g., Sheriff and Geldart, 1999; Yilmaz, 2001). Vibroseis correlation was performed to eliminate the vibroseis sweep signal from recorded signal, leaving only the subsurface response as a result (e.g., Sheriff and Geldart, 1999; Yilmaz, 2001).

Following vibroseis correlation, data were merged by source location to produce shot gathers (Figure 34; Appendix F). The resulting data exhibited severely aliased noise. Reflections can be observed, but are greatly obscured by noise. Refractions appear as early arrivals, which occur in linear fashion on successive traces in the shot gathers (e.g., Yilmaz, 2001).

Table 1. Seismic data acquisition parameters for Line S05 and related shots.

Description	Parameters
File format	SEG2
Station spacing	5 m
Geophones	40 Hz
	Vertical channel
Pilot signal	Filtered ground force
Vibroseis sweep	15 s
	30 to 160 Hz
	Linear sweep
Record length	18 s
Sample interval	2 ms
Trigger delay	0.23 ms
Assign pilot channel	Channel 1
Assign data channels	Channels 2 to 60
Notch filter	60 Hz

Although data from Line S05 are noisy, these data were utilized to determine an appropriate receiver station interval for the second seismic survey (Line F06) in order to prevent spatial aliasing. For this purpose, Equation 49 from Evans (1997) was utilized:

$$\delta x = 0.25^* v/(f/\sin\theta),$$

where δx is the maximum station spacing to prevent spatial aliasing, v is the average velocity of the subsurface material, f is the dominant frequency, and θ is the dip of the target reflector (in this case, the suspected dip of the BHF). Utilizing the data from Line S05,

$$\delta x = 0.25^*800/(45/\sin(65)) = 4.03 \text{ m}.$$

Station spacing at intervals $\leq \delta x$ will prevent spatial aliasing (Evans, 1997).

Therefore, additional data were acquired along Line F06, overlapping portions of Line S05, with adjusted parameters (Figure 28). Seismic reflection and refraction data were acquired in SEG2 format at 3 m station spacing on a 144-channel system, to produce longer offsets and further increase resolution. Shot points were located in between receiver stations, rather than co-locating shots and receivers, to maximize common midpoint (CMP) locations and prevent clipping. In addition, sweep length was shortened to 8 s and bandwidth was broadened to 20 to 160 Hz in an effort prevent excessive side lobe energy and thus reduce noise levels. Data acquisition parameters for Line F06 are summarized in Table 2.

Table 2. Seismic data acquisition parameters for Line F06.

Description	Parameters
File format	SEG2
Station spacing	3 m
Geophones	4.5 Hz
	Vertical channel
Pilot signal	Synthetic pilot
Vibroseis sweep	8 s
	20 to 160 Hz
	Linear sweep
Record length	11 s
Sample interval	2 ms
Trigger delay	0.23 ms
Assign pilot channel	Channel 1
Assign data channels	Channels 2 to 144
Acquisition filters	None

Equipment failure limited the survey to 51 shot points, including 6 off-end shots NW of the receiver line and 45 shots between receiver stations 1 to 46.

Following vibroseis correlation utilizing a synthetic pilot, data were merged by source location to produce 51 shot gathers (Figures 35 and 36; Appendices G to I). Although the data contain multiples, resulting in a ringy appearance, these data exhibit an improved signal-to-noise ratio with clear reflections and no clipping of CMP gathers.

Reflection Processing

The purpose of processing reflection data was to distinguish actual reflections from noise and to produce images that show the locations of these reflections in 2D, with distance (m) on the x-axis and two-way travel time (ms) on the y-axis (e.g., Yilmaz, 2001). The resulting reflection sections are analogous to geologic cross sections and can then be interpreted using known surface geology. Processing procedures are summarized in Figures 37 and 38.

Pre-Processing

Prior to reflection processing, procedures termed by Yilmaz (2001) as "pre-processing" were implemented (Figure 37). First, vibroseis correlation was performed on raw data. After applying a nominal geometry, data were then merged by shot location to produce raw shot gathers (Figures 34 to 36; Appendices F and I).

Spatial locations of each source and receiver were defined by Northing, Easting, and elevation (m) values, and this geometry was applied to the raw shot gathers. Corresponding GPS survey points, which were acquired at 100 m

intervals for Line S05a and were acquired at each receiver location for Line F06, were noted. For Line S05a, individual receiver and shot point locations were determined by interpolating Northing, Easting, and elevation coordinates at 5 m intervals between the known GPS survey locations. For Line F06, known GPS values were utilized for receiver location values, and shot point locations were determined by interpolating Northing, Easting, and elevation coordinates at 3 m intervals in between the receiver stations. In addition, six off-end shot locations directly NW of the receiver line were interpolated to correspond to shots 3001 to 3006. For each line, the station locations were then converted to X, Y and Z values, which correspond to changes in Northing, Easting, and elevation values, respectively. The X, Y, and Z values for Line S05a were calculated relative to receiver channel 1, and the X, Y, and Z values for Line F06 were calculated relative to shot point 3001.

Missing or poorly coupled geophones produce traces with erroneous readings that adversely affect data quality. For each shot gather, the data on these bad traces were "killed," or erased, leaving blank traces in their place (e.g., Young, 2004).

Variations in topography and in characteristics of the weathered layer can produce artifacts in seismic data (e.g., Marsden, 1993; Cox, 1999; Yilmaz, 2001). Changes in elevation along the profiles were significant enough that such artifacts might occur (Figure 39). Datum statics correction was performed to address this problem by collapsing the upper surface of the seismic data to a flat

datum located at the lower surface of the weathered layer (e.g., Marsden, 1993; Cox, 1999; Yilmaz, 2001).

Noise Analysis and Muting

Both Line S05 and Line F06 contain a considerable amount of high-amplitude coherent linear noise, which obscures reflection data. This type of noise may result from energy trapped in low-velocity near-surface layers, and is often termed "ground roll" (e.g., Sheriff and Geldart, 1999; Yilmaz, 2001). Such trapped energy travels horizontally, and thus is of little value in seismic reflection analysis (e.g., Yilmaz, 2001).

Coherent linear noise is characterized by high amplitude energy traveling at low velocities (e.g., Yilmaz, 2001). Although this type of noise occurs at low frequencies, the multiple cycles of these surface waves may cause noise to appear at higher frequencies (e.g., Sheriff and Geldart, 1999). Sampling 10 Hz windows of frequencies (e.g., 20 to 30 Hz, 30 to 40 Hz, etc.) revealed that coherent linear noise trains consistently appear in the 20 to 100 Hz frequency ranges, essentially the same frequency ranges where reflection data is expected to occur (e.g., Yilmaz, 2001). Therefore, coherent linear noise cannot be removed by low-cut filtering.

Muting is a simple method of eliminating portions of coherent linear noise (e.g., Yilmaz, 2001; Young, 2004). Tail muting erases all data at arrival times greater than a specified arrival time, thus eliminating data with steeply dipping slopes (e.g., Young, 2004). Low-velocity linear noise was identified by steeply

61

dipping slopes and high amplitudes located at the lower portion of each shot

gather (e.g., Yilmaz, 2001). These noise trains were then eliminated by picking

their earliest arrival times and performing tail muting based on these arrival

times.

Deconvolution

Deconvolution was performed to enhance temporal resolution and eliminate

multiple arrivals from the same reflection interface (multiples) (Figure 38) (e.g.,

Yilmaz, 2001; Lines and Newrick, 2004). Resolution of thin beds of subsurface

lithology, as modeled by closely spaced reflection arrivals, is dependent on

seismic wavelength, according to the formula

$$\lambda = v/f,$$

where λ is the seismic wavelength, v is the velocity of the subsurface material,

and f is the frequency of the data (e.g., Lines and Newrick, 2004). Reduction of

λ can increase temporal resolution (e.g., Lines and Newrick, 2004).

Deconvolution accomplishes this by increasing the bandwidth of the amplitude

spectrum (e.g., Lines and Newrick, 2004; Young, 2004).

Vibroseis data often include multiples, which produce an echoing, or "ringy,"

appearance (e.g., Telford et al., 1990; Yilmaz, 2001). Multiples can occur when

energy becomes trapped between subsurface layers for some duration before

reflecting back to the surface (e.g., Telford et al., 1990; Yilmaz, 2001). Because

only the first arrival of any given reflection is valid for analysis of the subsurface,

62

subsequent multiple arrivals must be eliminated to prevent artifacts from appearing in the data (e.g., Telford et al., 1990; Yilmaz, 2001).

Certain multiples may occur at regular, predictable time intervals (e.g., Telford et al., 1990). To determine these time intervals, spectral analysis of the data was performed (Young, 2004). After sorting the data according to CMP locations, several traces were picked and autocorrelated (Figure 40). The timing of the second peak of the autocorrelated traces was utilized to predict the time interval between multiple arrivals (e.g., Young, 2004). Predictive deconvolution was then performed to apply a Wiener predictive error filter to remove or minimize multiples from the seismic data (e.g., Yilmaz, 2001; Young, 2004).

The deconvolved data contained additional random noise as well as a faded appearance at far offsets. A time-variant bandpass filter was applied to reduce the appearance of random noise (Figure 38) (e.g., Yilmaz, 2001; Young, 2004). This step was followed by trace balancing, which equalizes differences in the amplitudes of near- and far-offset data (Figure 38) (e.g., Yilmaz, 2001). The result was data with both improved temporal resolution and lateral consistency in amplitudes.

Velocity Analyses

Several iterations of velocity semblance analyses and normal moveout (NMO) corrections were performed to assess subsurface velocities along the profiles (Figure 38). In cases where tomographic P-wave analysis of refraction data is not utilized to ascertain subsurface velocities, velocities must be estimated and

then gradually fine-tuned using the reflection data to produce a valid seismic section for interpretation (e.g., Yilmaz, 2001). The slopes of first arrivals in the shot gathers were used to calculate estimated velocities in the subsurface lithology (e.g., Mussett and Khan, 2000). These velocities were used as an initial guideline for picking root mean square (RMS) velocities from semblance maps (Figure 41).

CMPs at progressively longer offsets display reflections from the same layers at progressively longer time delays, producing reflections with a hyperbolic appearance (e.g., Mussett and Khan, 2000; Yilmaz, 2001). Utilizing the previous velocity estimates, these hyperbolic reflections were flattened using NMO correction (e.g., Mussett and Khan, 2000; Yilmaz, 2001).

The combination of velocity semblance analysis followed by NMO correction is a prerequisite for the residual statics correction, dip moveout (DMO) correction, and migration processes (e.g., Yilmaz, 2001). However, statics and DMO correction processes adjust the CMP gathers in such a way that inverse NMO correction, followed by additional velocity analyses and NMO correction must be performed as a consequence (Figure 38) (e.g., Cox, 1999; Yilmaz, 2001). Each iteration of velocity analysis and NMO correction produces an improved velocity estimate of the subsurface (e.g., Cox, 1999; Yilmaz, 2001).

Residual Statics Correction

To account for irregularities in the near surface, several iterations of residual statics corrections were calculated and applied to shift CMP gathers in temporal

location (e.g., Yilmaz, 2001). Residual statics calculations are dependent on RMS velocity estimates, but application of residual statics corrections produce data that requires an adjustment in velocity estimates (e.g., Cox, 1999; Yilmaz, 2001). Therefore, several iterations of residual statics corrections were performed until velocity analyses produced only minor adjustments in RMS velocity estimates (Figure 38).

Dip Moveout (DMO) Correction

NMO correction assumes horizontal reflectors in the subsurface (e.g., Mussett and Khan, 2000; Yilmaz, 2001). However, since the geologic mapping indicated that seismic data were acquired across an alluvial fan, dipping reflectors were expected (Figure 29; Plate 1). To account for dipping reflectors, DMO correction was performed on NMO corrected, offset sorted data (Figure 38) (e.g., Yilmaz, 2001). This step essentially performs a partial migration of the data prior to CMP stacking (e.g., Yilmaz, 2001). DMO correction also helped to attenuate coherent linear noise not eliminated by tail muting (e.g., Yilmaz, 2001). When DMO correction is utilized, subsequent CMP stacking can preserve the steep dips that may be associated with faults (e.g., Yilmaz, 2001).

Premigration Flow and CMP Stacking

Prior to migration, previous processing flows were re-ordered and re-applied to ensure that optimal processing parameters were utilized (Figure 38) (e.g., Young, 2004). This included utilizing the latest, most refined velocity estimate,

65

obtained following DMO correction. Following re-application of previous processes, CMP gathers were stacked to produce unmigrated seismic sections (Figures 42 and 43).

In Line S05a, the greatest number of CMP locations (fold) is 58, and is located in the center of the profile (Figure 44a). Fold decreases in a linear fashion and approaches zero at the ends of the profile (Figure 44a). In Line F06, fold remains at a maximum of ~40 along 60% of the profile, but decreases along the edges of the profile (Figure 44b). Clipping is noted in the unmigrated CMP stack of Line S05a, in the first few ms of approximately every other trace (Figure 42). Clipping is not noted in the unmigrated CMP stack of Line F06 (Figure 43). Therefore, clipping may result from co-locating shot points and receivers.

Migration

As the final step in processing, post-stack time migration was performed to adjust reflectors to a more precise location in space and time, based on second iteration velocity estimates. Phase shift migration was performed on Line S05a, following the procedures recommended by Young (2004). The resulting migrated seismic section is shown in Figure 45. However, phase shift migration does not accommodate lateral changes in velocity (e.g., Yilmaz, 2001). Therefore, Kirchhoff migration was utilized in processing Line F06 (e.g., Yilmaz, 2001). The migrated section for Line F06 is shown in Figure 46.
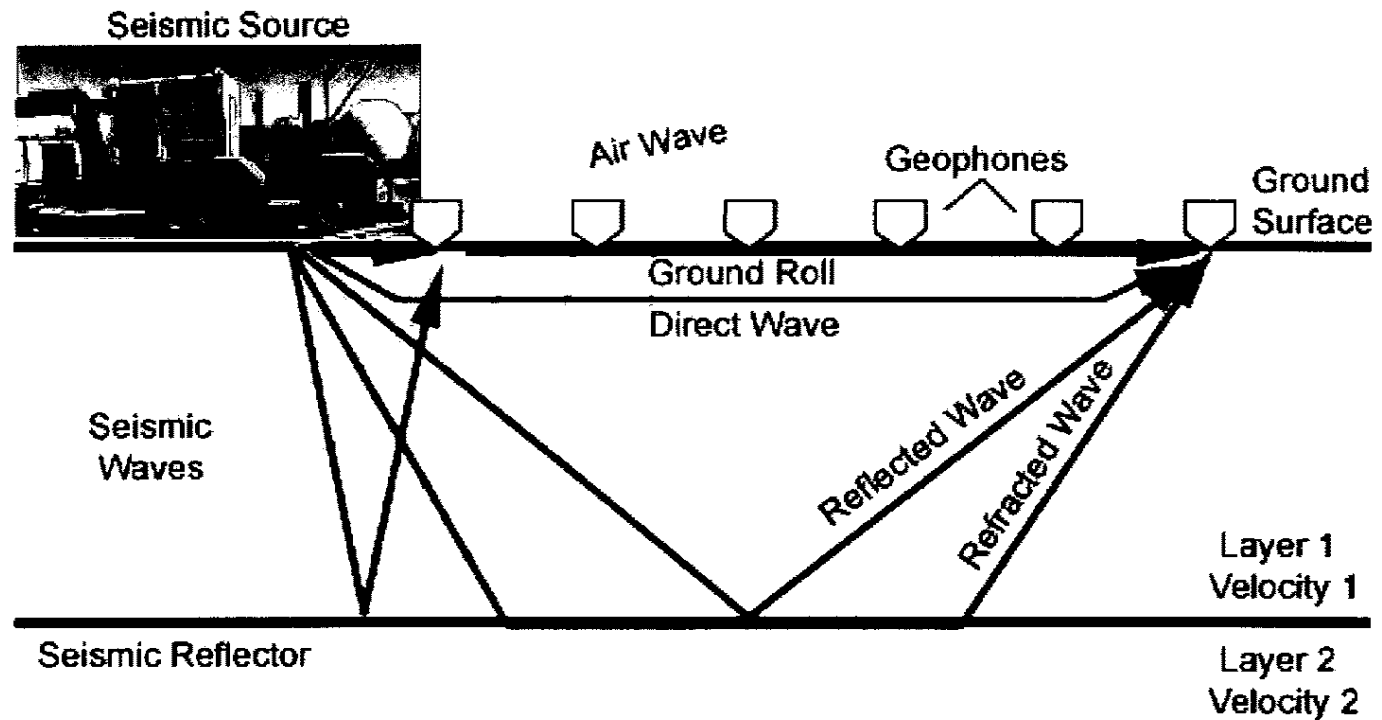
Figure 33. Seismic surveys record the travel time between the source and the receivers (adapted from Illinois State Geological Survey, 2004). Reflected waves (red arrow) were analyzed in this survey. Vibroseis photo was taken by Sandra Saldaña.

A Shot 1001

NW   Offset (m)   SE

290   250   200   150   100   50   0

Bad Traces

Coherent Linear Noise

B Shot 1058

NW   Offset (m)   SE

290   250   200   150   100   50   0
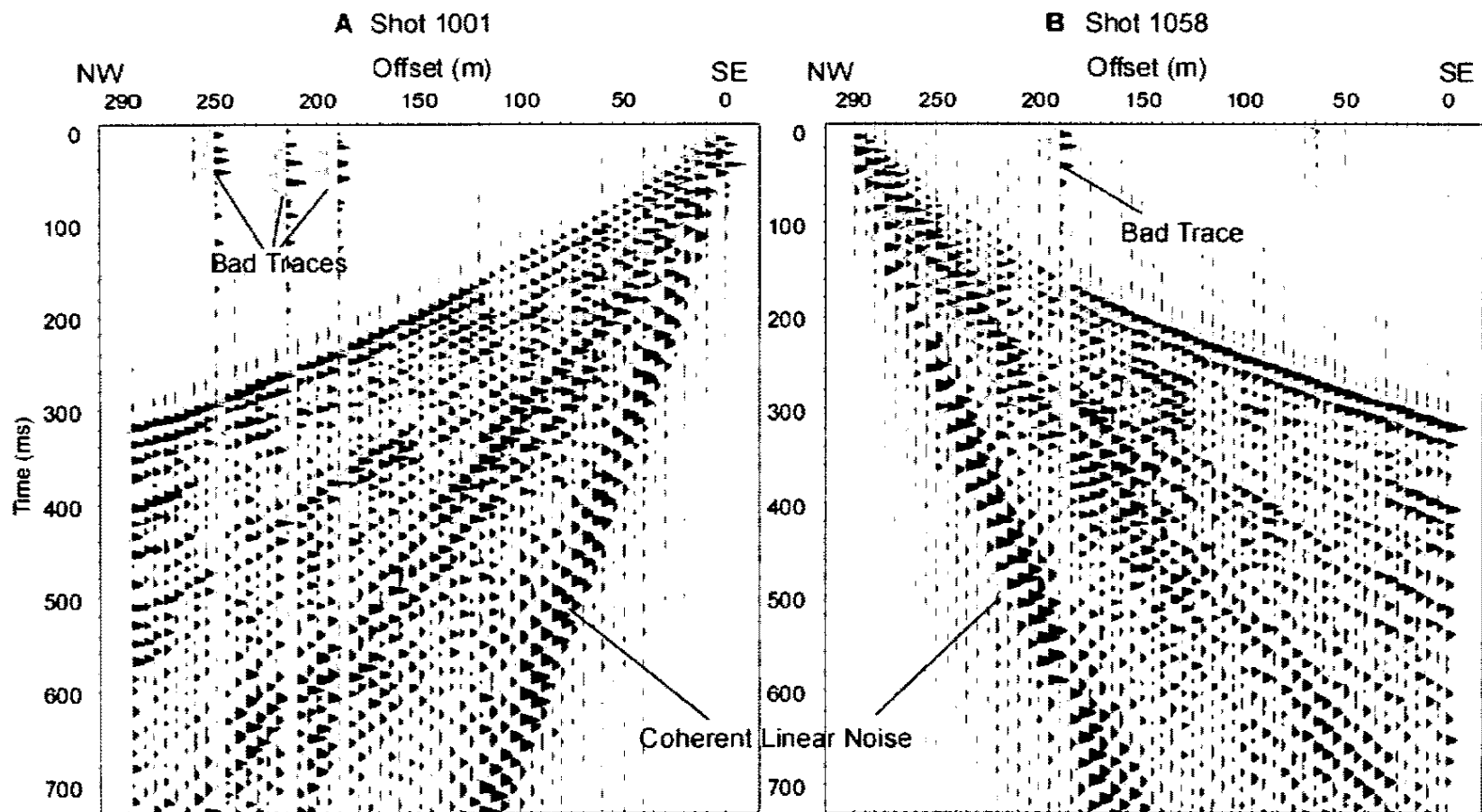
Bad Trace

Time (ms)

Figure 34. Wiggle variable area plot showing unreduced shot gathers from Line S05a, with a 60 Hz notch filter applied. A) Shot 1001. B) Shot 1058. Each plot shows offset (m) on the x-axis, and two-way travel time (ms) on the y-axis. Bad traces are from poorly coupled or missing geophones. Coherent linear noise is from ground roll.
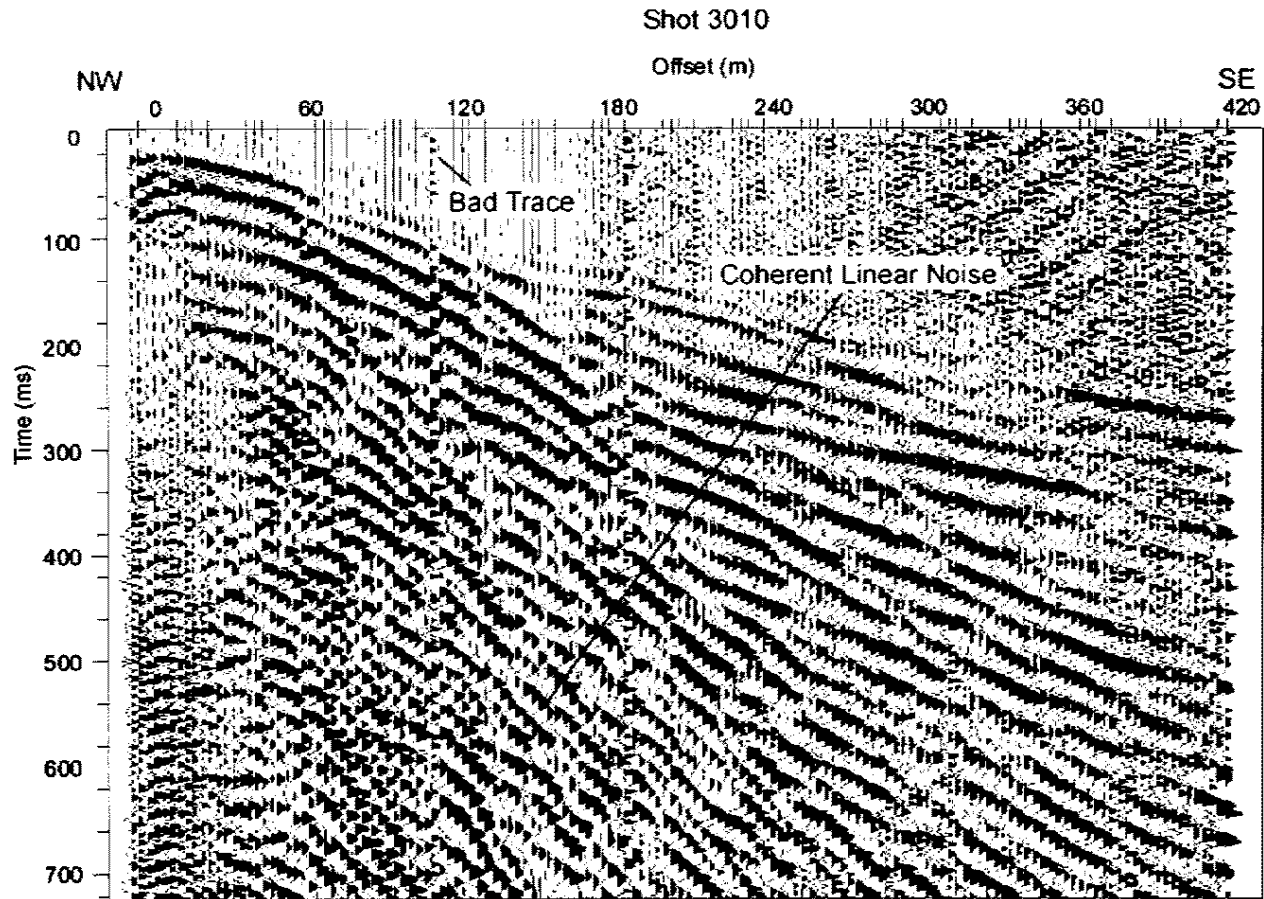
Figure 35. Wiggle variable area plot showing unreduced shot gather from Shot 3010 of Line F06. The x-axis displays offset (m), and the y-axis displays two-way travel time (ms). Data displays a ringy appearance due to multiples. The bad trace is from a poorly coupled geophone. Coherent linear noise is also noted in the shot gather.
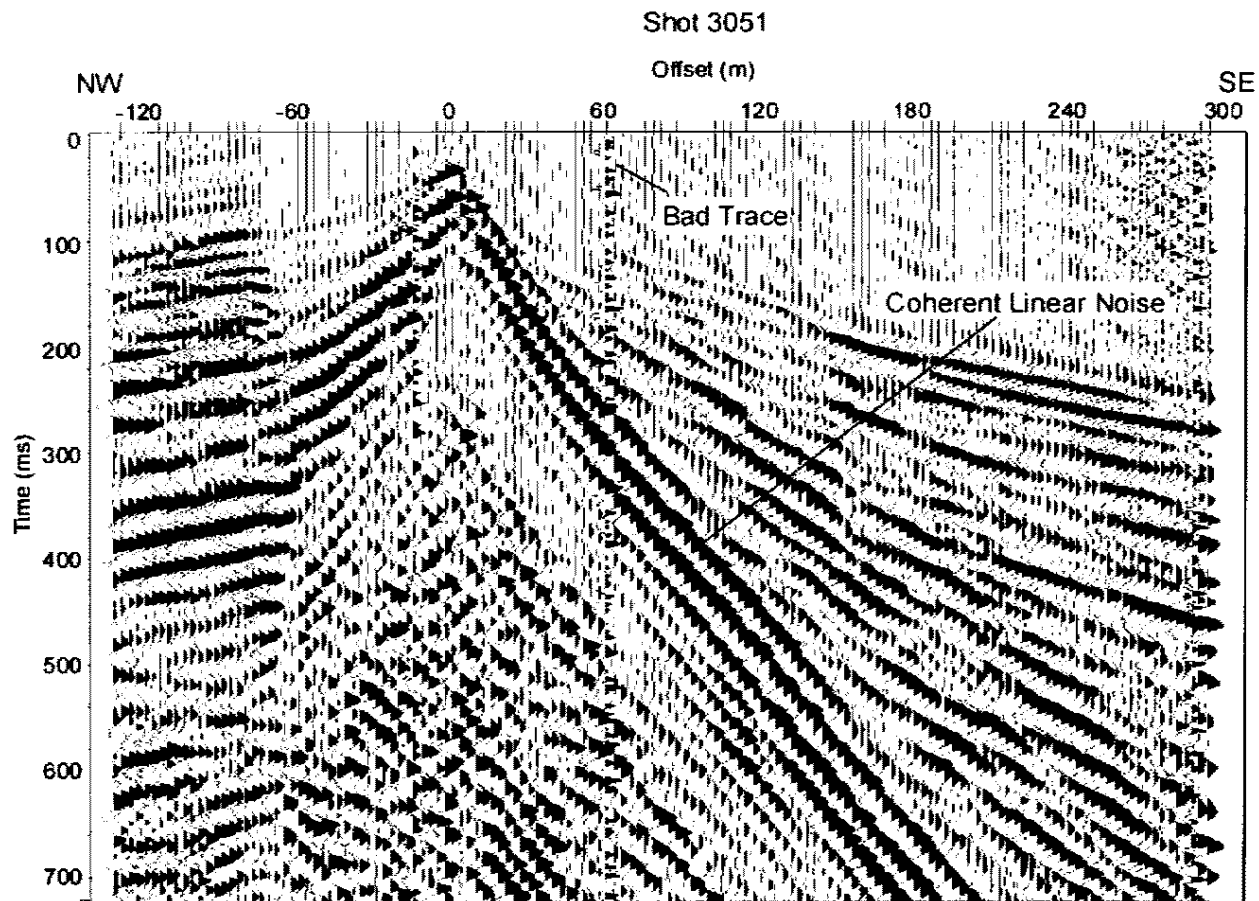
Figure 36. Wiggle variable area plot showing unreduced shot gather from Shot 3051 of Line F06. The x-axis displays offset (m), and the y-axis displays two-way travel time (ms). Data displays a ringy appearance due to multiples. The bad trace is from a poorly coupled geophone. Coherent linear noise is identified by high amplitudes and low velocities.
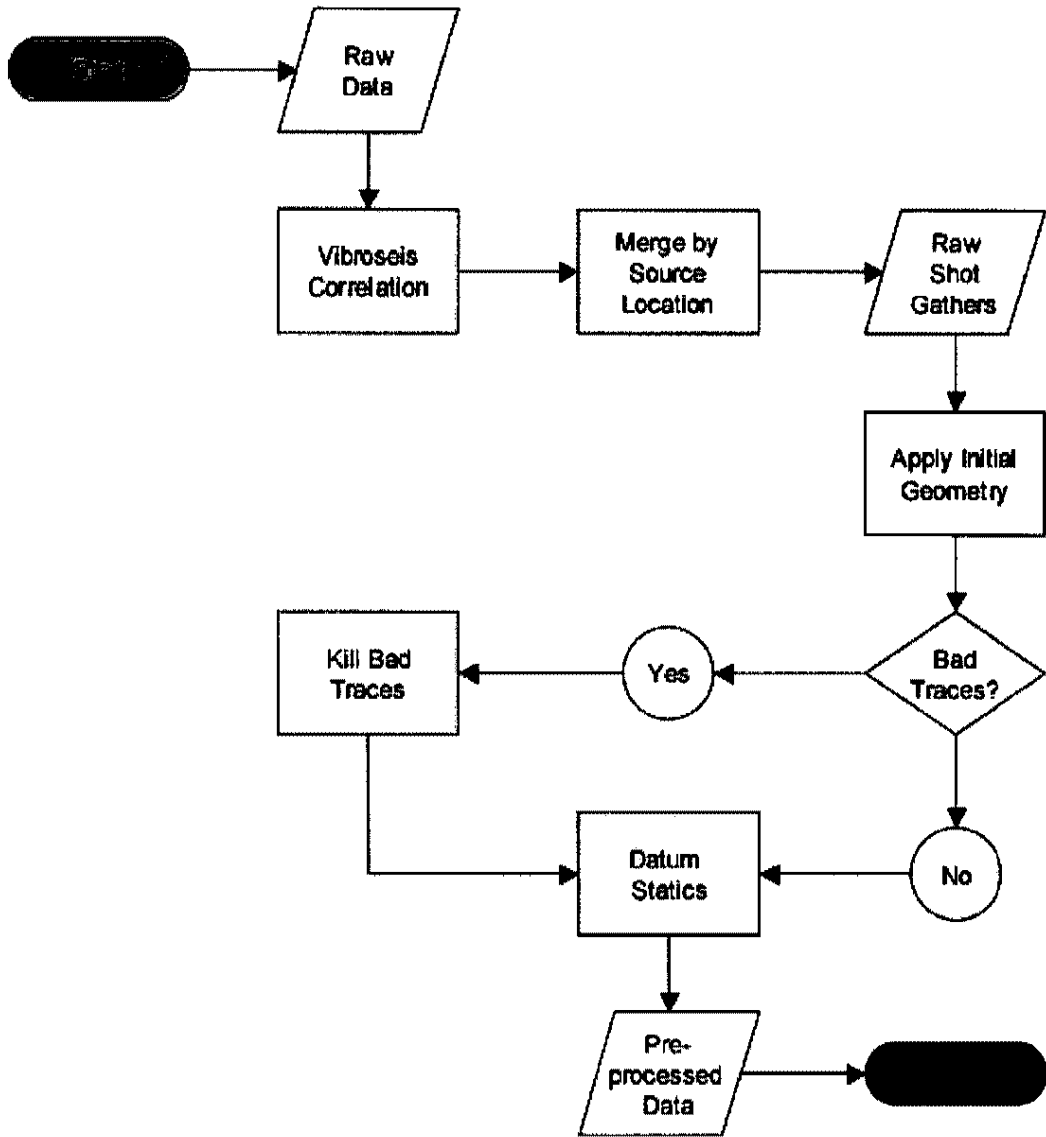
Figure 37. Simplified pre-processing flow chart, based on Marsden (1993) and Yilmaz (2001).
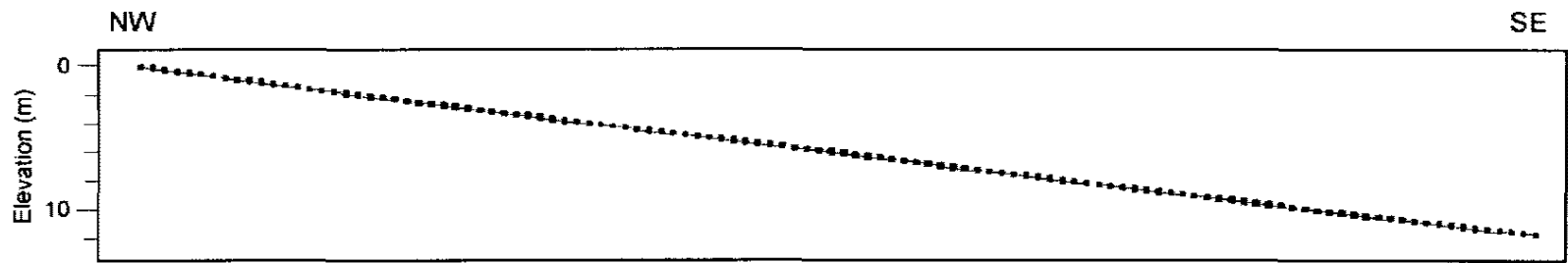
Figure 39a. Elevation plot for S05a source and receiver locations relative to shot point 1058.
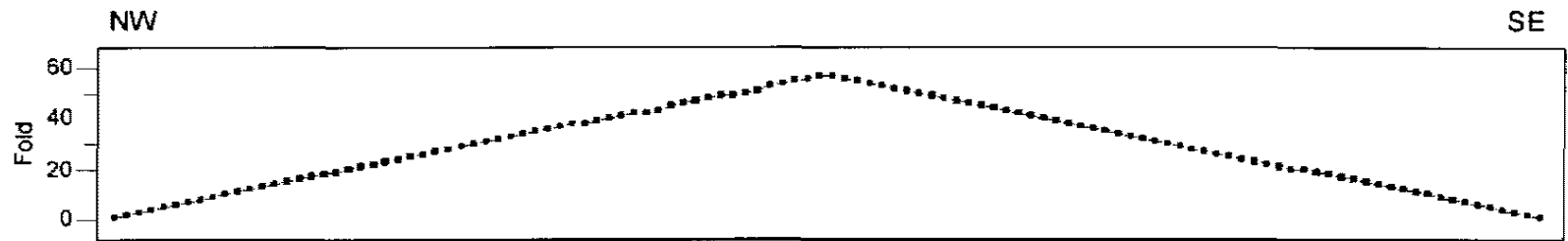
Figure 39b. Elevation plot for F06 receiver locations relative to shot point 3001.
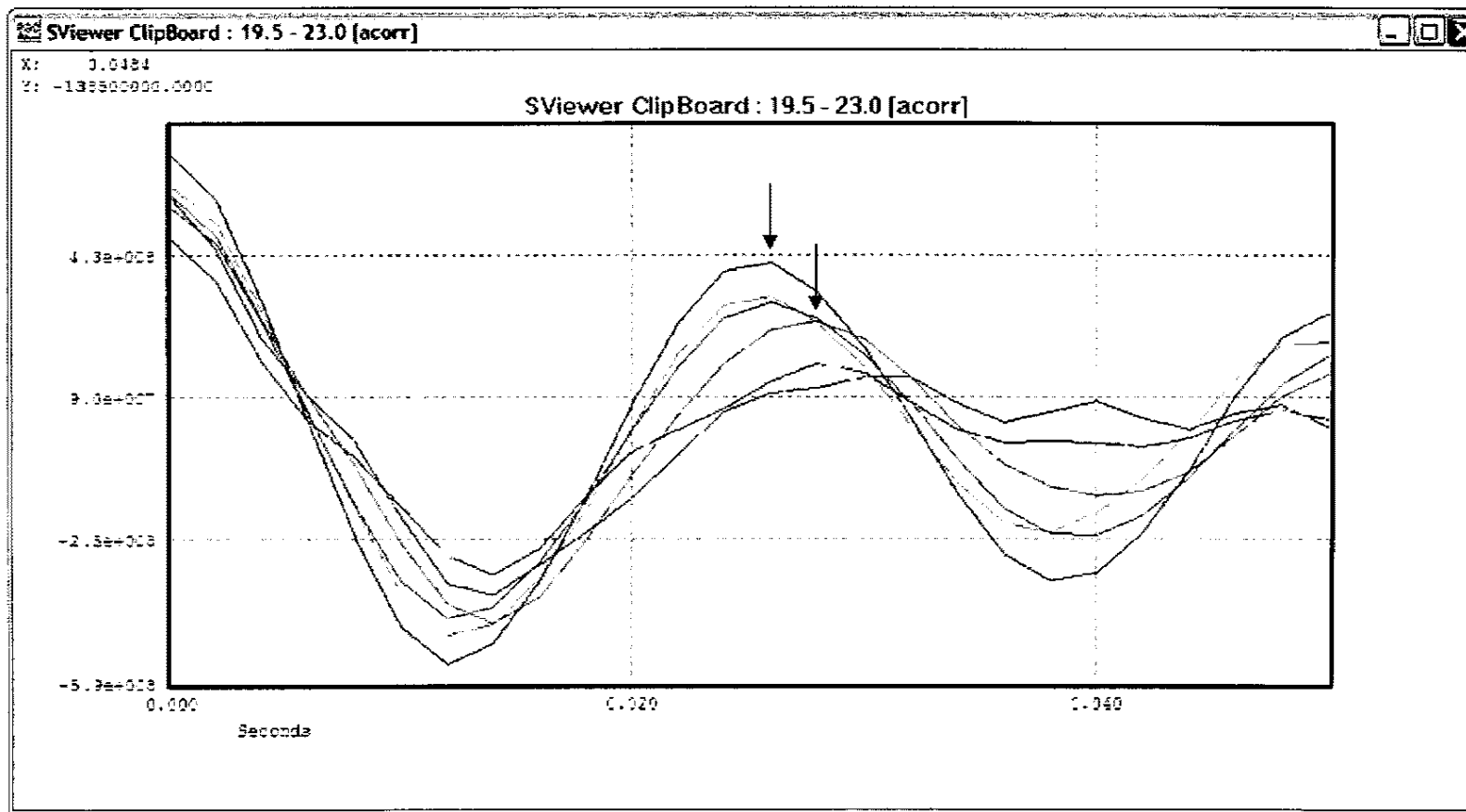
Figure 40. Autocorrelation of traces from F06. Lag time (red arrows) of the second peak (25.9-27.9 ms) was used in predictive deconvolution to determine time intervals between multiples.
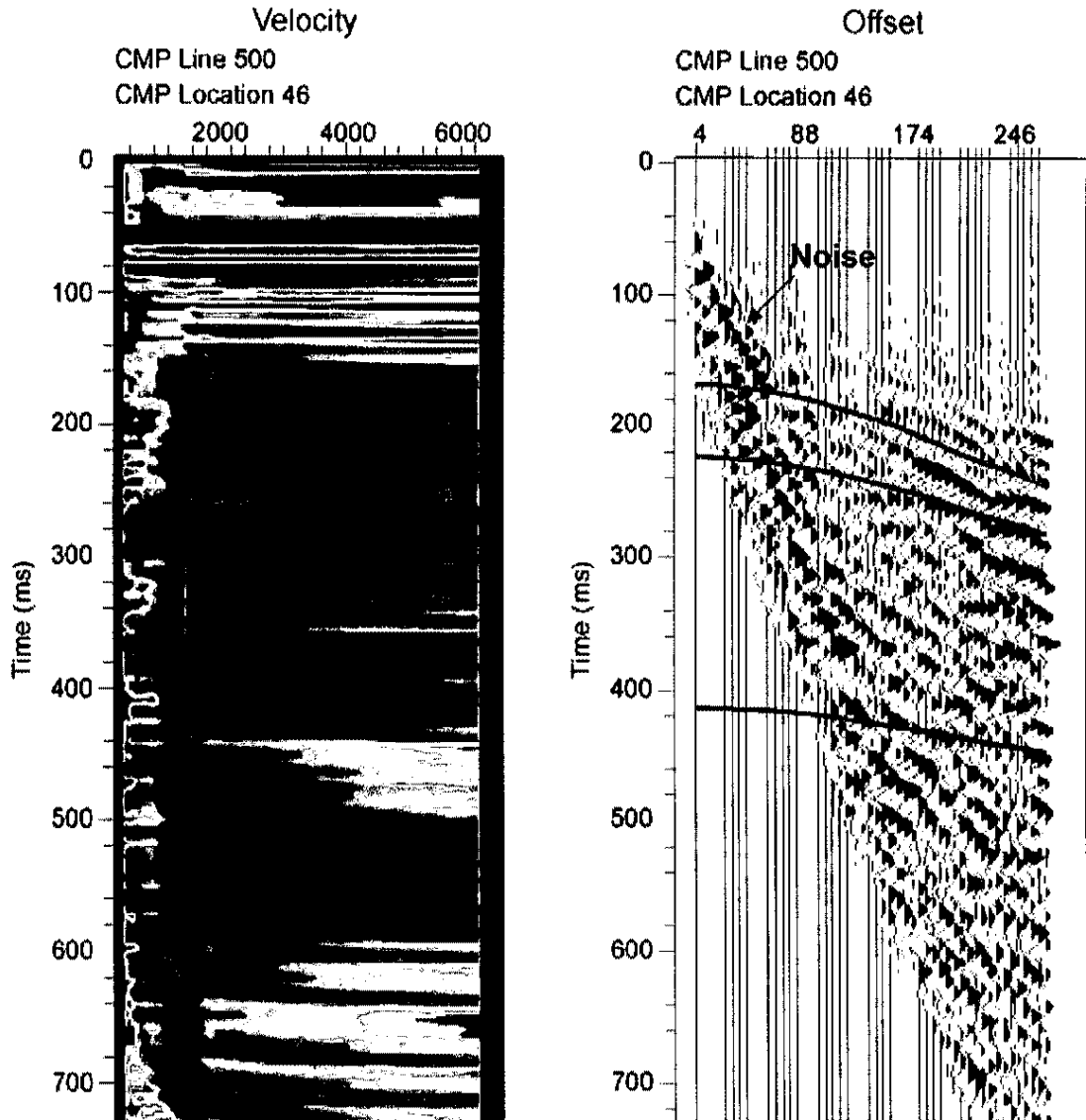
Figure 41. Left: Velocity semblance map of CMP location 46. Pink "bull's-eyes" show areas where semblance is approximately equal to 1. Black line shows picking of RMS velocity estimates based on these bull's-eyes. Velocity estimates for this CMP location are 1450 to 1550 m/s. Right: Wiggle variable area plot of CMP Location 46. Green lines mark the location of reflection hyperbolas that correspond with the bull's-eyes picked on the semblance map. Coherent linear noise (red arrow) in the upper left-hand portion of the plot tends to obscure a portion of these hyperbolas.
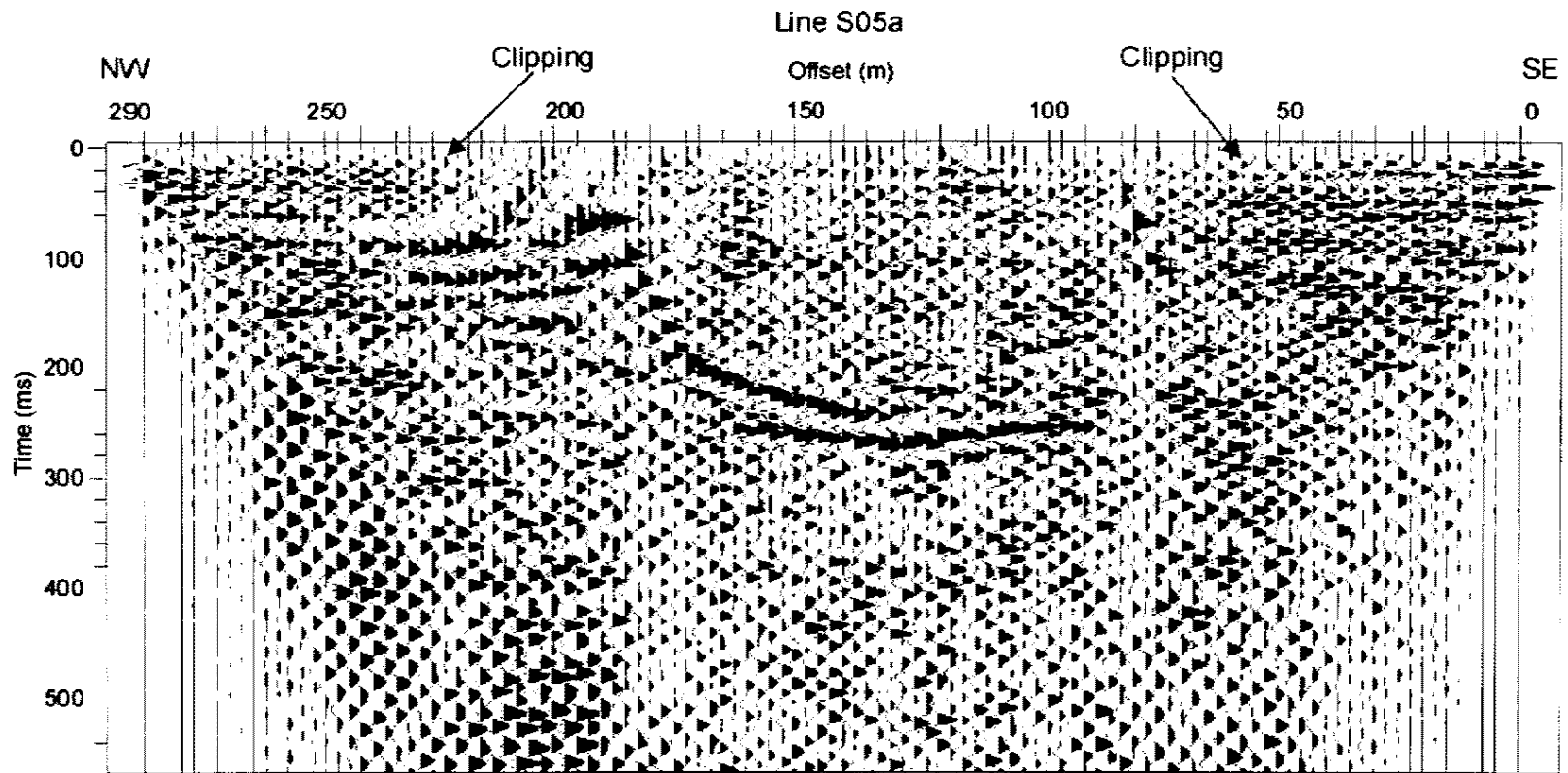
Figure 42. Unmigrated CMP stack of Line S05a. Co-location of shot points and receivers produced clipping of some traces in the near surface (examples are noted by the red arrows).
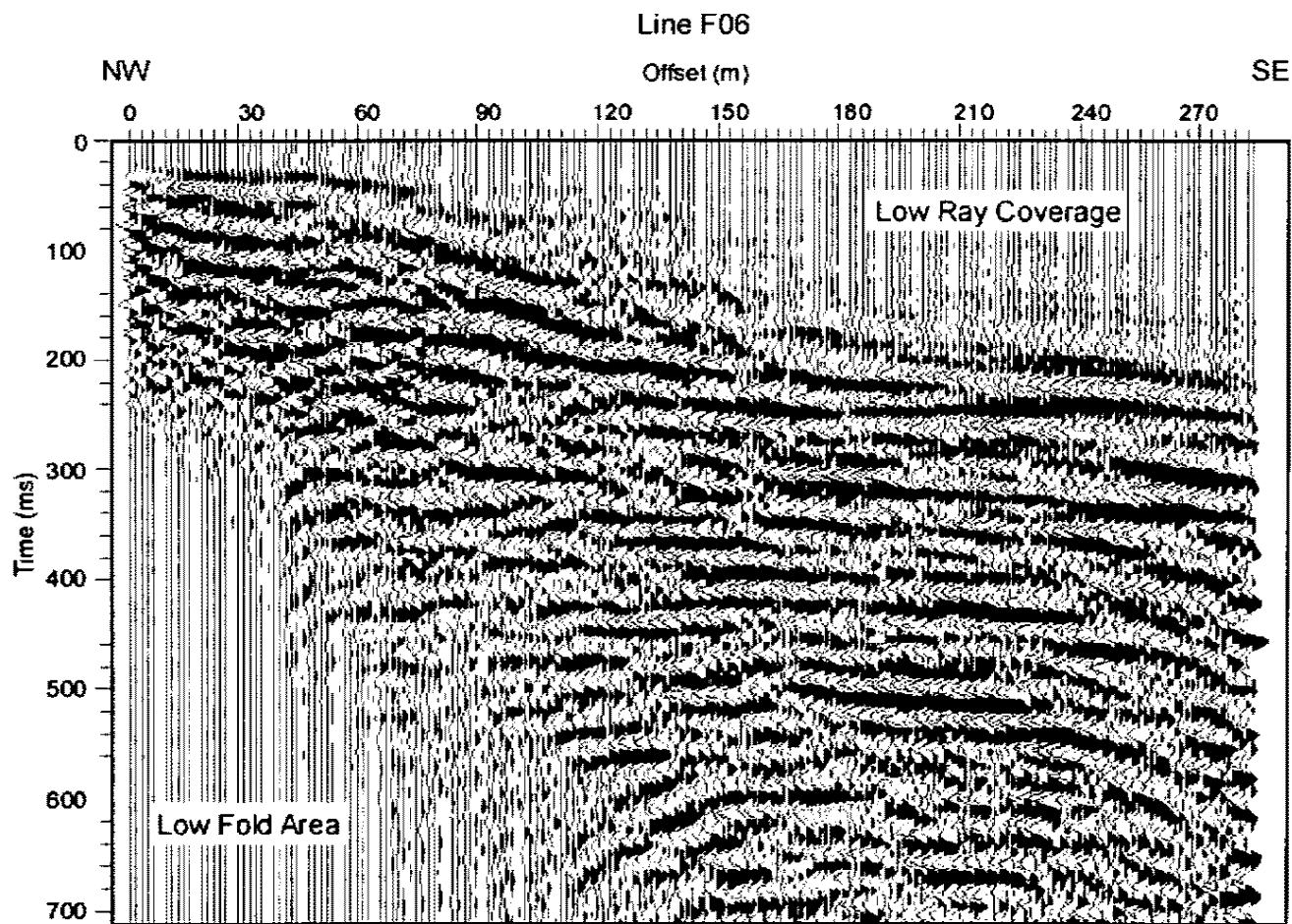
Figure 43. Unmigrated CMP stack of Line F06. Because only 51 shots were acquired, low ray coverage occurs in the near surface at the SE end of the profile. This leads to a lack of sufficient data to determine reflections in this area of the profile. No clipping of traces is noted. Energy drop-off in the lower left-hand portion of the profile is due to low fold (low ray coverage) at the extremity of the seismic line.
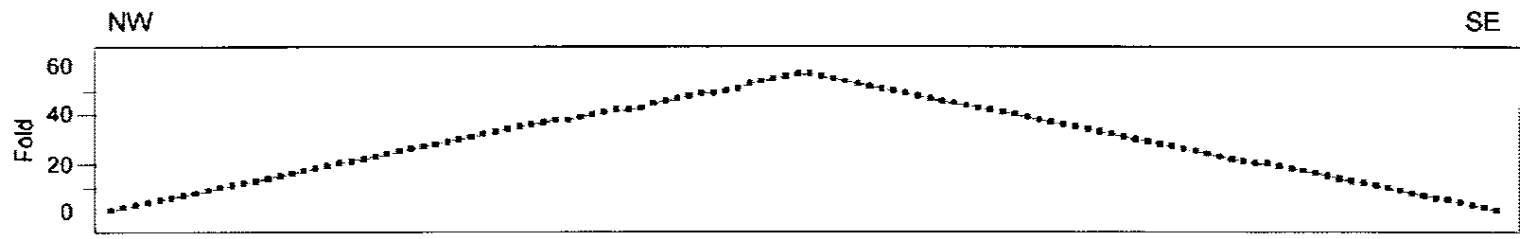
Figure 44a. Fold plot for Line S05a showing maximum fold of 58 at the center of the profile.
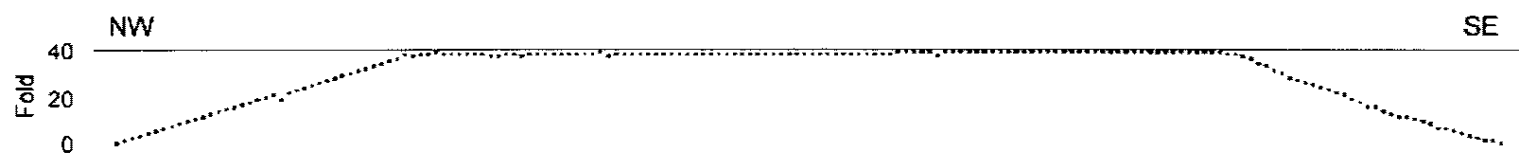
Figure 44b. Fold plot for Line F06, showing maximum fold of ~40, with fold tapering off at the ends of the profile.
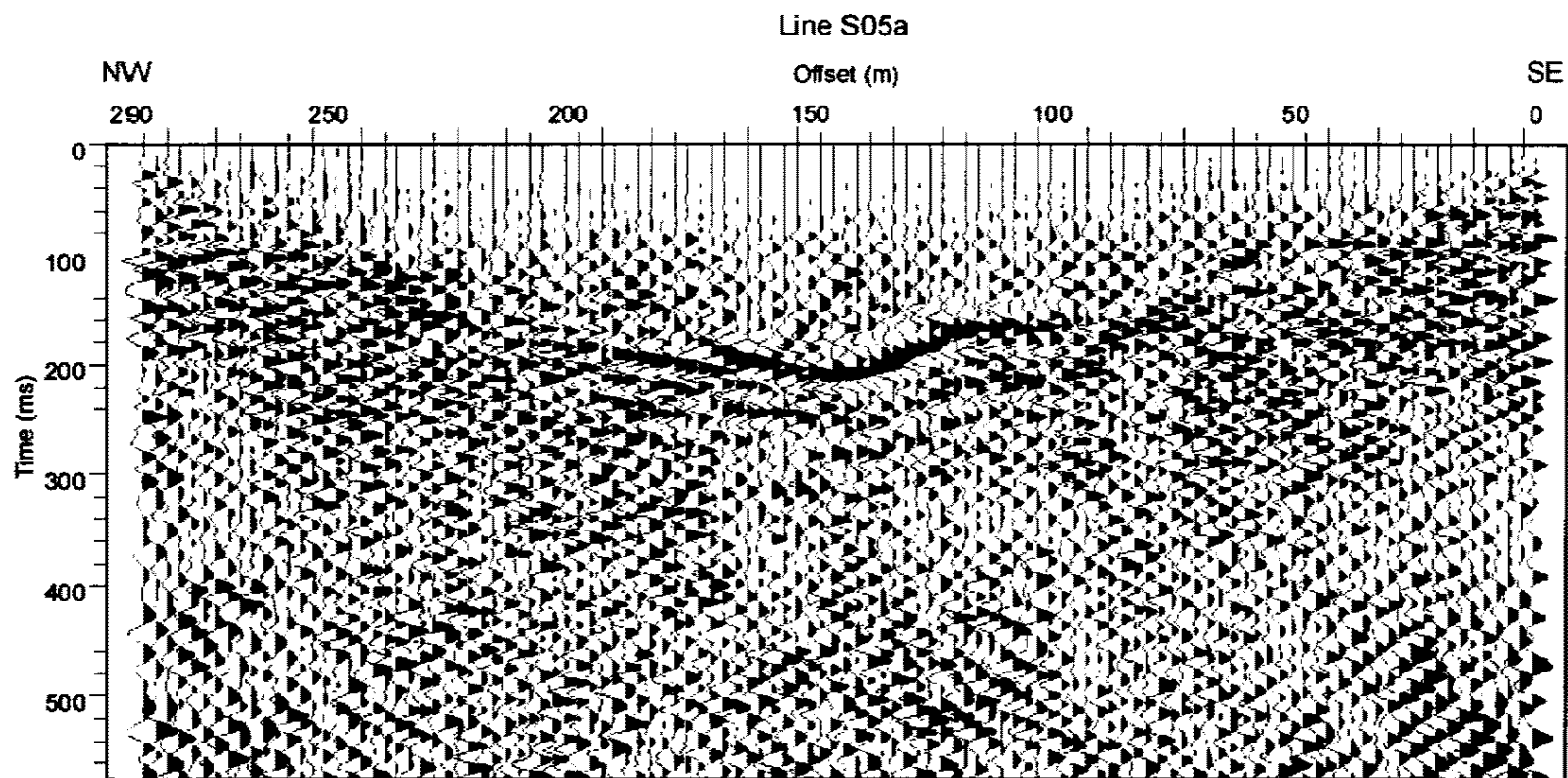
Figure 45. CMP stack of Line S05a post phase shift migration.
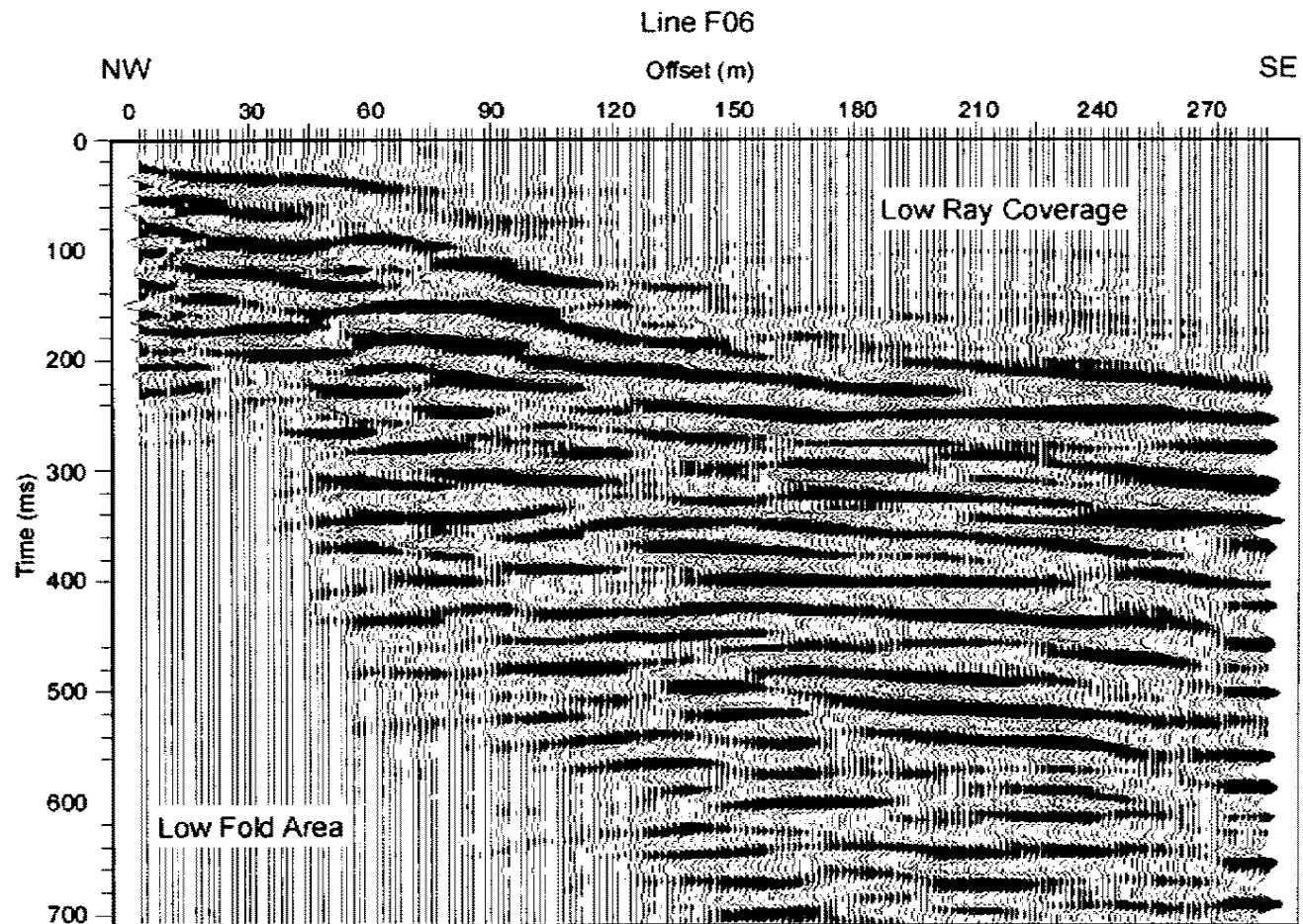
Figure 46. CMP stack of Line F06 after Kirchhoff poststack migration. Because only 51 shots were acquired, low ray coverage occurs in the near surface at the SE end of the profile. This leads to a lack of sufficient data to determine reflections in this area of the profile. No clipping of traces is noted. Energy drop-off in the lower left-hand portion of the profile is due to low fold (low ray coverage) at the extremity of the seismic line.

CHAPTER SEVEN

INTERPRETATIONS

Seismic sections for Lines S05a and F06 were interpreted and then merged

into an interpretive cross-section, analogous to a geologic cross-section, but with

two-way travel time (TWT) on the y-axis (Figures 47 to 50). The S05a section is

290 m in lateral extent (Figure 47). The F06 section extends 282 m laterally

(Figures 48 and 49). The S05a and F06 sections overlap by ~20 m, making

some interpolation possible from one section to another (Figures 47 to 50).

Line S05a

Velocities range from 700 to 1280 m/s at the NW end of the S05a section,

780 to 1000 m/s in the center of the section, and 800 to 980 m/s at the SE end of

the section. These velocities often indicate that the subsurface consists of

unconsolidated to loosely consolidated sediments (e.g., Mussett and Khan,

2000). However, highly fractured igneous units may also exhibit low velocities

(e.g., Ibrahim and Keller, 1981). Based on the surface geology, the S05a section

most likely consists of Quaternary alluvial fan deposits, although some highly

fractured igneous unit(s) corresponding to Taa or Ti may exist at depth (Figures

29 and 50; Plate 1). A diffraction is also noted in the seismic section,

representing energy that was randomly scattered, probably by hitting the edge of

a fault (Figure 47). In addition, a strong reflector at ~150 m offset appears to indicate the presence of a paleochannel (Figure 47). The upper 4 to 5 m of the section were indistinguishable.

The S05a reflection section reveals offset horizons that would indicate the presence of several normal fault strands, with some faults becoming listric at depth (Figures 47 and 50). Faults dip in the SE direction at ~56 to 77 degrees, with the exception of one antithetic fault, which dips in the NW direction at ~74 degrees. (Figures 47 and 50). Offset on S05a faults varies from ~5 to ~15 m, indicating multiple slip events. Differences in thickness of units across some faults may indicate syndepositional faulting (Figures 47 and 50). Vertical resolution of 4 to 5 m precludes visualizing offsets <4 to 5 m. The NW-most fault on the S05a section is on strike with the SE-most strand of the BHF scarp (Fossett, 2005).

Line F06

Since the unmigrated seismic section may have vertical exaggeration when compared to the migrated section, making it easier to visualize offset horizons, interpretations for Line F06 were first performed on the unmigrated section (Figure 48) (e.g., Yilmaz, 2000). Since the S05a reflection section overlaps the F06 reflection section by ~20 m, Horizons 1, 2 and 3 from S05a, as well as the NW-most fault from S05a were interpolated onto the F06 section and labeled Horizons 1y to 3y, respectively, to assist in interpretations where the F06 section had low ray coverage (Figures 47 to 50). Velocities range from 1100 to 1350 m/s

at the NW end of the section, 1050 to 1550 m/s in the center of the section, and 1250 to 1850 m/s at the SE end of the section. These velocities may indicate that the subsurface consists of unconsolidated to loosely consolidated sediments or highly fractured igneous units (e.g., Ibrahim and Keller, 1981; Mussett and Khan, 2000). Based on the surface geology, the F06 section most likely consists of highly fractured Taa and/or Ti at the NW edge of the section, and Quaternary alluvial fan deposits at the SE end of the section, with highly fractured Taa and/or Ti at depth (Figures 29 and 50; Plate 1). The upper 9 to 10 m of the section were indistinguishable.

The unmigrated F06 reflection section reveals offset horizons that would indicate the presence of several normal fault strands (Figure 48). Migration of the F06 section moved reflections to their proper positions in TWT (e.g., Yilmaz, 2000). Therefore, migration caused the faults interpreted on the unmigrated section to shorten in length and to move in their updip direction, as expected (Figure 49) (e.g., Yilmaz, 2000). Dips on F06 faults were estimated from the migrated section at ~80 to 85 degrees, with some faults becoming listric at depth (Figures 48 to 50). Offset on F06 faults varies from ~6 m to >30 m, indicating multiple slip events. The larger offset figures are uncertain, due to low ray coverage in the shallow surface of the section (Figures 48 and 49). Vertical resolution of 4 to 5 m precludes visualizing offsets <4 to 5 m. The fault adjacent to the Taa outcrop is on strike with the longest strand of the BHF scarp (Fossett, 2005).
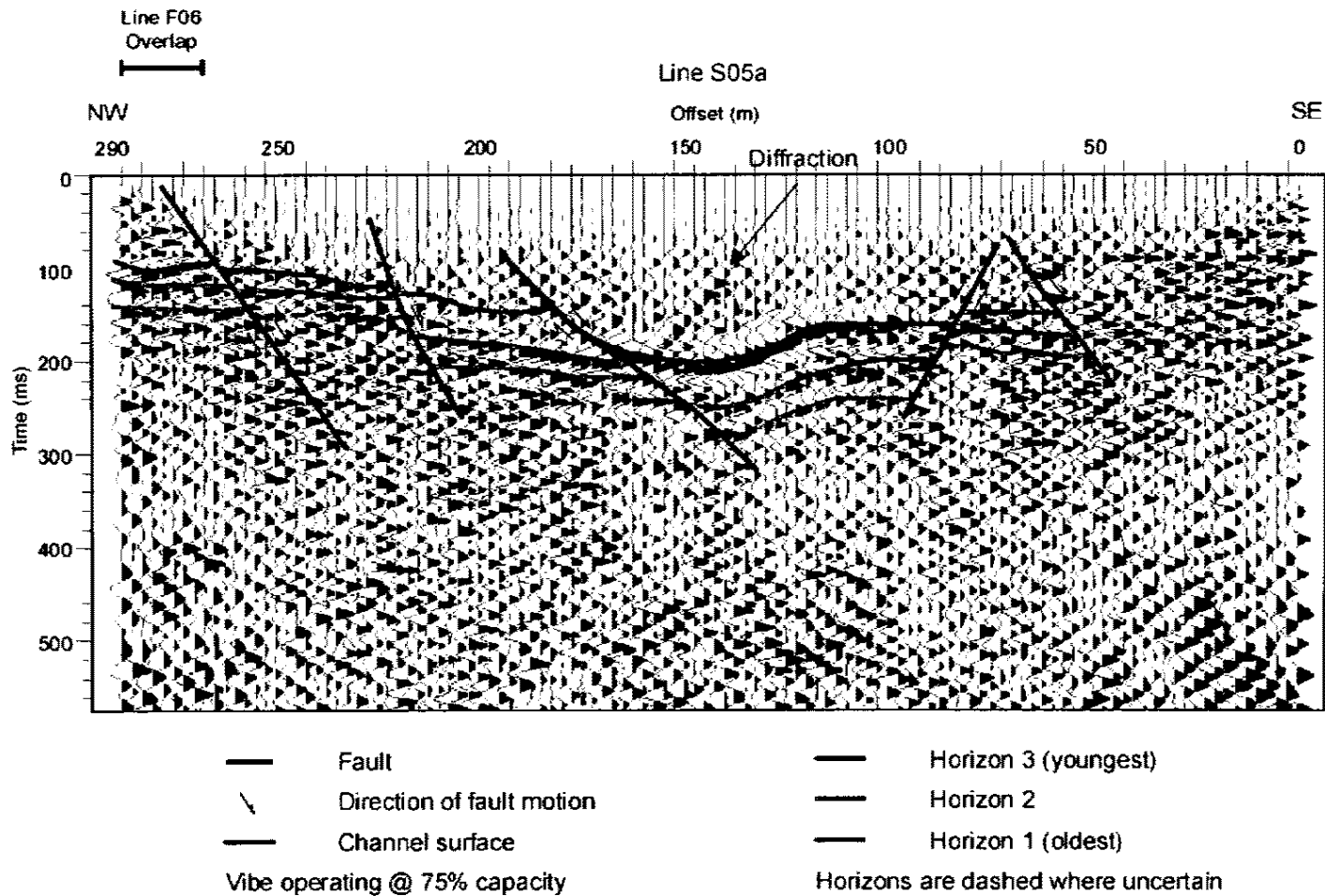
Figure 47. Interpreted seismic section for Line S05a. See text for discussion. Fault dips range from ~56-77 degrees, with offsets ~5-15 m. Fault at the NW end of the section is on strike with the SE-most BHF scarp.
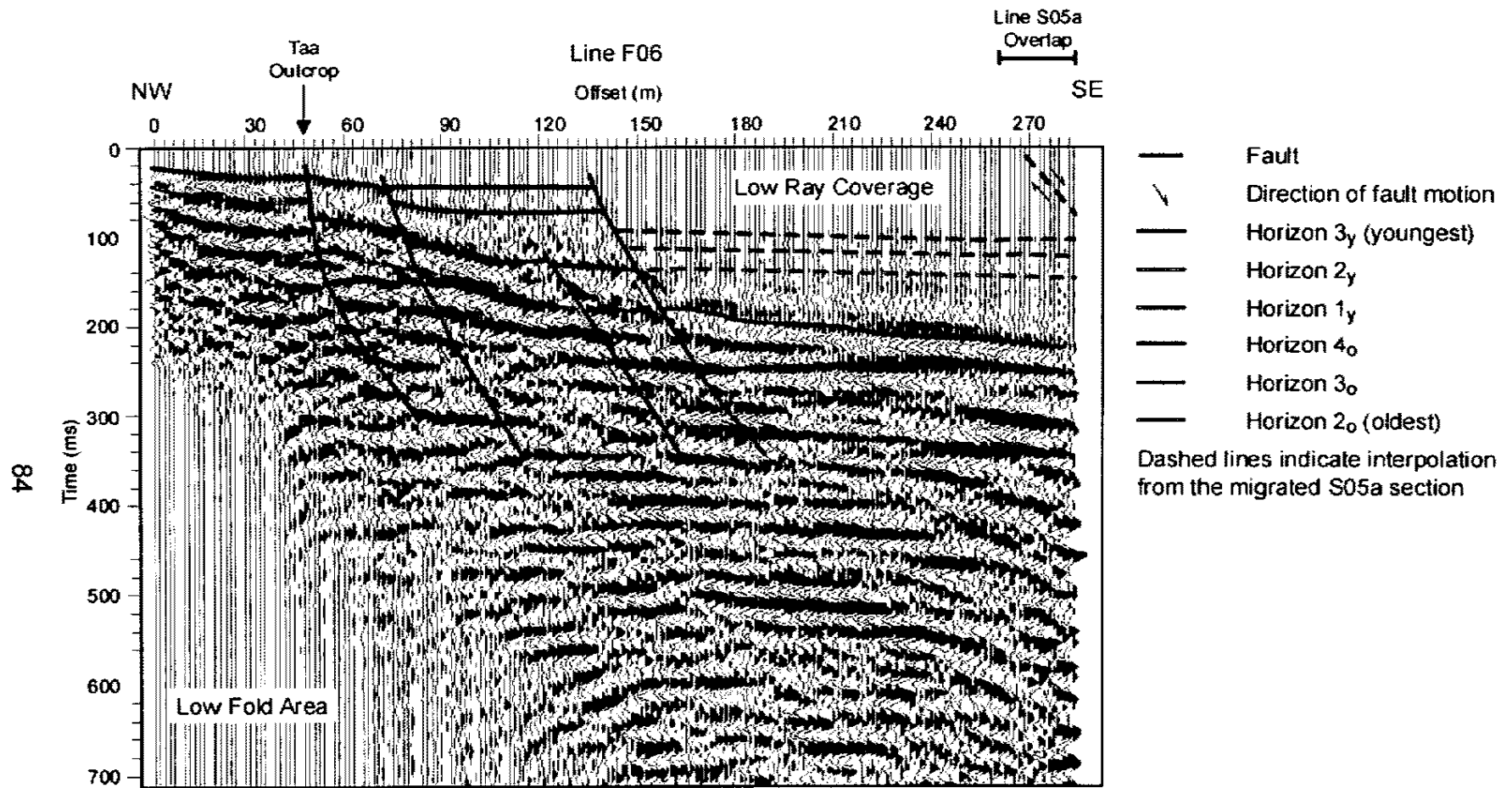
Figure 48. Interpreted unmigrated seismic section for Line F06. See text for discussion. Fault dips range from ~80-85 degrees, with minimum offset ~6 m. Fault adjacent to Taa outcrop is on strike with the longest BHF scarp (Fossett, 2005).
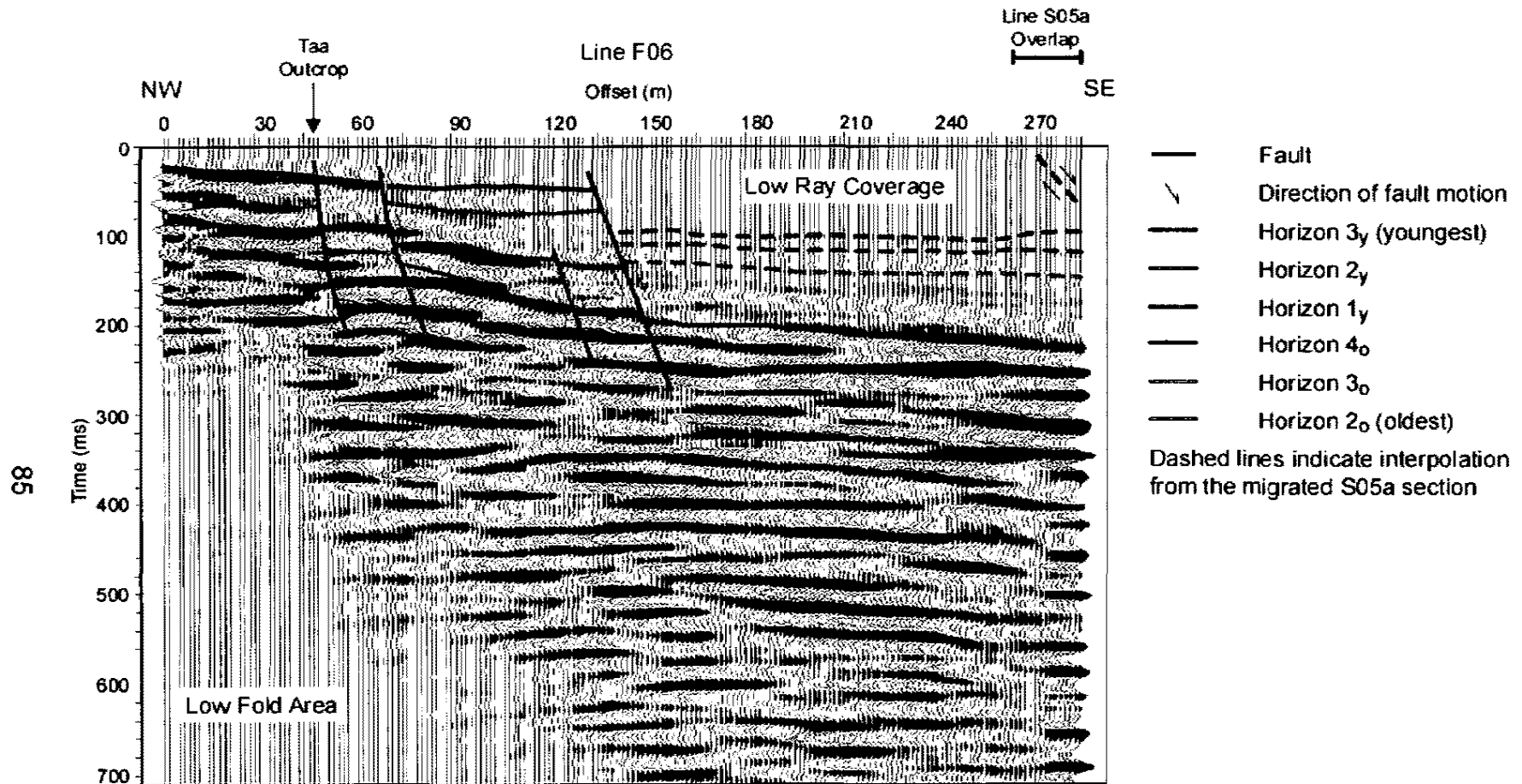
Figure 49. Interpreted migrated seismic section for Line F06. See text for discussion. Fault dips range from ~80-85 degrees, with minimum offset ~6 m. Fault adjacent to Taa outcrop is on strike with the longest BHF scarp (Fossett, 2005).

CHAPTER EIGHT

DISCUSSION/CONCLUSIONS

This study examined the question of whether the BHF trace continues in the subsurface south of the known surface rupture. To answer this question, a three-component approach was utilized. First, remote sensing imagery was analyzed to determine the ideal study location. Second, geologic mapping documented surface geology to assist with interpretation of the seismic profile. Third, high-resolution seismic reflection data were processed and analyzed to determine structural relationships in the subsurface south of the BHF scarp.

The existence of normal faults in the subsurface at the locations of Lines F06 and S05a provide an interesting component in the question of BHF length. Since the fault adjacent to the Taa outcrop is on strike with the longest strand of the BHF scarp, this suggests that the BHF may continue south of the scarp (Fossett, 2005). If these fault strands correspond to the previously mapped BHF strands, then the minimum subsurface extent of the BHF relative to the surface is ~6 km (Fossett, 2005). If, based on the linear trends noted in SRTM hillshaded imagery and Laplacian-filtered Landsat imagery, the BHF actually extends along the entire Black Hills mountain front, the minimum subsurface extent of the BHF would be ~9.5 km (Figure 27). However, no evidence of surface rupture was found south of the seismic line. In addition, Fossett (2005) noted that the SRL

may be rheologically controlled by the location of the Black Hills pluton (T_i),

causing rupture to occur in the softer Quaternary sediments along the base of the

pluton. If BHF rupture has been constrained by the pluton, a minimum

subsurface extent of 6 km would be reasonable, since T_i does crop out as far

south as the seismic line (Figure 29 and Plate 1).

Age constraints on faults mapped in the seismic sections are difficult to

determine, since the upper 4 to 5 m are uninterpretable. Offset of Quaternary

alluvium would restrict the age of fault rupture to <1.8 Ma; however, it cannot be

conclusively stated whether these faults could be Holocene (<10,000 ya). The

question of whether Holocene rupture has occurred along these profiles could be

examined utilizing seismic reflection with a hammer source along these profiles

to look at the upper 4 to 5 m. Otherwise, analyses and age dating of materials in

a paleoseismic trench in this location, although logistically difficult due to cost

and/or permitting issues, would be most conclusive.

Structural Models

Previous workers have established that the regional extension direction in the

vicinity of the BHF is E-W. However, rather than exhibiting a ~N-S strike, as

would be expected of a dip-slip fault in this region, the BHF strikes NE-SW.

Although other faults in the McCullough Range have segments with variable

orientations, these faults are Miocene in age and were not likely active during the

Quaternary. Furthermore, any Quaternary slippage on these faults due to E-W

extension would be governed by Byerlee's Law, which states that for pre-existing

faults, motion is resisted by sliding friction rather than internal friction of the surrounding rock (Byerlee, 1978). Thus, failure on pre-existing faults may not be oriented at the expected angle relative to the maximum principal stress direction (Byerlee, 1978). Rupture along the BHF did not occur along a pre-existing fault. Therefore, Byerlee's Law does not explain the unexpected orientation of the BHF relative to the principal stress direction.

Three models are proposed as possible explanations of this unpredicted orientation for the BHF. These models also address the question of why the fans adjacent to the Black Hills tend to be deeply dissected, while the fans of the Eldorado Mountains are relatively gently sloping and nondissected.

1. *Rotational Model*. This model assumes that the Black Hills were at one time oriented ~N-S. Following rupture on the BHF, the Black Hills and the BHF experienced clockwise rotation (Figure 51). However, neither remote sensing data nor geologic mapping data reveal any cause for rotation of the Black Hills area. This lack of a reasonable cause makes this model an unlikely explanation for the NE-SW strike of the BHF.

2. *Localization Model*. Greater rheological strength in the Ti could cause localization of BHF rupture in weaker sedimentary lithologies along the flanks of the Black Hills pluton (Figure 52). However, if the dominant extension is E-W, some oblique motion on the BHF would be expected. Fossett (2005) established via aerial photography that very little, if any, oblique motion exists on the BHF.

3. *Strain Partitioning Model.* Sinistral motion on the EVF coupled with an E-W extension direction could provide the necessary components of motion to cause NW-SE dip-slip rupture on the BHF (Figure 53). However, there is no documentation in the literature for sinistral motion on the EVF. In addition, various authors do not agree on the actual location of the EVF (e.g., Langenheim and Schmidt, 1996; Faulds et al., 2001; Fossett, 2005). This emphasizes the need for more studies to be performed on the EVF to better constrain its location and kinematics. In the regional context, strike-slip faults in the western portion of the North American Plate have motions consistent with the orientation of these faults. For example, a NW-striking fault will tend to have dextral motion, while NE- or E-striking faults tend to have sinistral motion (Figure 54) (e.g., Wernicke, 1992). Movement on these strike-slip faults has a strong influence on extension in the region (e.g., Wernicke, 1992). Therefore, the regional control for the Strain Partitioning Model acknowledges that stresses associated with the interaction between the Pacific Plate and the North American Plate are distributed across a wide region from the plate boundary toward the interior of the North American Plate. Thus, motion on relatively smaller faults such as the BHF may ultimately be influenced by motion on larger fault zones, such as the Garlock fault (GF) or the Death Valley Fault Zone (DVFZ) (Figure 54).

Although further research needs to be performed on the BHF and the EVF, this study supports the possibility that the BHF trace extends in the subsurface

south of the previously mapped BHF scarp (Fossett, 2005). However, this study does not prove conclusively whether the segment of the BHF identified in the seismic sections is linked to one or more strands along the scarp. Additional seismic studies between the scarp and the S05/F06 profile locations may be able to address this question.

Alternatively, the BHF segment along the scarp and the segment identified on the S05/F06 seismic profiles may have ruptured independently in the past. However, due to their close proximity, non-linkage of these segments does not necessarily preclude the segments from rupturing simultaneously. In either case, the two segments may be considered part of a larger BHF system.

The minimum subsurface length for the BHF system is estimated at 6 km, measured from the northernmost surface expression of the BHF to the location of the seismic profiles. In the event where the two BHF segments rupture simultaneously, this would imply a greater seismic hazard for the BHF than the predicted potential of M_w 5.7 based on SRL alone (Fossett, 2005). Casualty and property damage estimates based on simultaneous rupture of the adjacent fault segments could be performed via HAZUS-MH Loss Estimation studies, similar to those performed on the Frenchman Mountain fault (Hess and dePolo, 2006). Such estimates would assist the communities of Boulder City, Henderson, and Las Vegas to determine appropriate mitigation of the seismic hazard posed by the BHF.
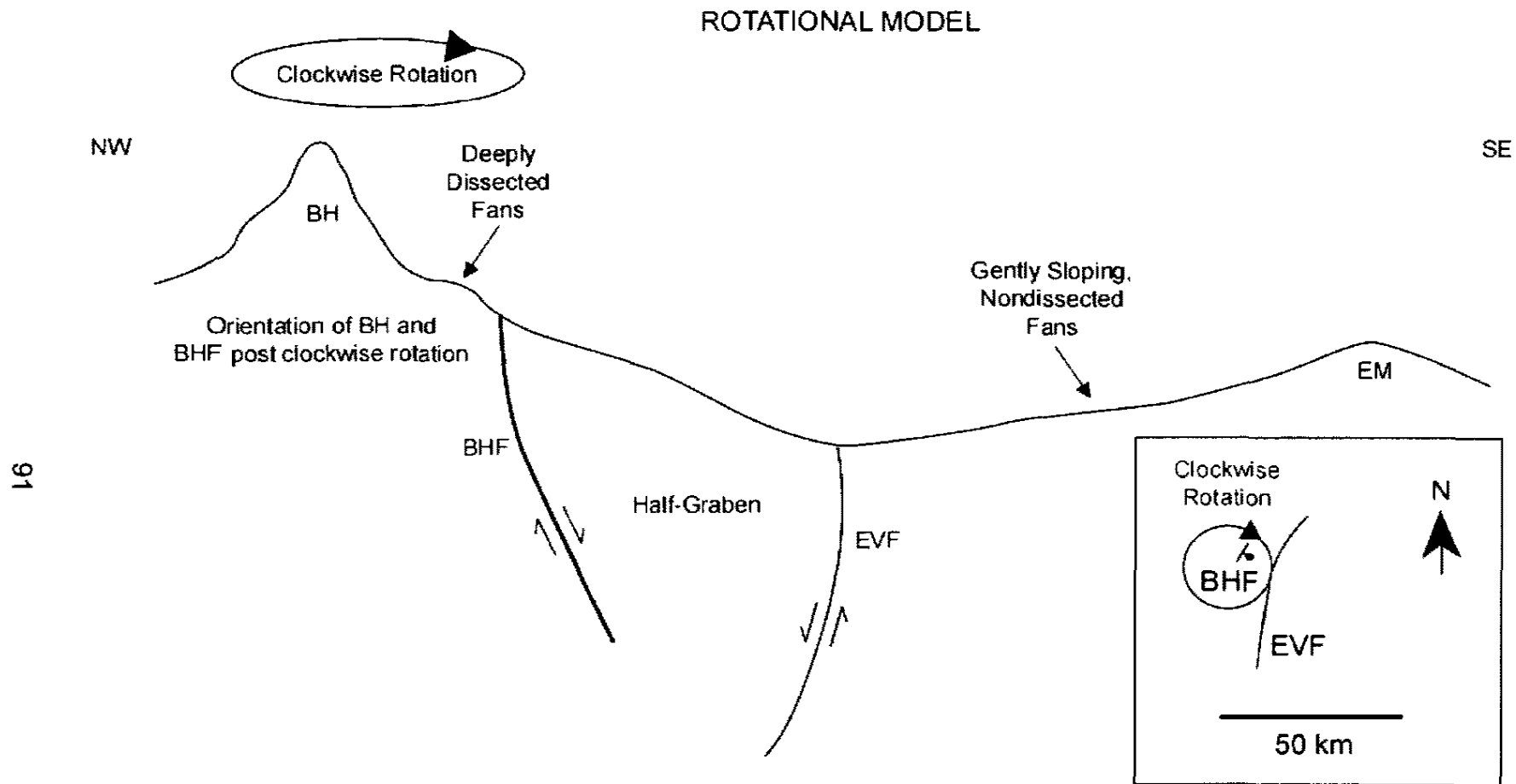
ROTATIONAL MODEL

Figure 51. Rotational Model for the BHF. This model assumes that the BHF was originally oriented N-S, and that dip-slip motion on the BHF was subsequently followed by clockwise rotation of the Black Hills (BH) and the BHF. This model also assumes that the EVF is not active, which would explain the gently sloping, nondissected fans of the Eldorado Mountains (EM). Inset shows map view.

LOCALIZATION MODEL

NW   SE

Deeply
Dissected
Fans

BH

Rigid Pluton
Localizes
Rupture Orientation

Gently Sloping,
Nondissected
Fans

EM

BHF

Half-Graben

EVF

Rigid
Pluton

N

BHF

EVF

50 km
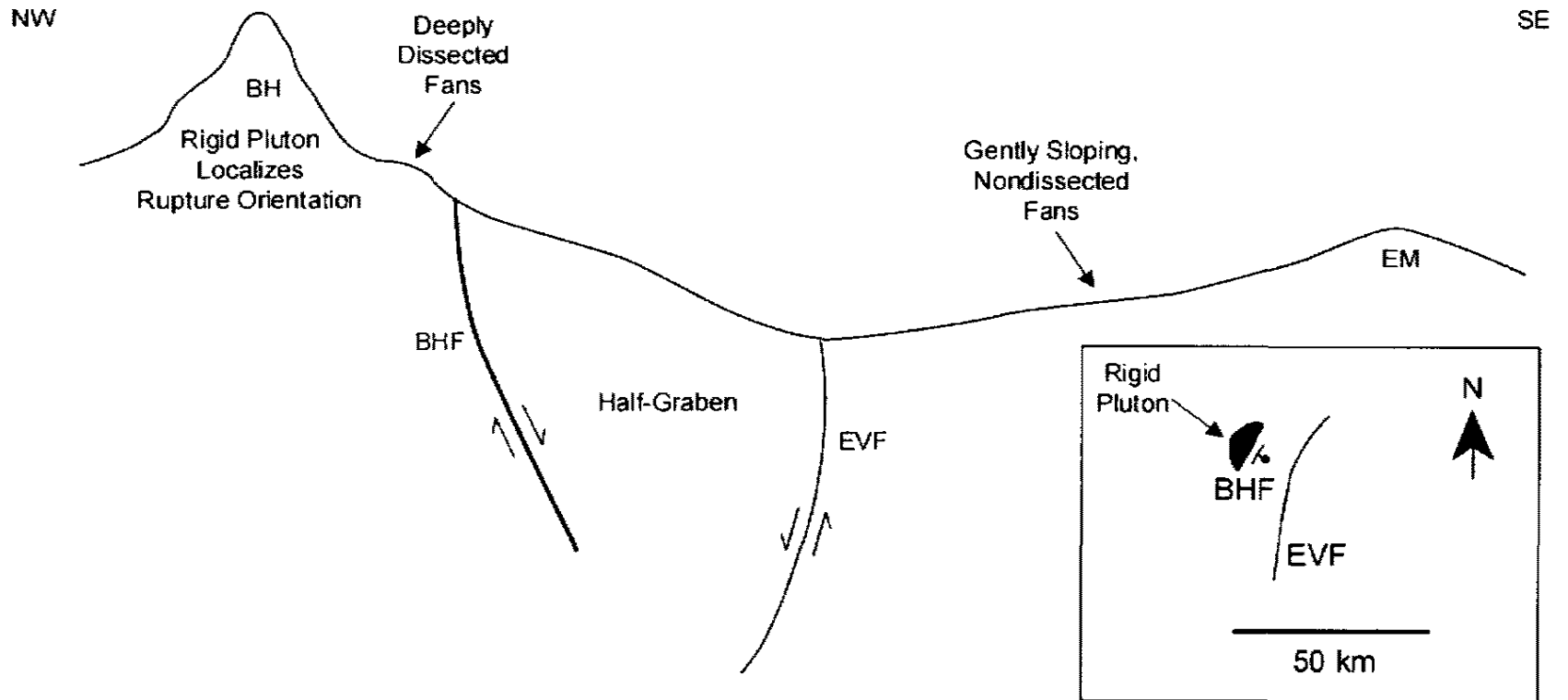
Figure 52. Localization Model for the BHF. This model assumes that the relatively rigid Black Hills pluton (mapped as Ti in Figure 29) localizes rupture on the BHF to its NE-SW orientation. This model also assumes that the EVF is not active, which would explain the gently sloping, nondissected fans of the Eldorado Mountains (EM) in contrast with the deeply dissected fans of the Black Hills (BH). Inset shows map view.

92

STRAIN PARTITIONING MODEL
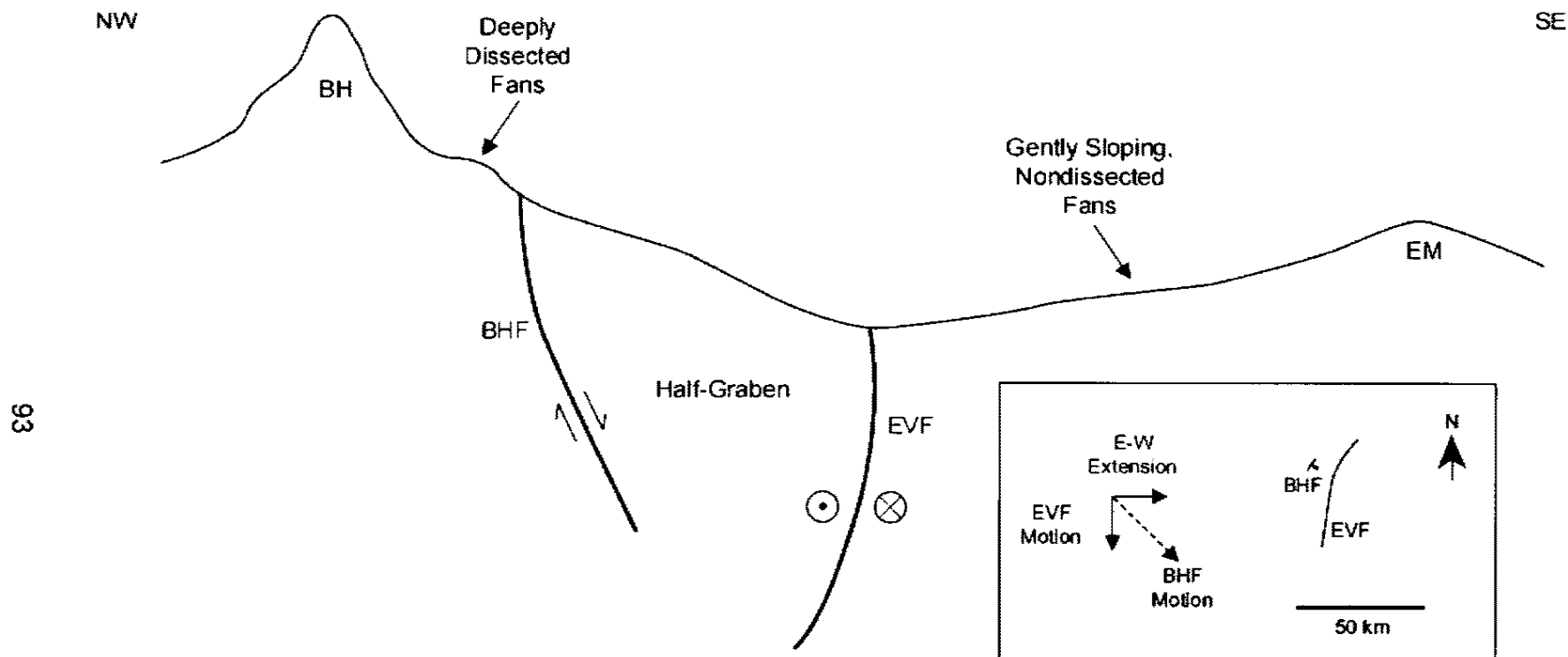
Figure 53. Strain Partitioning Model for the BHF. This model assumes that the EVF exhibits sinistral motion, which, coupled with an E-W extension direction, causes NW-SE dip-slip motion on the BHF. Sinistral motion on the EVF may explain the gently sloping, nondissected fans of the Eldorado Mountains (EM) in contrast with the deeply dissected fans of the Black Hills (BH). Inset shows vectors representing motion components for the BHF: The E-W extension motion component is shown in red; EVF motion component is shown in blue; combined motion on the BHF is shown in black.
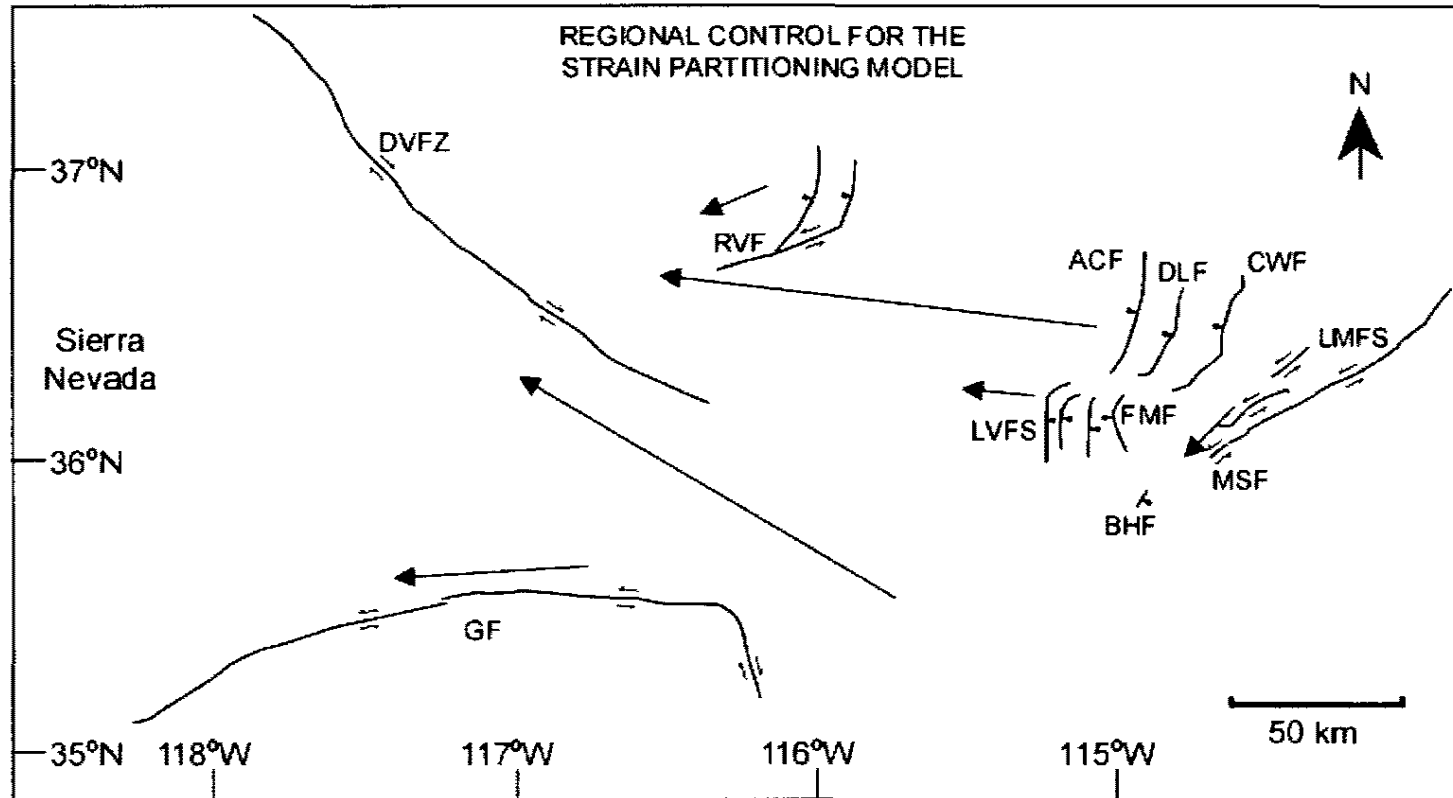
Figure 54. Regional Control for the Strain Partitioning Model. A simplified regional fault map is shown, based on Coe et al (2004) and Fossett (2005), with black lines representing faults. Normal faults show a ball on the downthrown side. Strike-slip faults show black arrows to indicate direction of motion. The red arrows show generalized extension directions, with longer arrows indicating higher rates of extension. ACF-Arrow Canyon fault, BHF-Black Hills fault, CWF-California Wash fault, DLF-Dry Lake fault. DVFZ-Death Valley fault zone, EVF-Eldorado Valley fault, FMF-Frenchman Mountain fault, GF-Garlock fault, LMFS-Lake Mead fault system, LVFS-Las Vegas Valley fault system, MSF-Mead Slope fault, RVF-Rock Valley fault.

REFERENCES

Anderson, L.W., 1973, Large-magnitude Late Tertiary strike-slip faulting, north of Lake Mead, Nevada: United States Geological Survey Professional Paper, Report P 0794, 18 p.

Anderson, L.W., and O'Connell, D.R., 1993, Seismotectonic study of the northern portion of the Lower Colorado River, Arizona, California, and Nevada: U.S. Bureau of Reclamation, Seismotectonic Report 93-4, Denver, Colorado, 122 p.

Anderson, R.E., 1977, Geologic map of the Boulder City 15-minute quadrangle, Clark County, Nevada: United States Geological Survey, Map GQ-1395, scale 1:62,500, 1 sheet.

Atwater, T., 1970, Implications of plate tectonics for the Cenozoic tectonic evolution of western North America: Geologic Society of America Bulletin, v. 81, p. 3513-3535.

Bell, J.W., 1981, Subsidence in Las Vegas Valley: Bulletin, Nevada Bureau of Mines and Geology, no. 95, 84 p.

Bohannon, R.G., 1979, Strike-slips faults of the Lake Mead region of Nevada, in Armentrout, J.J., Cole, M.R., and Terbest, H., eds., Cenozoic paleogeography of the western United States: Society of Economic Paleontologists and Mineralogists, Pacific Section, Pacific Coast Paleogeography Symposium 3, p. 129-139.

Bohannon, R.G., 1984, Nonmarine sedimentary rocks of Tertiary age in the Lake Mead region, southeastern Nevada and Northwestern Arizona: U.S. Geological Survey Professional Paper 1259, 72 p.

Boland, K.A., 1996, The petrogenesis of andesites produced during regional extension: Examples from the northern McCullough Range, NV and Xitle volcano, Mexico, [MS Thesis]: University of Nevada, Las Vegas, 127 p.

Burchfiel, B.C., Cowan, D.S., and Davis, G.A., 1992, Tectonic overview of the Cordilleran orogen in the western United States, in Burchfiel, B.D., Lipman, P.W., and Zoback, M.L., eds., The Cordilleran Orogen: Conterminous U.S.:

Boulder, Colorado, Geological Society of America, The Geology of North America, v. G-3, p. 407-479.

Byerlee, J.D., 1978, Friction of rocks: Pure and Applied Geophysics, v. 116, p. 615-626.

Campagna, D. J. and Aydin, A., 1994, Basin genesis associated with strike-slip faulting in the Basin and Range, southeastern Nevada: Tectonics, v. 13, p. 327-341.

Christiansen, R.L., Yeats, R.S., Graham, S.A., Niem, W.A., Niem, A.R., and Snavely, P.D., Jr., 1992, Post-Laramide geology of the U.S. Cordilleran region, in Burchfiel, B.D., Lipman, P.W., and Zoback, M.L., eds., The Cordilleran Orogen: Conterminous U.S.: Boulder, Colorado, Geological Society of America, The Geology of North America, v. G-3, p. 261-406.

Coe, J.A., Yount, J.C., O'Leary, D.W., Taylor, E.M., 2004, Paleoseismic investigations on the Rock Valley fault system: United States Geological Survey Professional Paper, Report P 1689, p. 175-196.

Cox, M., 1999, Static corrections for seismic reflection surveys, Tulsa, Oklahoma: Society of Exploration Geophysicists, 531 p.

DeCelles, P.G., 2004, Late Jurassic to Eocene evolution of the Cordilleran thrust belt, and foreland basin system, western U.S.A.: American Journal of Science, v. 304, p. 105-168.

dePolo, C.M., Bell, J.W., Boron, S., Slemmons, D.B., and Werle, J.L., 2006, Latest Quaternary fault movement along the Las Vegas Valley Fault System, Clark County, Nevada: Environmental & Engineering Geoscience, v. 12, p. 181-193.

Duebendorfer, E.M., and Black, R.A., 1992, Kinematic role of transverse structures in continental extension: An example from the Las Vegas Valley shear zone, Nevada: Geology, v. 20, p. 1107-1110.

Evans, B.J., 1997, A handbook for seismic data acquisition in exploration, Tulsa, Oklahoma: Society of Exploration Geophysicists, 305 p.

Faulds, J.E., Feuerbach, D.L., Miller, C.F., and Smith, E.I., 2001, Cenozoic evolution of the northern Colorado River extensional corridor, southern Nevada and northwest Arizona: Pacific Section of the American Association of Petroleum Geologists Publication GB 78 (also Utah Geological Association Publication 30), p. 239-272.

Fossett, E., 2005, Paleoseismology of the Black Hills Fault, southern Nevada, and implications for regional tectonics, [MS Thesis]: University of Nevada, Las Vegas, 103 p.

Fossett, E., Taylor, W. J., Snelson, C. M., Tecle, M. G., and Luke, B. A., 2003, New Insights into the Quaternary Black Hills Fault, Southern Nevada, Geological Society of America Abstracts with Programs, v. 35, p. 65.

Fossett, E., Taylor, W.J., Snelson, C.M., Tecle, M.G., and Luke, B.A., 2003, Paleoseismicity and regional seismic hazard implications of Quaternary faulting along the Black Hills fault, southern Nevada: Association of Engineering Geologists Program with Abstracts, v. 46, p. 55-56.

Global Land Cover Facility (GLCF), 2005, Earth science data interface, http://glcf.umiacs.umd.edu/data/, accessed Mar 27, 2005.

Hess, R.H., and dePolo, C.M., 2006, Loss-estimation modeling of earthquake scenarios for each county in Nevada using HAZUS-MH: Nevada Bureau of Mines and Geology Open-File Report 06-1, 517 p.

Humphreys, E.D., 1995, Post-Laramide removal of the Farallon slab, western United States: Geology, v. 23, p. 987-990.

Ibrahim, A.W., and Keller, G.V., 1981, Seismic velocities and electrical resistivity of recent volcanics and their dependence on porosity, temperature, and water saturation: Geophysics, v. 46, p. 1415-1422.

Illinois State Geological Survey, 2004, http://www.isgs.uiuc.edu/app-geophy/tools/ appgeophys_seisreflect.htm, accessed Jan 16, 2006.

Jensen, J.R., 2000, Remote sensing of the environment: An earth resource perspective, Upper Saddle River, New Jersey: Prentice-Hall, Inc., 544 p.

Keck, W.M., 1994, Digital orthophoto quadrangle, Boulder City NW: Earth sciences & mining research information center, http://keck.library.unr.edu/, accessed February 2, 2007.

Langenheim, V.E., Grow, J.A., Jachens, R.C., Dixon, G.L., and Miller, J.J., 2001, Geophysical constraints on the location and geometry of the Las Vegas Valley shear zone, Nevada: Tectonics, v. 20, p. 189-209.

Langenheim, V.E., and Schmidt, 1996, Thickness and storage capacity of basin fill of the northern part of the Eldorado Valley, Nevada, and the extent of the Boulder City pluton, United States Geological Survey Open-File Report 96-512, 27 p.

Lines, L.R., and Newrick, R.T., 2004, Fundamentals of geophysical interpretation, Tulsa, Oklahoma: Society of Exploration Geophysicists, 268 p.

MacQueen, J.B., 1967, Some methods for classification and analysis of multivariate observations: Proceedings of the 5-th Berkeley Symposium on Mathematical Statistics and Probability: Berkeley: University of California Press, v. 1, p. 281-297.

Marsden, D., 1993, Static corrections—a review, The Leading Edge, v. 12, p. 43-49, 115-119, 210-216.

Mussett, A.E. and Khan, M.A., 2000, Looking into the earth, New York: Cambridge University Press, 470 p.

Officer, C.B., 1974, Introduction to theoretical geophysics, New York: Springer-Verlag, 551 p.

Ostenaa, D., 1984, Relationships affecting estimates of surface fault displacement based on scarp-derived colluvium deposits: Geological Society of America Abstracts with Programs, v. 16, p. 327.

Palmer, A.R. and Geissman, J., 1999, Geological time scale: Geological Society of America, http://www.geosociety.org/science/timescale/timescl.pdf, accessed April 2, 2007.

Research Systems, Inc. (RSI), 2005, ENVI tutorials: ENVI v. 4.1, CD-ROM.

Sabins, F.F., 1997, Remote sensing: Principles and interpretation, New York: W.H. Freeman and Company, 494 p.

Short, N.M., 1984, Ratio, PCA, and maximum likelihood analysis of the Utah site: NASA, http://rst.gsfc.nasa.gov/Sect5/Sect5_3.html#5-6, accessed March 24, 2007.

Slemmons, D.B., Bell, J.W., dePolo, C.M., Ramelli, A.R., Rasmussen, G.S., Langenheim, V.E., Jachens, R.C., Smith, K., and O'Donnell, J., 2001, Earthquake hazard in Las Vegas, Nevada, in Luke, B., Jacobson, E., and Werle, J. (eds.), Proceedings, 36th annual symposium on engineering geology and geotechnical engineering, University of Nevada Las Vegas, p. 447-459.

Smith, K., O'Donnell, J., and Slemmons, B., 2001, Seismicity and ground motion hazards in the Las Vegas area, Nevada, in Luke, B., Jacobson, E., and Werle, J. (eds.), Proceedings, 36th annual symposium on engineering geology and geotechnical engineering, University of Nevada Las Vegas, p. 447-459.

Stewart, J.H., and Carlson, J.E., 1977, Geologic map of Nevada: Nevada Bureau of Mines and Geology, http://www.nbmg.unr.edu/dox/e30.pdf, accessed March 28, 2007.

Tabor, L.L., 1982, Geology of the Las Vegas area: Department of Energy Report JAB-10145-1.

Taylor, W. J., 1998, Mesozoic and Cenozoic tectonics and structures of southern Nevada, in dePolo, C. M., ed., Proceedings of a Conference on Seismic Hazards in the Las Vegas Region: Las Vegas, Nevada, Nevada Bureau of Mines and Geology Open-File Report 98-6, p. 12-23.

Taylor, W. J., Fossett, E., Luke, B., Snelson, C., Rasmussen, T., McCallen, D., Rodgers, A., and Louie, J., 2003, Quaternary Faults and Basin-fill sediments of the Las Vegas Basin, Southern Nevada, EOS Trans. AGU, 84(46), Fall Meet. Suppl., Abstract S12E-06.

Telford, W.M., Geldart, L.P., and Sheriff, R.E., 1990, Applied geophysics, New York: Press Syndicate of the University of Cambridge, 770 p.

United States Geological Survey (USGS), 2002, Shuttle Radar Topography Mission, 1 Arc Second scene SRTM_u03_n035w115, Unfilled Unfinished 2.0, http://seamless.usgs.gov/, accessed April 20, 2005.

United States Geological Survey (USGS), 2007, Advanced National Seismic System (ANSS), http://earthquake.usgs.gov/research/monitoring/anss/index.php, accessed April 26, 2007.

Weber, M.E., and Smith, E.I., 1987, Structural and geochemical constraints on the reassembly of disrupted mid-Miocene volcanoes in the Lake Mead-Eldorado Valley area of southern Nevada: Geology, v. 15, p. 553-556.

Werle, J.L., and Knight, L.H., 1992, Estimation of maximum surface displacement of the Eldorado Valley fault, Clark County, Nevada, for pipeline design: in Sharma, Sunil, ed., Proceedings of the 285h Symposium on Engineering Geology and Geotechnical Engineering, p. 27-42.

Werle, J.L., and Knight, L.H., 1998, Natural gas pipeline fault crossing— investigation of the potential rupture hazard from the Black Hills Fault, Clark County, Nevada, in dePolo, C.M., ed., Seismic hazards in the Las Vegas region, Nevada Bureau of Mines and Geology Open-File Report 98-6, p. 196.

Wernicke, B., 1992, Cenozoic extensional tectonics of the U.S. Cordillera, in Burchfiel, B.D., Lipman, P.W., and Zoback, M.L., eds., The Cordilleran

Orogen: Conterminous U.S.: Boulder, Colorado, Geological Society of
America, The Geology of North America, v. G-3, p. 553-581.

Yilmaz, Ö., 2001, Seismic data analysis processing, inversion, and interpretation
of seismic data, Tulsa, Oklahoma: Society of Exploration Geophysicists, v. 1,
1000 p.

Young, R.A., 2004, A lab manual of seismic reflection processing, The
Netherlands: EAGE Publications bv, 126 p.

VITA

Graduate College
University of Nevada, Las Vegas

Shelley A. Zaragoza

Local Address:
4378 Shortleaf St
Las Vegas, NV 89119

Home Address:
11303 Ash Creek Dr
Houston, TX 77043

Degrees:
Bachelor of Science, Geology, 2004
University of Nevada, Las Vegas

Selected Academic Awards and Honors:
Bernada E. French Fund Graduate Scholarship, 2005-2006
Society of Exploration Geophysicists Scholarship, 2005-2006
Nevada Space Grant Consortium Graduate Scholarship, 2005
National Dean's List 2003, 2005
Shell Oil International Award, 2003-2004
Nevada Space Grant Consortium Undergraduate Scholarship, 2000-2004
Norman R. Tilford Field Studies Scholarship, 2004
Edwin Wiegand Science and Technology Scholarship, 2001-2004
Bernada E. French Fund Undergraduate Scholarship, 2002-2004
UNLV College of Science Dean's List, 2000-2003
Mary Dougherty Honors Scholarship-EC 2002-2003
Who's Who Among Students in American Universities and Colleges, 2003
Phi Kappa Phi National Honor Society, 2003

Publications:
Zaragoza, S.A., Snelson, C.M., Saldaña, S.C., Hirsch, A., Poche, S., and
    Taylor, W.J., 2006, Imaging the Black Hills fault, Clark County, Nevada
    utilizing high-resolution seismic reflection and vibroseis, Eos Trans. AGU,
    v. 87 (52), Fall Meet. Suppl., Abstract NS41A-1117.

Zaragoza, S.A., Snelson, C.M., Jernsletten, J.A., Saldaña, S.C., Hirsch, A. and McEwan D., 2005, High-Resolution Seismic Reflection Profiling Across the Black Hills Fault, Clark County, Nevada: Preliminary Results, Eos Trans. AGU, v. 86 (52), Fall Meet. Suppl., Abstract S22A-04.

Zaragoza, S.A., and Snelson, C.M., 2004, Crustal Velocity Model of Watusi Data Integrated with Legacy Data, Clark County, Nevada, Eos Trans. AGU 85(47), Fall Meet. Suppl., Abstract S34A-06.

Zaragoza, S.A., Snelson, C.M., McEwan, D., Sandru, J, and Hirsch, A., 2003, Crustal velocity model of Watusi and Legacy seismic refraction data, Clark County, Nevada, Eos Trans. AGU, 84(46), Fall Meet. Suppl., Abstract S11D-0321.

Zaragoza, S.A., Snelson, C.M., McEwan, D., Hirsch, A., Sandru, J., and Draa, A., 2003, Las Vegas Valley Seismic Response Project (LVVSRP): Initial results from seismic refraction experiments, GSA Abstracts with Programs, v. 34, no. 7, p. 477.

Thesis Title:
Imaging the Southern Trace of the Black Hills Fault, Clark County, Nevada

Thesis Examination Committee:
Chair, Dr. Catherine M. Snelson, Ph.D.
Committee Member, Dr. Wanda J. Taylor, Ph.D.
Committee Member, Dr. Eugene I. Smith, Ph.D.
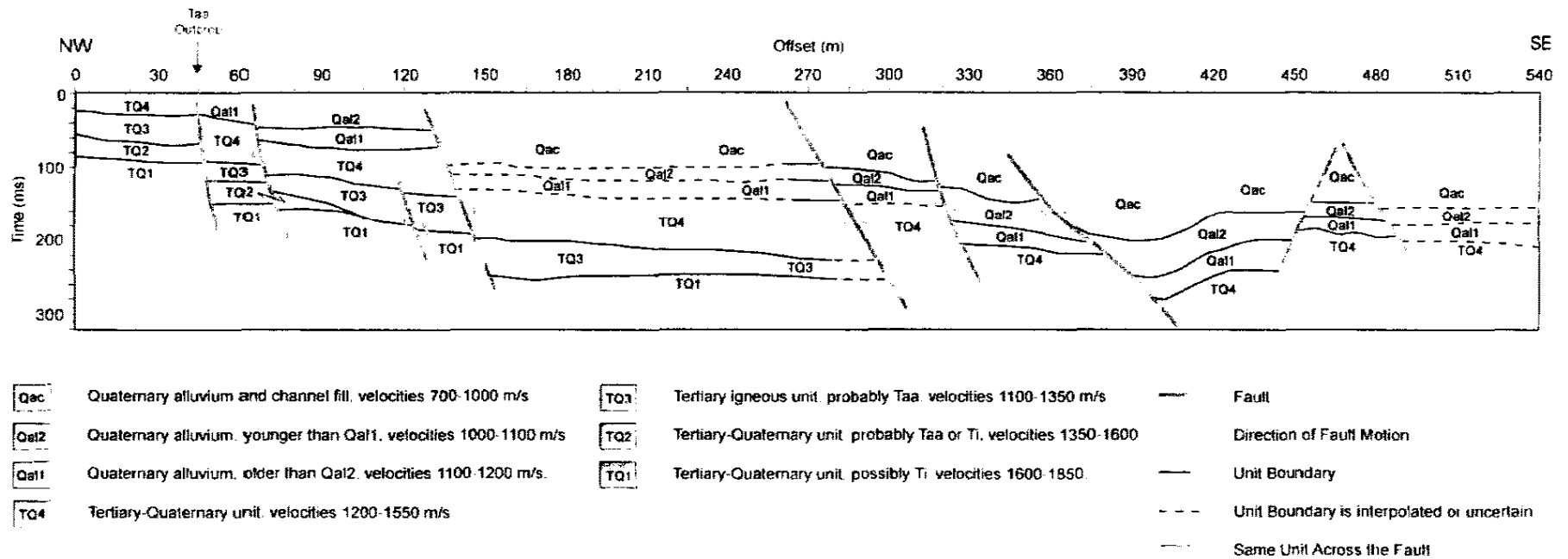Graduate College Faculty Representative, Dr. Michael G. Pravica, Ph.D.

Figure 38. Simplified processing flow chart based on Cox (1999), Yilmaz (2001), and Young (2004).

NW ... Offset (m) ... **SE**

Taa Outcrop

0   30   60   90   120   150   180   210   240   270   300   330   360   390   420   450   480   510   540

Time (ms): 0 — 100 — 200 — 300

TQ4, TQ3, TQ2, TQ1, Qal1, Qal2, Qac, TQ3, TQ4, TQ2, TQ1, TQ3, TQ1, Qal1, Qal2, Qal1, Qal2, Qal1, Qac

| Qac | Quaternary alluvium and channel fill, velocities 700-1000 m/s | TQ3 | Tertiary igneous unit, probably Taa, velocities 1100-1350 m/s | —— | Fault |

| Qal2 | Quaternary alluvium, younger than Qal1, velocities 1000-1100 m/s | TQ2 | Tertiary-Quaternary unit, probably Taa or Ti, velocities 1350-1600 | | Direction of Fault Motion |

| Qal1 | Quaternary alluvium, older than Qal2, velocities 1100-1200 m/s | TQ1 | Tertiary-Quaternary unit, possibly Ti, velocities 1600-1850 | —— | Unit Boundary |

| TQ4 | Tertiary-Quaternary unit, velocities 1200-1550 m/s | | | - - - | Unit Boundary is interpolated or uncertain |

| | | | | —— · | Same Unit Across the Fault |

Figure 50. Interpretive cross-section of Lines F06 and S05a, with offset from the NW-most receiver on the x-axis and TWT on the y-axis. See text for discussion. Location of Taa outcrop is marked with a blue arrow. Fault dips range from ~56 to 85 degrees, with minimum offset ~5 m. Fault adjacent to Taa outcrop is on strike with the longest BHF scarp (Fossett, 2005).